Physically Programmable Surfaces

A dissertation presented
by

Alexander David Wissner-Gross

to
The Department of Physics
in partial fulfillment of the requirements
for the degree of
Doctor of Philosophy
in the subject of

Physics

Harvard University
Cambridge, Massachusetts
October 2007

Thesis advisor

Efthimios Kaxiras

Author

Alexander David Wissner-Gross

Physically Programmable Surfaces

Abstract

The progress of civilization has depended on the development of materials whose properties can be increasingly finely customized. Such customization reached an apotheosis with the availability of materials that could support readily-programmed universal computation. With the software revolution arguably complete, it is natural to look to the physical world of atoms not yet sequestered for computation for the next great leaps in material control. To bring the benefits of software to matter, novel properties and forms of programmability must be developed. The natural place to begin with adding functionality to materials is at their surfaces, where they are likeliest to interact with the world. In this thesis, I demonstrate novel functionality relating to six physical characteristics of surfaces: chemical, electrical, thermal, hydrodynamic, mechanical, and magnetic properties. For chemical programmability, I show how gaps between electrodes with precisely controllable widths can be synthesized, enabling chemical specificity. For electrical programmability, I show that nanowire interconnects can be assembled, reconfigured, and disassembled on a surface. For thermal programmability, I show that by varying the surface chemistry of diamond films, different thicknesses of ice films can be stabilized at elevated temperatures. For hydrodynamic programmability, I show that hollow semiconductor

nanostructures of various geometries can be synthesized, allowing sub-attoliter liquid transport on surfaces. For mechanical programmability, I show how a large particle can be stochastically manipulated through tossing by a vibrated bed of smaller particles. For magnetic programmability, I show that ensembles of local Ising-like interactions on 1-D and 2-D lattices lead to rich pattern formation that can partially be predicted.

Contents

List of Figures

List of Tables

Citations to Previously Published Work

Chapter 2 appeared as

> "Arrays of Cu(2+)-complexed organic clusters grown on gold nano dots", A. Hatzor-de Picciotto, A. D. Wissner-Gross, G. Lavallee, and P. S. Weiss, J. Exp. Nanosci. **2**, 3-11 (2007).

Chapter 3 appeared as

> "Dielectrophoretic reconfiguration of nanowire interconnects", A. D. Wissner-Gross, Nanotechnology **17**, 4986-4990 (2006).
>
> "Dielectrophoretic architectures", A. D. Wissner-Gross, Nano-Scale and Bio-Inspired Integrated Computing (Ed. M.M. Eshaghian-Wilner, Wiley, 2007).

Chapter 4 appeared as

> "Diamond stabilization of ice multilayers at human body temperature", A. D. Wissner-Gross, E. Kaxiras, Phys. Rev. E Rapid Comm. **76**, 020501 (2007).

Chapter 5 appears as

> "Single-crystal silicon nanotubes, hollow nanocones, and branched nanotube networks", B. P. Timko and A. D. Wissner-Gross (equal contrib.), W. Lu, A. B. Greytak, C. M. Lieber, submitted to Nano Lett.

Chapter 6 appears as

> "Surface intruder dynamics on vibrated granular beds", A. D. Wissner-Gross, submitted to Granular Matt.

Chapter 7 appears as

> "Pattern formation without favored local interactions", A. D. Wissner-Gross, J. Cellular Automata **2** (In press, 2007).

Acknowledgments

Thanks to my family, Elizabeth Wissner-Gross, Sigmund Wissner-Gross, Zachary Wissner-Gross, Timothy Sullivan, Aileen Wissner, Irwin Wissner, Cynthia Gross, and Robert Gross;

my elementary school science teachers, Rose Grabelsky, Eileen Magilligan, Andrea Kay, Ruth Bertman, Martha Ripp, and Lew Love;

my middle and high school science teachers and advisors, Mark Epstein, Richard Soviero, Timothy Hickey, Arnold Ross, James Ellenbogen, Joyce O'Connor, Robert Silverstone, Albert Cavallaro, Col. Charles Duggan, Peter Suchman, Melanie Krieger, Vicki Merten, Mike Golden, and Steven Conrad;

my college teachers and advisors, Hartley Rogers, Gerald Sussman, Boleslaw Wyslouch, Anne Hunter, Nancy Savioli, Munther Dahleh, Jinane Abounadi, Ravi Shah, and Joost Bonsen;

my college research supervisors, Push Singh, Marvin Minsky, Hank Smith, Neil Gershenfeld, Tony Tyson, Greg Kochanski, Paul Weiss, David Goldhaber-Gordon, Shuguang Zhang, Joe Jacobson, and Alexander van Oudenaarden;

my graduate research supervisors, Efthimios Kaxiras, Dudley Herschbach, Andrew Kiruluta, Peter Galison, Lubos Motl, Charles Lieber, and Charles Marcus.

my fellow strivers, Trevor Bass, Brian Laulicht, Eric Stern, David Jeng, Jeremy Hwang, Matthew Tomey, Nirav Shah, Joseph Turian, Derek Dreyer, Zachary London, Benjamin Mathews, Adrian Sox, Matthew Craighead, Natalia Toro, Kirsten Wickelgren, David Moore, Erika Ebbel, Keith Winstein, Lisa Schwartz, Adam Cohen, David Goldhaber-Gordon, Davesh Maulik, Reid Barton, Ethan Cotterill, Raymond Casella, Lisa Carlivati, Jared Weinstein, Patrik Sundberg, Philip Schuster, Megha

Padi, Philip Larochelle, Jonathon Gillen, Rodrigo Guerra, Fernando Patolsky, Ali Javey, Brian Timko, Bozhi Tian, Marya Fyta, Jacob Krich, Edward Boyden, Jeffrey Gore, Larry Page, Nathan Myhrvold, Stephen Wolfram, Leroy Hood, Greg Tseng, and Johann Schleier-Smith.

Dedicated to my family.

Chapter 1

Introduction

The progress of civilization has depended on the development of materials whose properties can be increasingly finely customized. Such customization reached an apotheosis with the availability of materials that could support readily-programmed universal computation. With the software revolution arguably complete, it is natural to look to the physical world of atoms not yet sequestered for computation for the next great leaps in material control [1-6]. To bring the benefits of software to matter, novel properties and forms of programmability must be developed.

Here, I use the terms 'programmable' and 'programmability' in the broader sense of using one physical signal, whether time-shifted or not, to predictably (some would say "rationally") alter another physical signal. In Figures 1.1 and 1.2, I attempt to provide systematic examples of methods for, and applications of, tuning of individual physical properties using different input signal types. For example, piezoelectric materials can use electrical signals as an input signal and transduce them into mechanical signals. Note that the diagonal cells, in which a given physical property is

used to manipulate itself (the classical example being the electrical-electrical signal transduction of the transistor field effect), represent substrates for computation.

The natural place to begin with adding functionality to materials is at their surfaces, where they are likeliest to interact with the world. In this thesis, I demonstrate novel functionality relating to six physical characteristics of surfaces: chemical, electrical, thermal, hydrodynamic, mechanical, and magnetic properties. For chemical programmability, I show how gaps between electrodes with programmable widths can be synthesized, enabling chemical specificity on a surface. For electrical programmability, I show that nanowire interconnects can be assembled, reconfigured, and disassembled on a surface. For thermal programmability, I show that by varying the surface chemistry of diamond films, different thicknesses of ice films can be stabilized at elevated temperatures. For hydrodynamic programmability, I show that hollow semiconductor nanostructures of various geometries can be synthesized, allowing sub-attoliter liquid transport on surfaces. For mechanical programmability, I show how a large particle can be stochastically manipulated through tossing by a vibrated bed of smaller particles. For magnetic programmability, I show that ensembles of local Ising-like interactions on 1-D and 2-D lattices lead to rich pattern formation that can be partially predicted and controlled.

Such special-purpose programmable surfaces could have a significant impact in fields ranging from medicine to energy to education, which I identify in each chapter. In the long term, I expect that research on physically programmable surfaces will ultimately lead to the development of "universal programmable surfaces" that unify control of a panoply of physical characteristics, as shown schematically in Figure 1.3.

A universal programmable surface would represent the culmination of millenia of materials physics research, whether deliberate or not, and would finally unify bits and atoms.

OUTPUT SIGNAL/PROPERTY TYPE	INPUT SIGNAL/PROPERTY TYPE: Mechanical	Thermal/ Vibrational	Electrical	Magnetic
Mechanical	➢ Microfluidic LSI	➢ Granular fluidics ➢ Ultrasonic micromanipulation	➢ Piezoelectrics	➢ Magnetostrictive actuators
Thermal/ Vibrational	➢ Mass-sensitive cantilever resonators	➢ Heat switches	➢ Peltier junctions	➢ Inductively heated magnetic particles
Electrical	➢ Piezoelectrics	➢ Thin-film thermocouples	➢ Field effect transistors	➢ GMR-based spin valves
Magnetic	➢ Magnetostrictive sensors		➢ Micro-electromagnets	➢ NMR quantum computation
Electro-magnetic	➢ External-cavity and VCSE lasers	➢ Distributed-feedback lasers ➢ Shockwave-tunable photonic crystals	➢ Electrically tunable laser diodes ➢ Software radio	
Chemical	➢ Single-molecule STM chemistry	➢ Switchable protein-adsorbing polymer film ➢ Sonochemistry	➢ Nanostructured surfaces with electrically reversible hydrophilicity	
Genetic/ Polymeric		➢ RNA thermosensor from Listeria		
Neural/ Ionic	➢ Mechanosensitive ion channels		➢ Neuron chips	

Figure 1.1: Taxonomy of programmable matter technologies by input/output signal type (Part 1).

OUTPUT SIGNAL/PROPERTY TYPE	INPUT SIGNAL/PROPERTY TYPE: Electromagnetic	Chemical	Genetic/ Polymeric	Neural/ Ionic
Mechanical	➢ Optical tweezers	➢ Metal ion-controlled linear and rotary molecular motors	➢ DNA tweezers ➢ B-Z DNA switch ➢ Hybridization-sensitive cantilever	
Thermal/ Vibrational	➢ Laser heating	➢ Exothermic reactions		
Electrical		➢ Nanowire molecular sensors	➢ Nanopore DNA sequencing ➢ Plastic electronics	➢ Neuron chips
Magnetic			➢ Ferritin derivatives	
Electro-magnetic	➢ Photonic transistors	➢ FRET pairs	➢ GFP derivatives ➢ Magnetic polymers	➢ Quantum dots on neurons
Chemical	➢ Laser femtochemistry	➢ Enzyme-based reaction-diffusion computation	➢ Artificial ribozymes and proteins ➢ Modular polyketide synthases	
Genetic/ Polymeric		➢ DNA synthesizers	➢ DNA computing ➢ Genetic circuits	
Neural/ Ionic	➢ Qdot-activated neurons	➢ Neurotransmitters		➢ Thought

Figure 1.2: Taxonomy of programmable matter technologies by input/output signal type (Part 2).

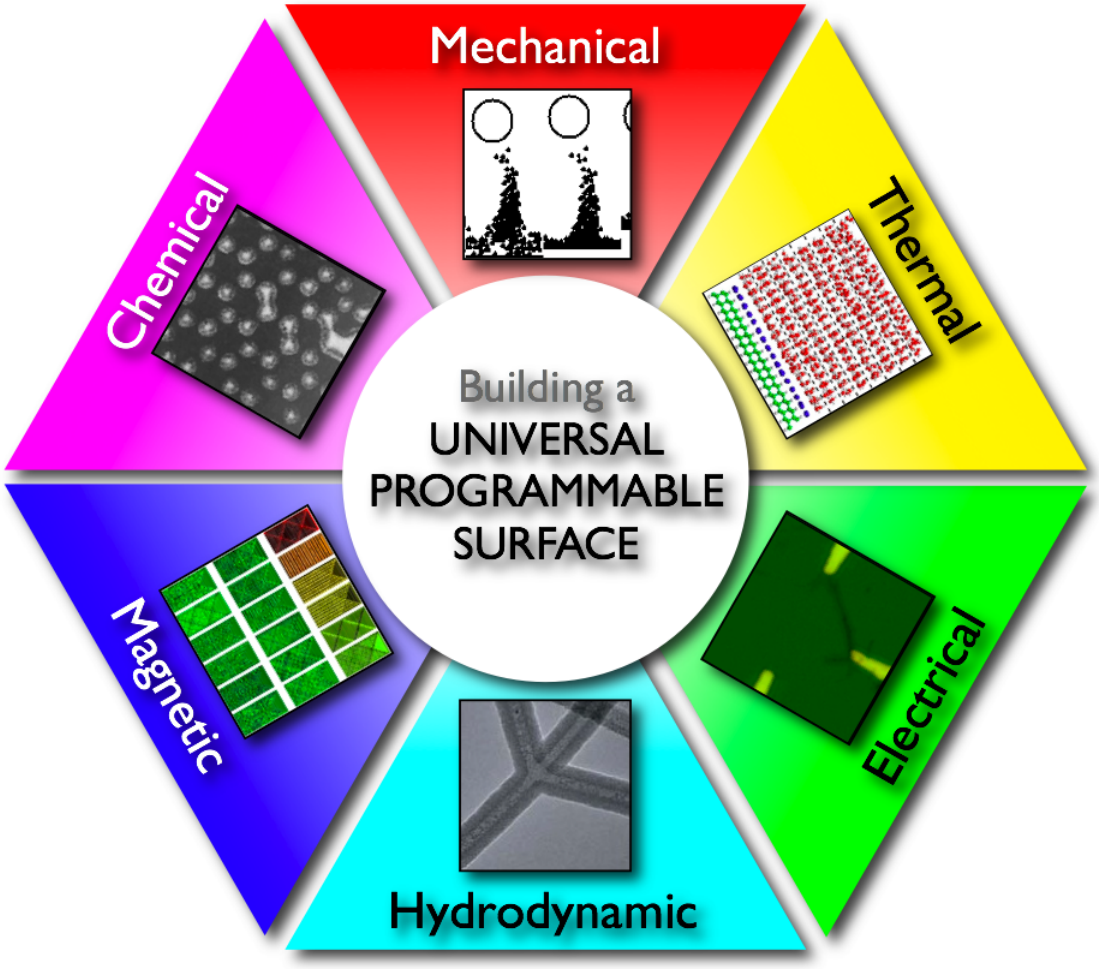

Figure 1.3: Special-purpose physically programmable surfaces and their unification.

Chapter 2

Chemical Programmability

2.1 Introduction

The fabrication of periodic arrays of submicron structures on surfaces has potential applications in electronic and optical devices. In addition, such arrays can be used specifically for optical filtering [7], magnetic storage [8], biological probes [9] and molecular electronics [10, 11]. Much effort has been directed toward finding methods for creating these structures. One particularly economical method is nanosphere lithography (NSL) [12-19], which uses a monolayer or a bilayer of spheres as a porous deposition mask for a large set of materials. NSL has been used to produce several different classes of metal particle patterns with the smallest reproducible gap [15] of 165 nm between particles.

The recent development of the molecular ruler nanofabrication process, which uses an elongated organic molecule as a unit length to define spaces on surfaces [20-24], enables the fabrication of nanostructure arrays with precise control over shape and

dimensions at the nanometer scale. The molecular ruler method enables the creation of very closely spaced metal structures with precise spacings of less than 10 nm. The combination of the NSL method and the molecular ruler technique is promising in terms of the versatility of the structures that can be obtained and the simplicity of the two processes.

Here we present this combined method for constructing an array of isolated Cu^{2+}-complexed organic particles on a SiO_2 substrate and the extension of this array to a continuous network. A hexagonally packed monolayer of polystyrene nanospheres (Figures 2.1(a), 2.2) is used as a shadow mask for metal evaporation onto the substrate. After evaporation, dissolution of the nanospheres leaves an array of triangular metal particles on the SiO_2 substrate (Figures 2.1(c), 2.3), which are then used as parent structures for the molecular ruler process to create a new nanostructure pattern (Figures 2.1(d-f), 2.4, 2.5). Using a subsequent gold-evaporation step followed by dissolution (lift-off) of the organic layers, a new array of gold-star structures is formed within the original gold dot array (Figures 2.6, 2.7).

2.2 Experimental Details

2.2.1 Preparation of Nanosphere Monolayers

Suspensions of unfunctionalized polystyrene spheres of diameter 240-1000 nm (Bangs Laboratories) were diluted (1:2) by a 1:400 solution of Triton X-100 (Sigma-Aldrich) in methanol (VWR) [15]. After dilution, the nanosphere suspensions were spin-coated onto isopropanol-cleaned, oxidized Si wafers with areas between 0.5 cm^2

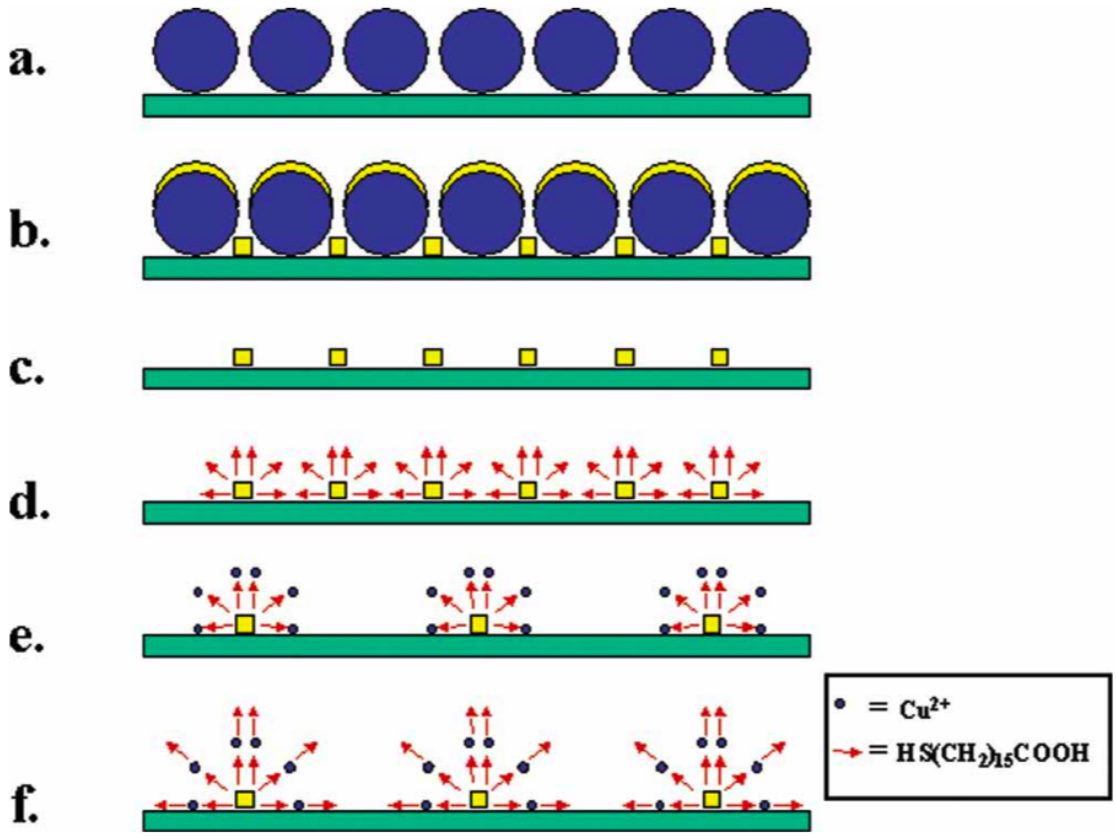

Figure 2.1: Fabrication scheme: (a) Nanospheres deposited on SiO_2 surface, (b) metal evaporation onto the spheres and into the layer gaps, (c) dichloromethane dissolution of the nanospheres, (d) adsorption of $SH(CH_2)_{15}COOH$ (arrows) monolayers, (e) Cu^{2+} ion (small dots) complexation to $SH(CH_2)_{15}COOH$ monolayers, (f) adsorption of a second $SH(CH_2)_{15}COOH$ layer on top of a Cu^{2+} layer.

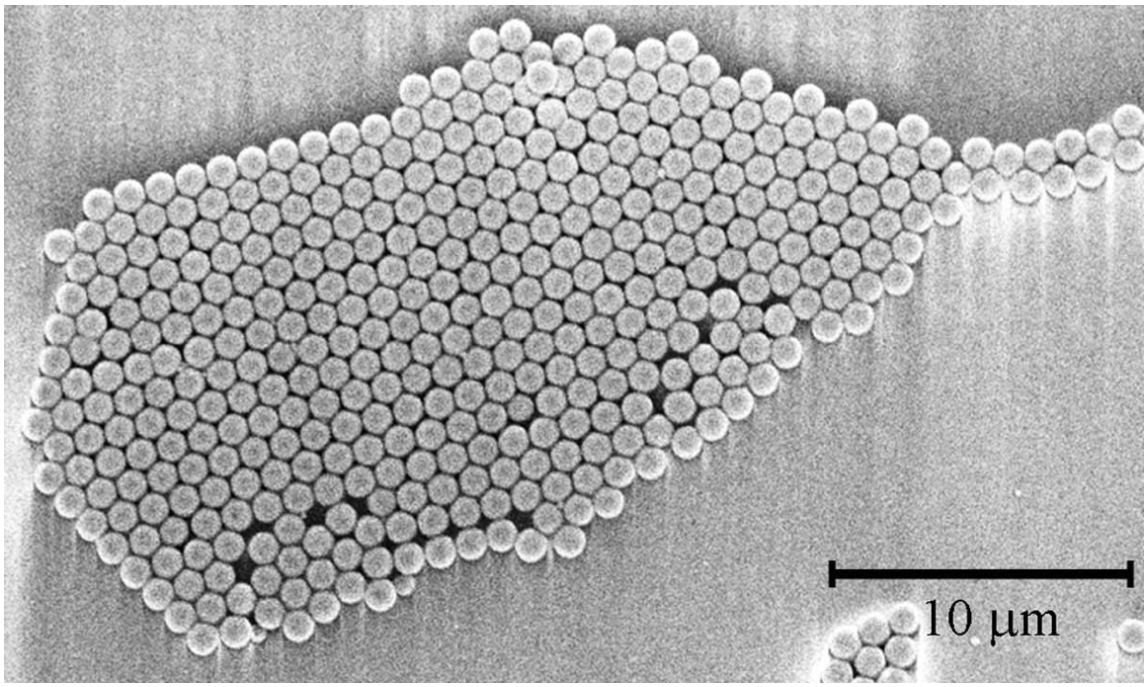

Figure 2.2: FESEM image of an array of close-packed one-micron polystyrene nanospheres formed by spin-coating the nanosphere solution onto a SiO2 substrate. The scale bar indicates 10 μm.

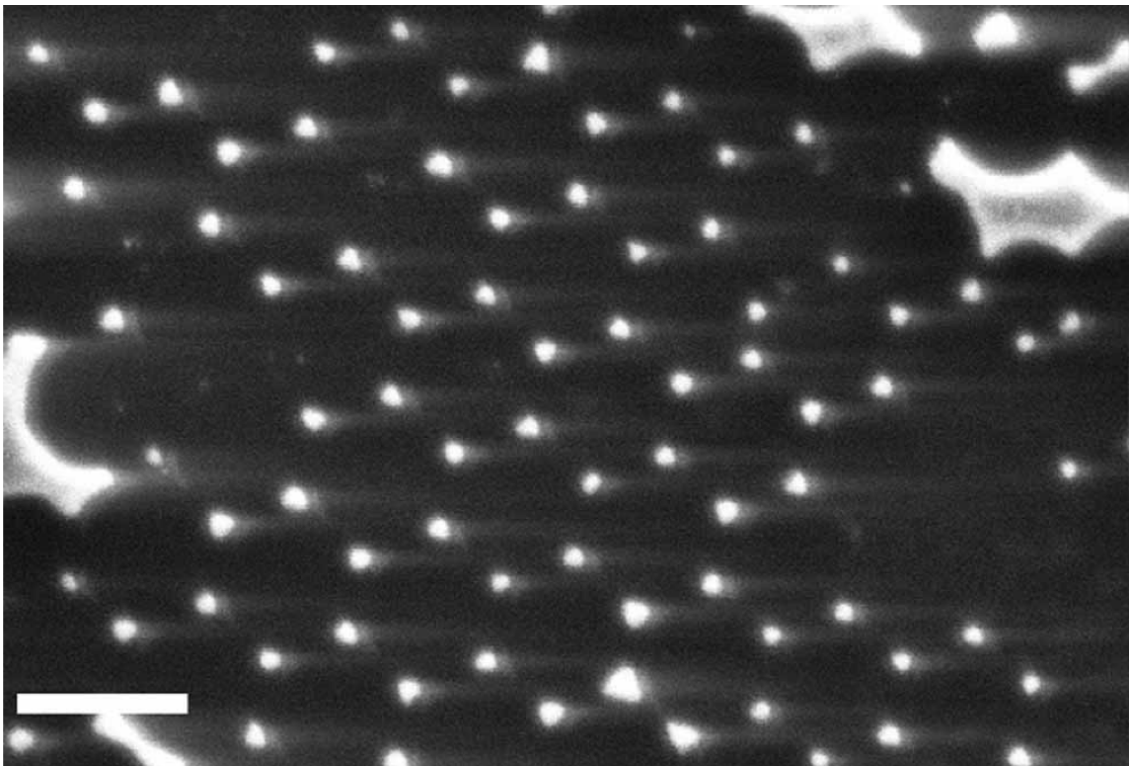

Figure 2.3: FESEM image of an array of Au/Ti particles formed by evaporating the metals through holes in a hexagonally packed 240-nm nanosphere mask. Particle shadow is formed by the FESEM detector position and is not inherent to the sample. The scale bar indicates 250 nm.

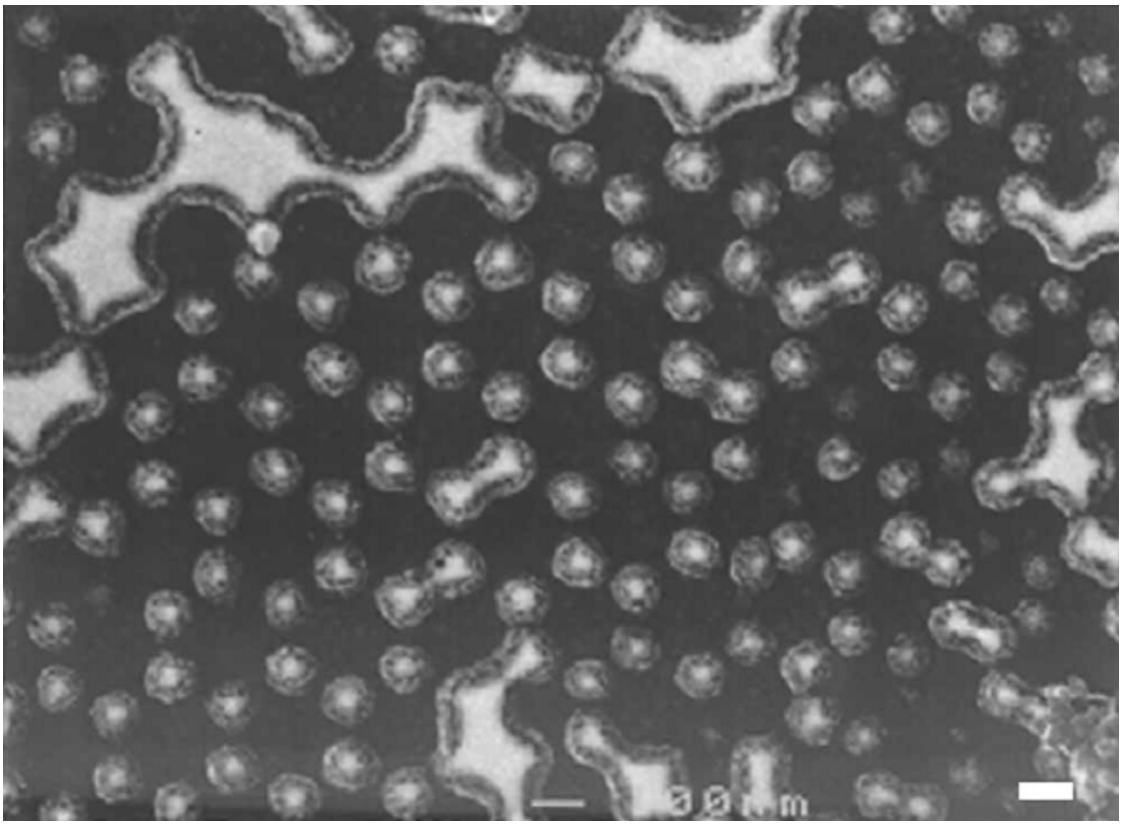

Figure 2.4: FESEM image of 10 layers of Cu^{2+}-complexed 16-mercaptohexadecanoic molecular layers grown on a gold dot array. The sample was coated with 2-nm evaporated gold to enhance SEM contrast and to stabilize the organic structures that are otherwise sensitive to the electron beam. Nanospheres with diameters of 240 nm were used as a mask for this gold dot array. The scale bar indicates 100 nm.

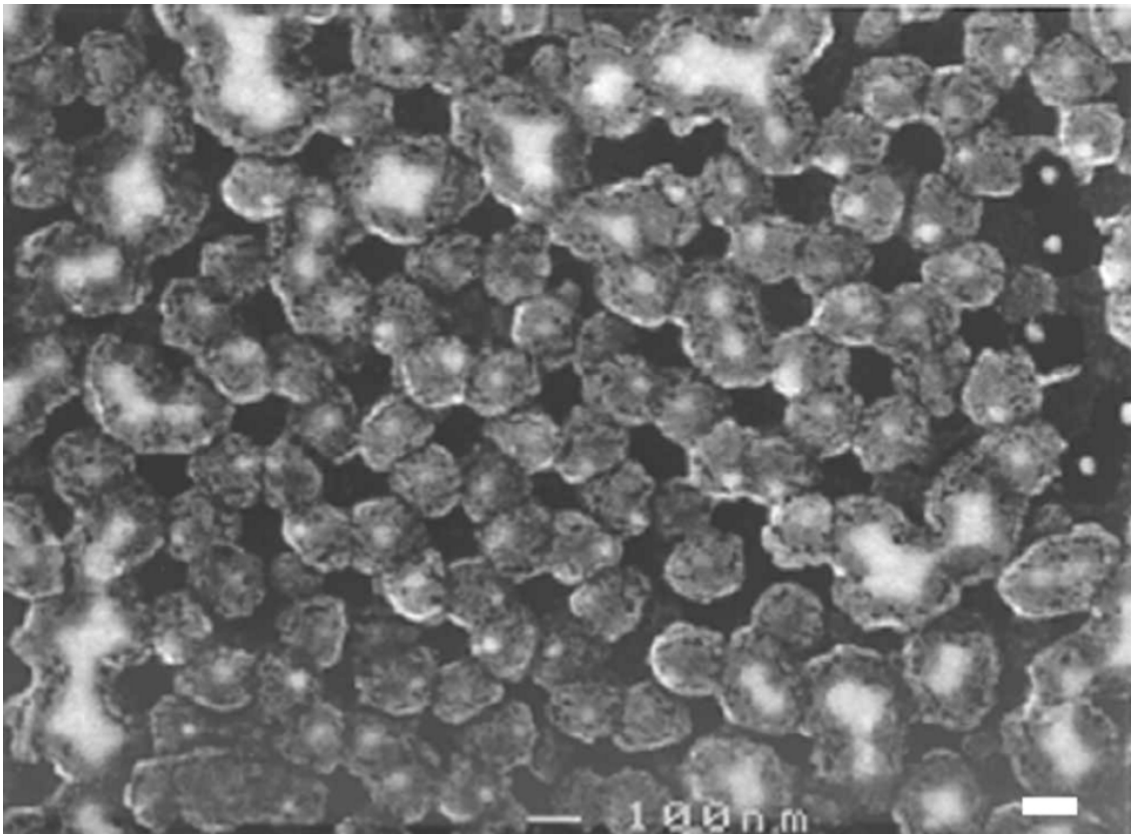

Figure 2.5: FESEM image of 20 layers of Cu^{2+}-complexed mercapto-alkanoic molecular layers grown on a gold dot array. The sample was coated with 2-nm evaporated gold to enhance SEM contrast and to stabilize the organic structures that are otherwise sensitive to the electronbeam. Nanospheres with diameters of 240 nm were used as a mask for this gold dot array. The scale bar indicates 100 nm.

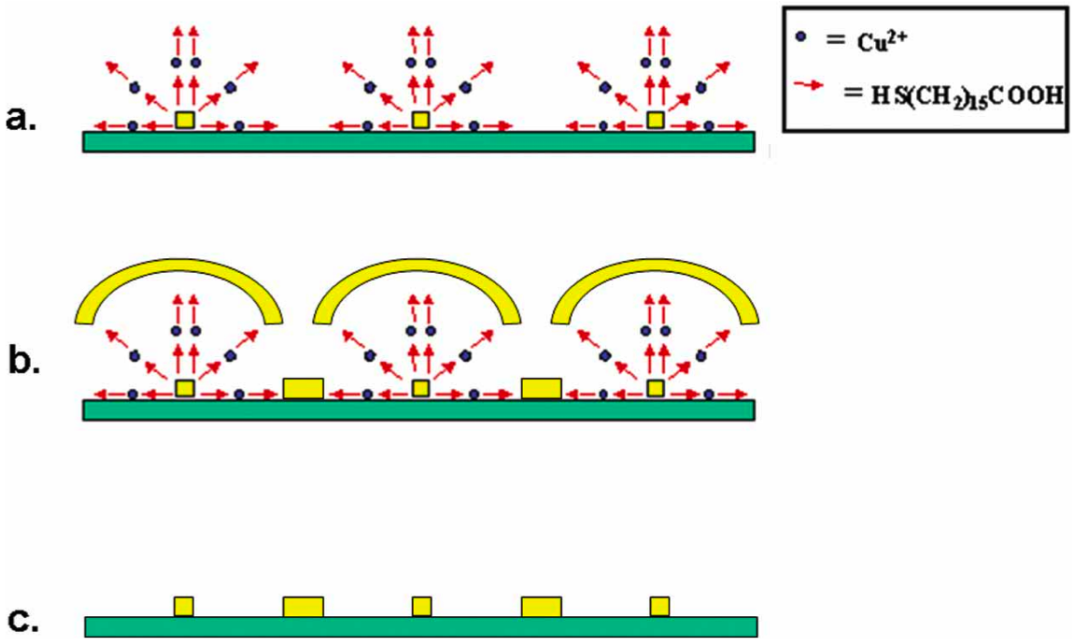

Figure 2.6: Illustration of the second metal-deposition step and removal of the organic structures: (a) The organic multilayer structure on the original gold-dot array as shown in Figure 2.5, (b) gold (with a 2-nm Ti precursor layer) is evaporated on top of the organic layers, and into the gaps between them. In these gaps the gold is deposited directly onto the SiO_2/Si surface, (c)the organic layers and the gold on top of it are removed in an organic solvent [14], to leave only the original gold structures and the new daughter gold structures on the surface. The squares represent the original gold dot structures and the rectangles represent the star-shaped new gold structures as shown in Figure 2.7.

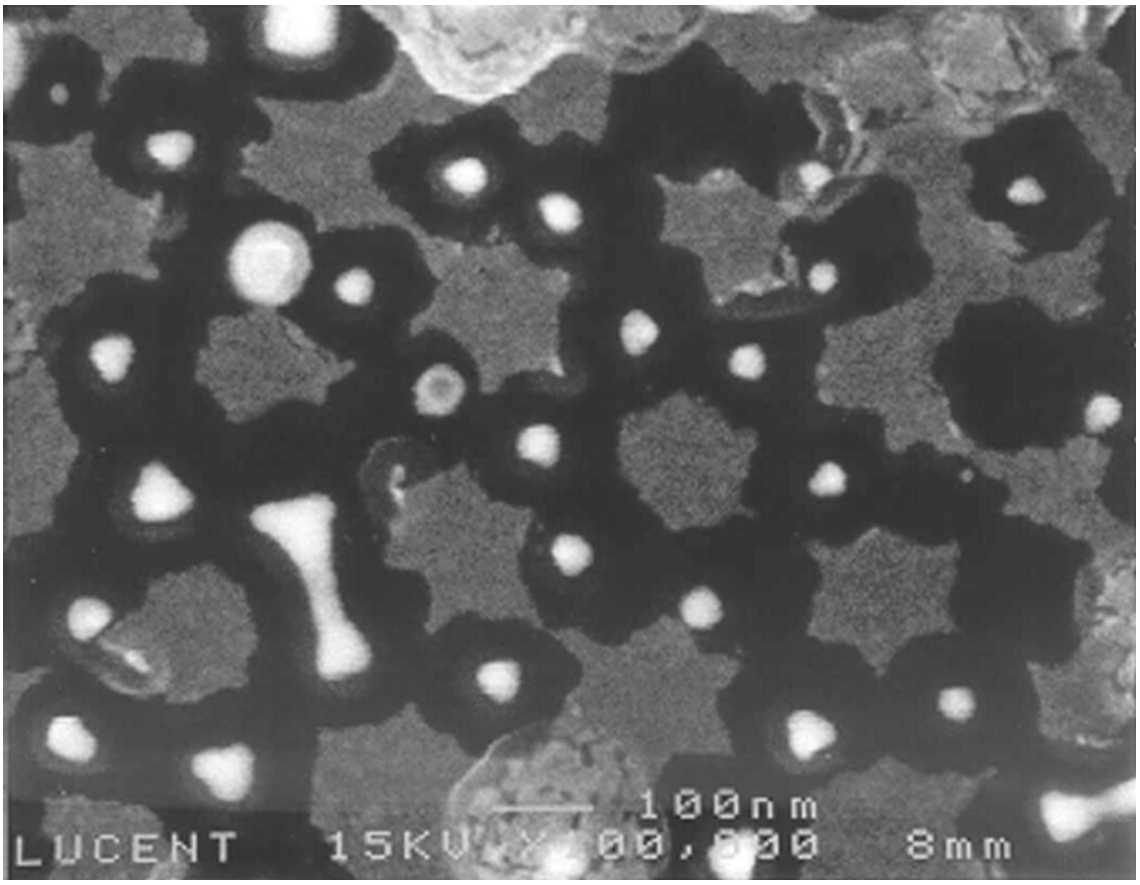

Figure 2.7: Subsequent gold deposition on the sample shown in Figure 2.5, followed by organic layer removal to form an array of star-shaped nanostructures within the original gold-dot array. The scale bar indicates 100 nm.

and 2.0 cm^2. The nanospheres were deposited using a spincoater (Headway Research Inc., Model CB15) operated at $\sim$ 500 rpm for 2 min. Excess fluid at the perimeter of the wafers was wiped dry. A 40-sec O_2/Ar reactive ion etching (RIE) was performed (Plasma-Therm 720RIE, SLR Series) to remove surfactant residues remaining in interstices of the sphere monolayer; this step is crucial to the adhesion of the metal deposited on the SiO_2 surface.

2.2.2 Preparation of Primary Metal Structures

The monolayer was then used as a mask (Figures 2.1(a-b), 2.2), first for electron gun evaporation of a 6-nm Ti underlayer, followed by thermal evaporation of a 40-100-nm Au layer (Kurt J. Lesker E-gun/Thermal Evaporator). Subsequent removal of the nanospheres by sonication in CH_2Cl_2 (J. T. Baker) for 2 min [15] left a hexagonal array of 40-nm-wide metal particles on the substrate (Figures 2.1(c),2.3).

2.2.3 Preparation of Secondary Metal Structures

Coordinated metal ion-organic multilayers [20-24] were adsorbed on the metal dots, by alternate deposition of 16-mercaptohexadecanoic acid (SH-$(CH_2)_{15}$-COOH, Aldrich), 1mM in ethanol and Cu^{2+} ions ($Cu(ClO_4)_2$, Aldrich), 1mM in ethanol [25]. Adsorption times for the organic molecules ranged from 4 h to overnight. Cu^{2+} adsorption time was 3 min. Samples were rinsed by ethanol and dried under a nitrogen stream between all adsorption steps and after adsorption was completed. Here, 10 or 20 such layers (each layer consists of one organic molecule plus one Cu^{2+} ion) were adsorbed on different samples (we have successfully used this technique with

3-30 layers in prior work [20]). The linear growth of the layers was verified using ellipsometry: the thickness of each additional layer grown on gold thin films was measured and was identical to all other layers (2.0 ± 0.2 nm) [25]. X-ray photoelectron spectroscopy (XPS) measurements were conducted as an independent characterization technique to verify the organic layer contents. The XPS atomic concentrations of the various chemical elements (i.e. C = 84.2%, O = 6.9%, S = 4.7%, Cu = 3.7% [±0.2]) reflect precisely the composition of the layers considering small (¡1%) sulfur contaminations that are always present in such samples. 0.5% of Au was found as well, as expected from the underlying gold surface. For FESEM imaging, the samples were coated by 2 nm of evaporated gold. Field emission scanning electron microscope (FESEM) images were taken using a Leica LEO 1530 FESEM and a JEOL JSM-6300F FESEM. For the construction of the gold-star daughter structures (Figures 2.6,2.7) we evaporated 2 nm of Ti followed by 10 nm of Au on top of the organic structures shown in Figure 2.5. This evaporation was followed by dissolution (lift-off) of the organic layers in an organic solvent, as described previously [20].

2.3 Results and Discussion

2.3.1 Primary Got Dot Arrays

Figure 2.1 is a scheme showing the various steps required for the build-up of the metal ions/organic nanostructure array. Figures 2.2-2.5 are FESEM images showing the samples at these various process steps. Figure 2.2 shows an array of 240-nm diameter nanospheres arranged on the Si/SiO_2 surface. This regular pattern was

formed by self-assembly of the spin-coated spheres. At the junction between every three neighboring spheres, the gap is large enough to allow evaporated gold atoms to penetrate and to reach the underlying Si/SiO_2 surface. When gold is evaporated on top of this sphere array, it covers the tops of the spheres and enters into the gaps, as shown in Figure 2.1(b). Figure 2.3 shows the sample after gold evaporation and subsequent removal of the spheres using sonication. The triangular gold dot array reflects the small junction areas between every three adjacent spheres. The shapes of the gold dots are close to triangular, as expected from such sphere geometry. The size of each gold dot is 40 nm which is expected and dictated by the diameter of the nanospheres. This step in the process is illustrated in Figure 2.1(c).

2.3.2 Organic Multilayer Assembly

Figures 2.4 and 2.5show the selective assembly of the organic multilayers on the gold dot array. As illustrated in Fgure 2.1(d-f), this growth is conducted by exposing the surface to a solution of the long organic molecules that self-assemble onto the gold forming a monolayer. The sample is then rinsed and inserted in a solution of the Cu^{2+} ions that serve to link two layers of organic molecules. The sample is rinsed again and placed in the organic molecule solution, and this process is repeated to form the desired number of layers on the surface.

Figure 2.4 shows a FESEM image of a sample coated with ten metal-ion-complexed organic layers. Ten complexed organic layers are expected to yield 20-nm-thick coating since each layer is 2 nm thick. The FESEM image reflects this expected thickness of ca. 20 nm grown off of the gold dots. Figure 2.5 is a similar image of a different

sample coated with 20 layers of the complexed organic molecules. Here the thickness of the layers was ca. 40 nm, corresponding to the length of each molecular layer (2nm) multiplied by the number of layers formed (20 layers). In this image it can be seen that multilayers grown from adjacent gold patterns reached each other and closed the gap completely. The original gap size of 80 nm between two neighboring gold structures was then covered by the two 40 nm organic growth areas originating from each dot. In some of these crossing areas, gaps of less than 10 nm appeared to remain, although growth in other areas persisted. This might be attributed to diffusion limitations of molecules into these thin gaps. The gold dots can be seen inside each structure. Note that in Figure 2.5 the gold dots are not always centered within each structure, yet the organic multilayers followed a periodic array. It might be that the gold array in the imaged area was not totally symmetric prior to molecular adsorption (note irregular spacings between parent structures in some areas of Figure 2.3). Nevertheless, the diffusion limitations of adsorption caused by neighboring growing clusters have the effect of healing this initial asymmetry. The holes (dark) appearing in the images might be areas of incomplete growth between adjacent growing clusters. Structure deformation under the SEM beam is excluded by the evaporation of 2-nm gold layer on top of the structure prior to imaging (Figure 2.4,2.5 captions). Imaging of different samples without the 2-nm gold adlayer shows identical structures with lower image contrast.

The growth of the organic layers from a well-defined gold dot array enables direct imaging of the organic multilayer formation in its initial steps. By reducing the dimensions of the gold nucleating centers and by using various functional organic

molecules withor without metal ions, a large number of organic nanoparticles can be created. Hybrid inorganic/organic or pure inorganic clusters can be similarly formed [26]. The organic nanoparticles formed complement the family of inorganic nanoparticles studied to date (see ref. [27] and references therein). The fabrication technique demonstrated here can be used to create nucleation centers for studying crystal growth mechanisms. The molecular ruler procedure is highly applicable for creating novel patterned surfaces for optical and electronic devices.

2.3.3 Secondary Metal Deposition

As illustrated in 2.6, the process shown above was further used to create more complex structures on the surface. This was done by starting with the nanostructures shown in Figure 2.5.The organic layers served as a mask for a second gold deposition step (Figure 2.6(b)). Gold deposition was followed by the removal of the entire organic layer structure in an organic solvent (Figure 2.6(c)) [20]. The result was an array of star-shaped structures that formed between the original gold dot array. This array is shown in Figure 2.7.

The gaps between the stars and the original gold-dot array reflect the area that was previously covered by the organic layers. The second metal deposited is not restricted to gold. Therefore, structures with two different metals can be formed where the two metals are in very close proximity (40 nm in this case). Such two-metal geometries are hard to achieve using conventional lithographic techniques. The shapes and sizes of these daughter nanostructures can be controlled easily using organic molecules of various lengths and by choosing the desired number of organic layers deposited.

2.4 Conclusion

We have shown the controlled uniform growth of organic multilayers from a periodic gold dot array on SiO_2 surfaces. This special geometry enables imaging of the metal-organic structure formation in its initial stages. This process can be used to fabricate new organic/metal nanostructures for possible uses in electronic or optical devices. The layer-by-layer growth can yield an isolated organic dot structure on a continuous surface or a continuous organic network exposing only an isolated array of surface dots. The molecular ruler technique enables the formation of novel and complex nanostructure arrays. The fine structure design depends on the initial dot spacing, the length of the organic molecule chosen and on the number of layers grown. Each of these parameters can be easily modified. The combination of NSL and the molecular ruler technique for creating nanostructure arrays is shown to be a very simple fabrication method. It offers great versatility in shape, in structure and in material combination.

Chapter 3

Electrical Programmability

3.1 Introduction

Programmability in electronic systems originates from the ability to form and reform nonvolatile connections. Devices in modern programmable architectures typically derive this ability from controlled internal changes in material composition or charge distribution [28]. However, for bottom-up nanoelectronic systems it may be advantageous to derive programmability not only from internal state, but also from the mechanical manipulation of mobile components. Proposed applications that require component mobility include neuromorphic networks of nanostructure-based artificial synapses [29], breadboards for rapid prototyping of nanodevice circuits [30, 31], and fault-tolerant logic in which broken subsystems are replaced automatically from a reservoir [32]. In this paper, we take the first step of demonstrating that interconnects, the simplest nanoelectronic components, can be assembled, reconfigured, and disassembled by an electromechanical process.

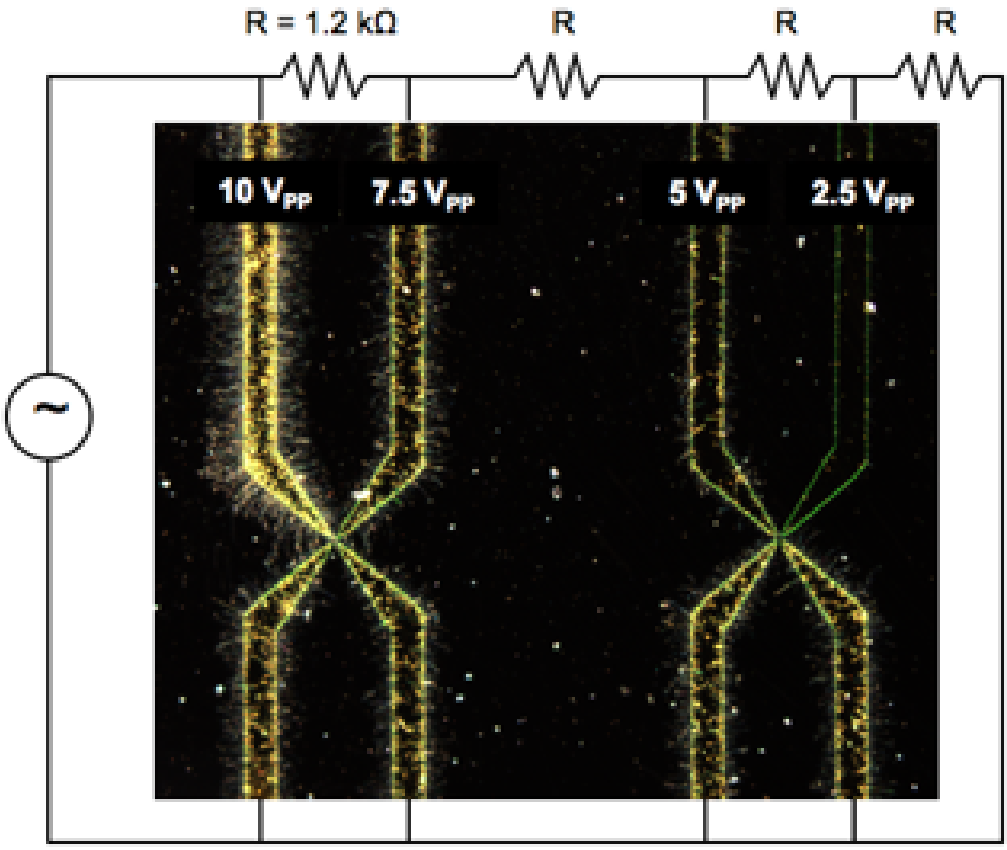

Figure 3.1: Dark-field microscope image demonstrating the trapping of large numbers of nanostructures, which are visible as lines perpendicular to the electrode faces, at relatively low voltages.

Various approaches for manipulating electronic nanostructures have been developed, including mechanical [33], optical [34, 35], electrostatic [36, 37], and dielectrophoretic [38] methods. Dielectrophoresis, in particular, is attractive for inexpensive and massively parallel manipulation [39] of neutral microscale and nanoscale objects using only standard semiconductor fabrication technologies. It has been used to trap a variety of structures from suspensions, including NiSi nanowires [40], CdS nanowires [41], GaN nanowires [42], carbon nanotubes [43], silicon microblocks [44], ZnO nanorods and nanobelts [45, 46], and gold nanowires [47]. An example of the ability of dielectrophoresis to trap nanostructures with relatively low voltages is shown in Figure 3.1. Previous electrical transport measurements of dielectrophoretically trapped structures have been performed either after immobilizing the structures through drying [42, 44-46] or chemical binding [47], or performed over large films of parallel interconnects [43]. In this work we demonstrate for the first time that dielectrophoresis may also be used to reconfigure and disassemble nanowire interconnects and that our process is compatible with the assembly and electronic characterization of individual nanowire devices.

3.2 Experimental Details

3.2.1 Preparation of Nanowire Colloid

For interconnects, p-type silicon nanowires were grown by the vapour-liquid-solid method [48], using 20-nm Au nanocluster catalysts (Ted Pella), and SiH_4 reactant (99.7%) and B_2H_6 dopant (0.3%) in He carrier gas (100 ppm) at 450 torr and 450°C.

Growth was performed for 10-60 min to achieve nanowire lengths of 10-60 μm. The nanowire growth wafer was sonicated lightly in isopropanol for 1 min. The suspension was vacuum filtered using a 12-μm mesh (Millipore Isopore) in order to remove unnucleated Au catalyst particles and short nanowires. The filter mesh was sonicated in isopropanol, and the suspension was again filtered. The second filter mesh was sonicated in benzyl alcohol for 2 min and the suspension was used for trapping experiments. Benzyl alcohol was selected as a viscous, low-vapour-pressure solvent [49] for reconfiguration in order to damp Brownian motion, minimize toxicity [50], and allow ambient operation. Additionally, its static relative permittivity is slightly smaller than that of bulk Si (11.9 versus 12.1, respectively) [49], reducing van der Waals interactions at low frequencies and favouring dielectrophoretic trapping of conductive structures [38]. Heavily-doped silicon nanowires were selected as interconnects to demonstrate potential compatibility of our technique with the assembly of more complex semiconducting nanostructures, such as axial heterostructures [51].

3.2.2 Preparation of Electrode Chip

Trapping experiments were performed with 100-nm Au electrodes (5-nm Cr wetting layer) to avoid oxidative damage, on a Si wafer with a 200-nm oxide to prevent shorts. Thicker electrodes, with reduced fringing fields, were found to better allow nanowires to migrate along their edges toward the trapping region. Thinner electrodes tended to permanently pin nanowires to the top electrode faces wherever they were first trapped. The electrodes were defined by e-beam lithography with a 10° taper angle and a 1-μm tip radius of curvature.

3.2.3 Field Pulse Protocol

The nanowire suspension was pipetted onto the electrode chip to form a 250-μm-thick reservoir, as shown schematically in Figure 3.2(a). For trapping, electrode pairs were biased at 10 kHz to minimize both solvent electrolysis and parasitic capacitance. The bias was modulated into 10-ms bursts at 110 V_{RMS} with a period of 100 ms, which allowed migration of nanowires toward the trapping region in controlled steps. The time between bursts was manually increased to 1000 ms as nanowires approached the inter-electrode region, and the bursts were halted when the desired number of nanowires had been trapped. Movies of nanowire motion were recorded at 4 fps.

3.2.4 Electrical Characterization

Electrical characterization was performed by manually switching the electrodes from the trapping voltage source to a measurement apparatus (Agilent 4156C). A 10-V sawtooth bias at 10 Hz was used and the measured currents were binned by voltage and averaged to remove hysteresis. Nanowire movement in the plane of the chip during transport measurement was minimal, since transport voltages were an order of magnitude smaller than trapping voltages.

3.3 Results and Discussion

3.3.1 Nanowire Trapping

Confirmation that the trapping voltage was not substantially attenuated was provided by observation of a single scattering fringe around the electrodes in dark-field

mode, which was consistent with the "DC" Kerr effect [38] at 155-V peak bias across a 10-μm gap. Nanowires up to 55 μm in length were stably trapped, as shown in Figure 3.2(b), with noticeable bending due to the trapping field inhomogeneity. The longest previously reported one-dimensional nanostructures to be trapped by dielectrophoresis at both ends were less than 15 μm long and showed minimal bending [41]. For larger electrode gaps, nanowires at either tip appeared not to experience significant bending toward the opposite electrode, while shorter gaps caused significant accumulations of wires, as shown in Figure 3.3. Confirmation that the trapping voltage was not substantially attenuated was provided by observation of a single scattering fringe around the electrodes in dark-field mode, as shown in Figure 3.4, which was consistent with the "DC" Kerr effect [38] at 155-V peak bias across a 10-μm gap.

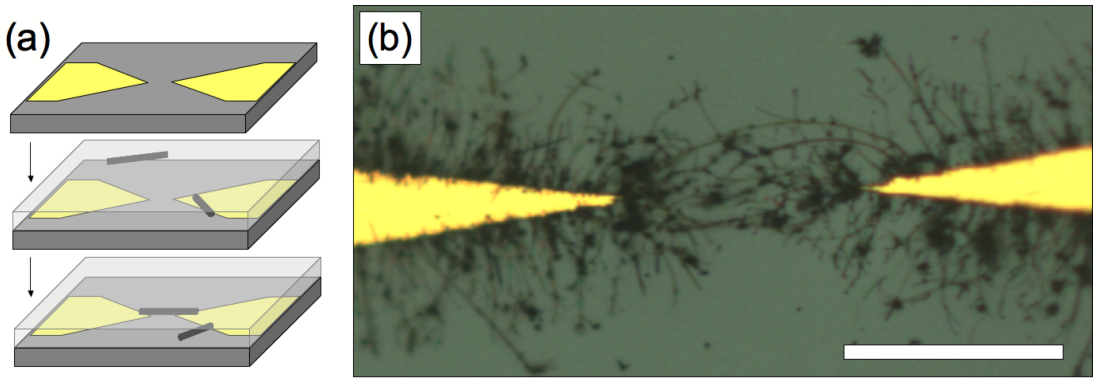

Figure 3.2: Dielectrophoretically trapped nanowires. (a) Schematic illustration of nanowire trapping process. (b) Light microscope image of multiple nanowires stably trapped between electrodes separated by 40 μm. Scale bar is 40 μm.

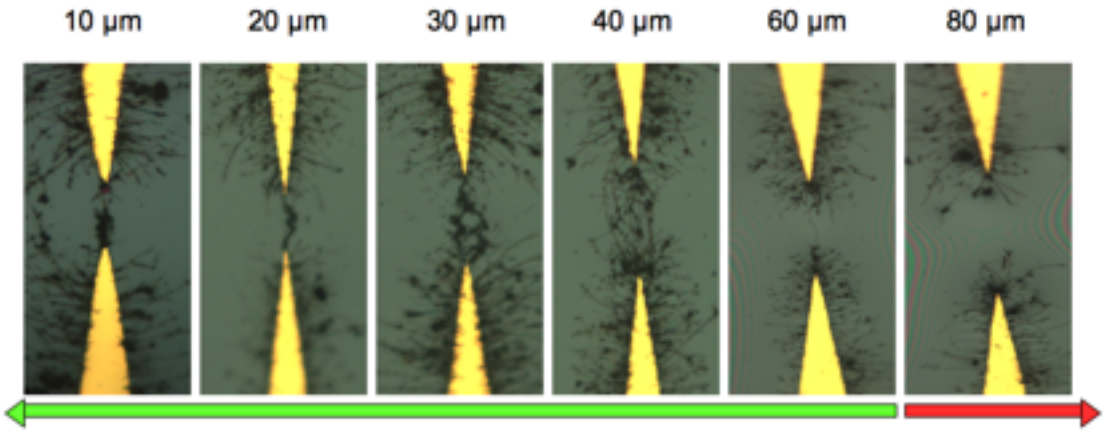

Figure 3.3: Nanowires trapped by electrodes separated by various distances.

3.3.2 Interconnect Assembly and Characterization

The burst method was also delicate enough to enable trapping of individual nanowires when the reservoir was diluted below 2×10^{-13} M, as shown in Figure 3.5(a). Before nanowire interconnects were assembled, DC transport between electrode pairs was nearly ohmic, as shown in Figure 3.5(b). The measured current of 0.3 μA at 1-V bias and 40-V/s sweep rate was consistent with electrooxidation of benzyl alcohol [52, 53] at 1-μm-radius electrode tips. However, after a 50-μm-long nanowire was trapped, the conductance became nonlinear and showed a 50% enhancement at 10-V bias, as shown in Figure 3.5(c). Treating the device as an electrooxidative resistance in parallel with a series nanowire resistance and Schottky contacts [54], a nanowire transport curve was calculated, as shown in Figure 3.5(d). The nanowire exhibited a calculated linear response resistivity of 3.8×10^{-3} Ω·cm (6.0-MΩ resistance), consistent with a B doping ratio of 2000:1, and an estimated barrier potential of 2.0 V. The barrier potential was higher than the 0.34 V measured in evaporated Au/p-Si junctions [55], and is attributed to incomplete contact of the nanowire with the electrodes.

Further confirmation that dielectrophoretically-trapped nanowires acted as interconnects was provided by substituting ethanol as a solvent and permitting the substrate to dry after trapping. A pair of nanowires thus trapped, as shown in Figure 3.6(e), appeared to rest on both electrode faces but initial voltage sweeps yielded a 30-MΩ resistance, as shown in Figure 3.6(f). After several sweeps, however, a sharp current turn-on was observed at 6.8-7.8 V, as shown in Figure 3.6(g), which may indicate electrostatically-induced bending of the nanowires to better contact the electrodes. Above the turn-on bias, the nanowires exhibited a 1.7-MΩ combined

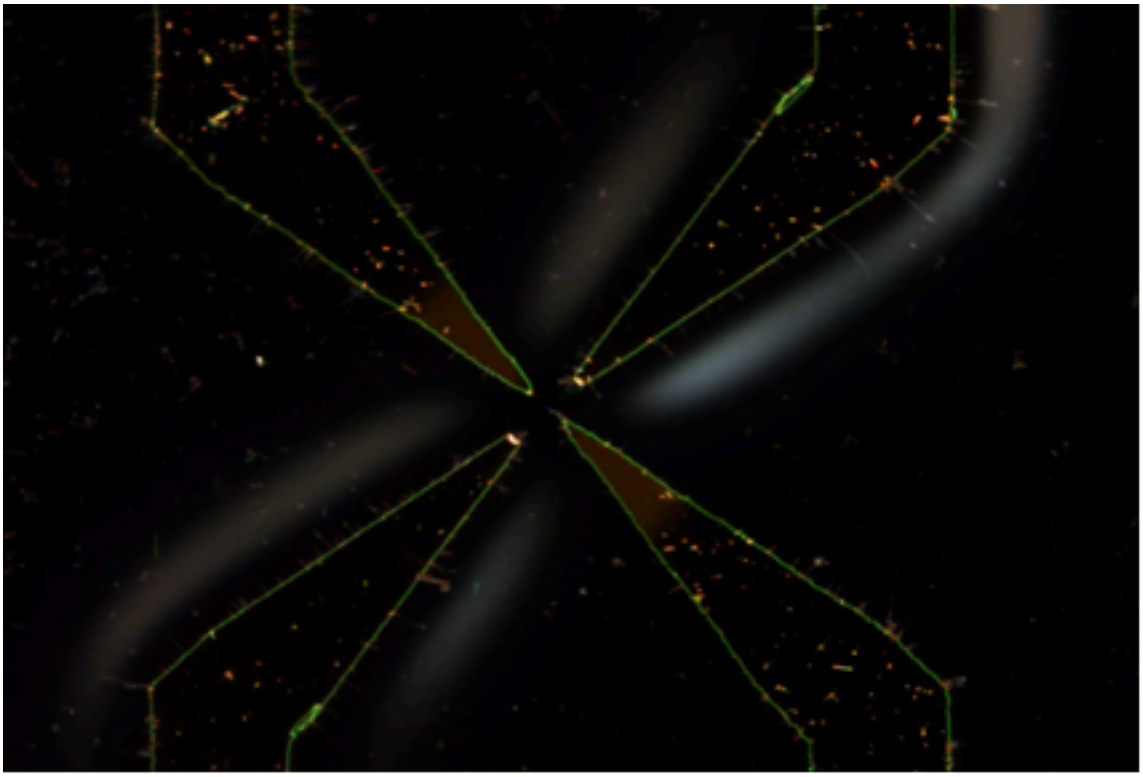

Figure 3.4: Scattering fringes about active electrodes as viewed in dark-field mode, attributed to the DC Kerr effect..

resistance, which is compatible with the solvent-based result.

3.3.3 Serial Interconnect Reconfiguration

The reported method for trapping nanowire interconnects furthermore enabled reconfiguration, since nanowires were maximally polarized when aligned between a pair of electrode tips. Reconfiguration of a nanowire bundle was achieved using 'source' and 'drain' electrodes with opposite phase and a 'latch' electrode with variable phase. Several nanowires were independently trapped between the source and latch electrodes with 100-ms-period bursts, as shown in Figure 3.7(a), and then bundled with 250-ms-period bursts, as shown in Fgure 3.7(b). The phase of the latch electrode was then inverted, with the same burst period, causing the nanowire bundle to experience a dielectrophoretic force toward the drain electrode. Because the electrode tips were arranged in an isosceles right triangle formation, the torque about the latch electrode was higher than that about the source electrode, and the nanowire remained in contact with the latch electrode during the motion, as shown in Figure 3.7(c). The reconfiguration was completed 0.25-0.75 s after the phase inversion, as shown in Figure 3.7(d), and could be reversed by restoring the original phase of the latch electrode, as shown in Figure 3.7(e).

3.3.4 Parallel Interconnect Reconfiguration

Similarly, parallel reconfiguration of a pair of nanowire interconnects was achieved with four electrodes in a 10-μm square, as shown in Figure 3.8. To accomplish this, the relative phases between diagonally opposite electrodes were fixed and the relative

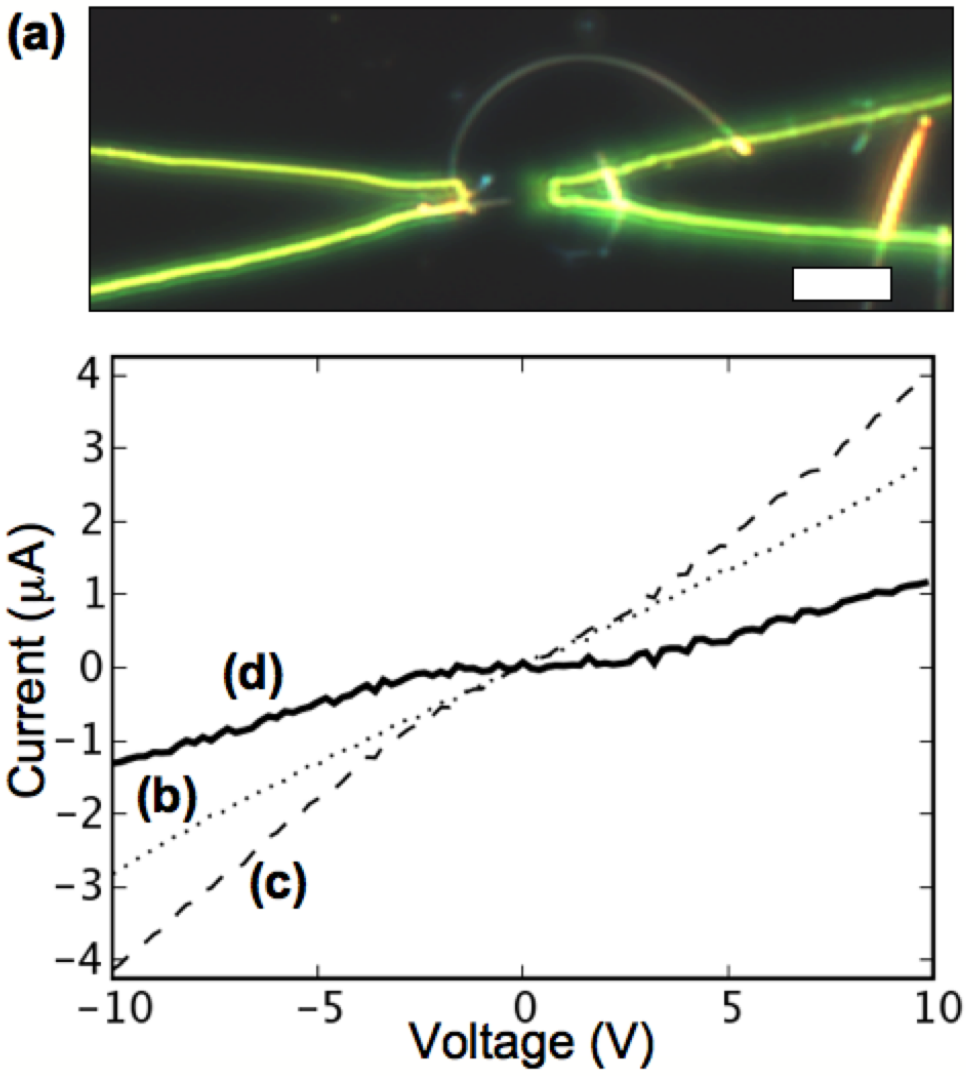

Figure 3.5: Electrical transport in trapped nanowires. (a) Dark-field microscope image of a single nanowire trapped by an electrode pair under solvent with electrical transport (b) measured with solvent, (c) measured with trapped nanowire in solvent, and (d) calculated for nanowire alone. Scale bars are 10 μm.

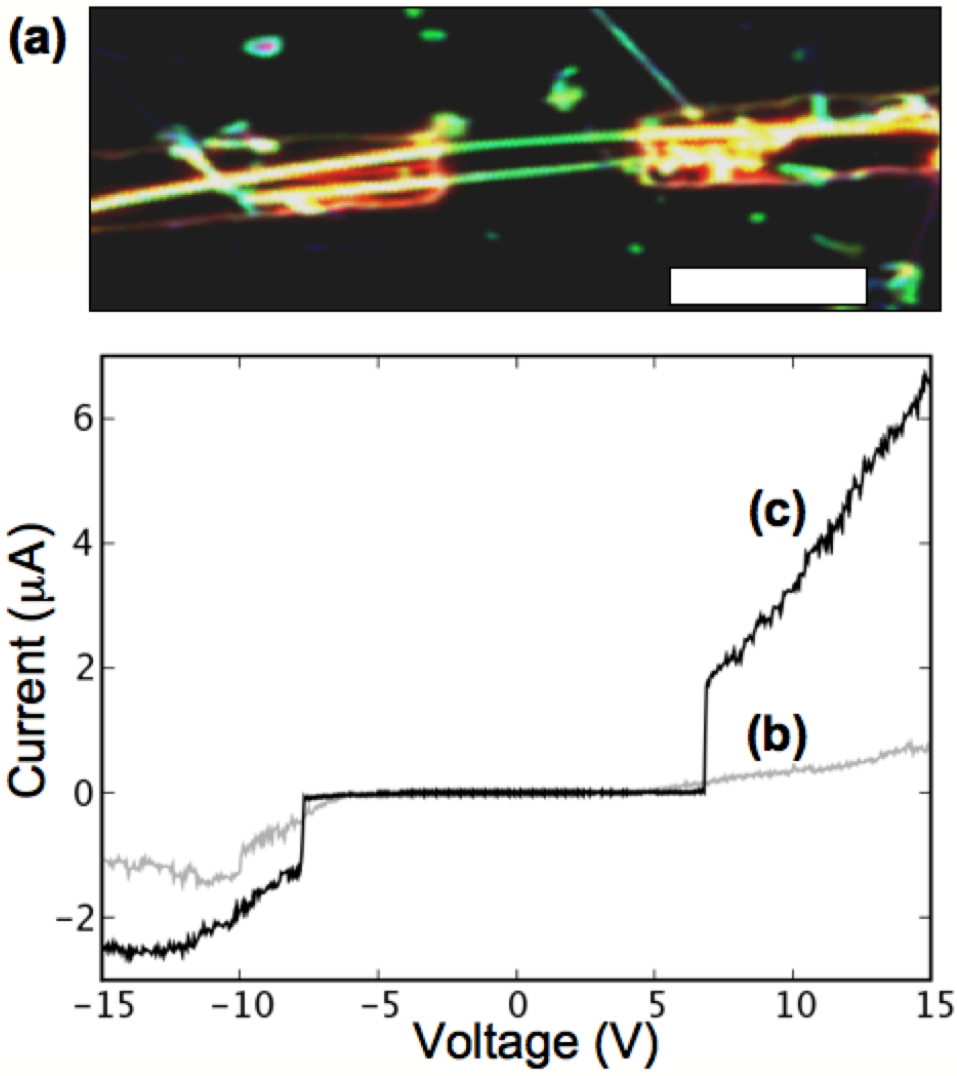

Figure 3.6: Electrical transport in trapped nanowires. (a) Dark-field microscope image of two trapped nanowires on dried substrate with electrical transport measured (b) immediately after drying and (c) after several voltage sweeps. Scale bars are 10 μm.

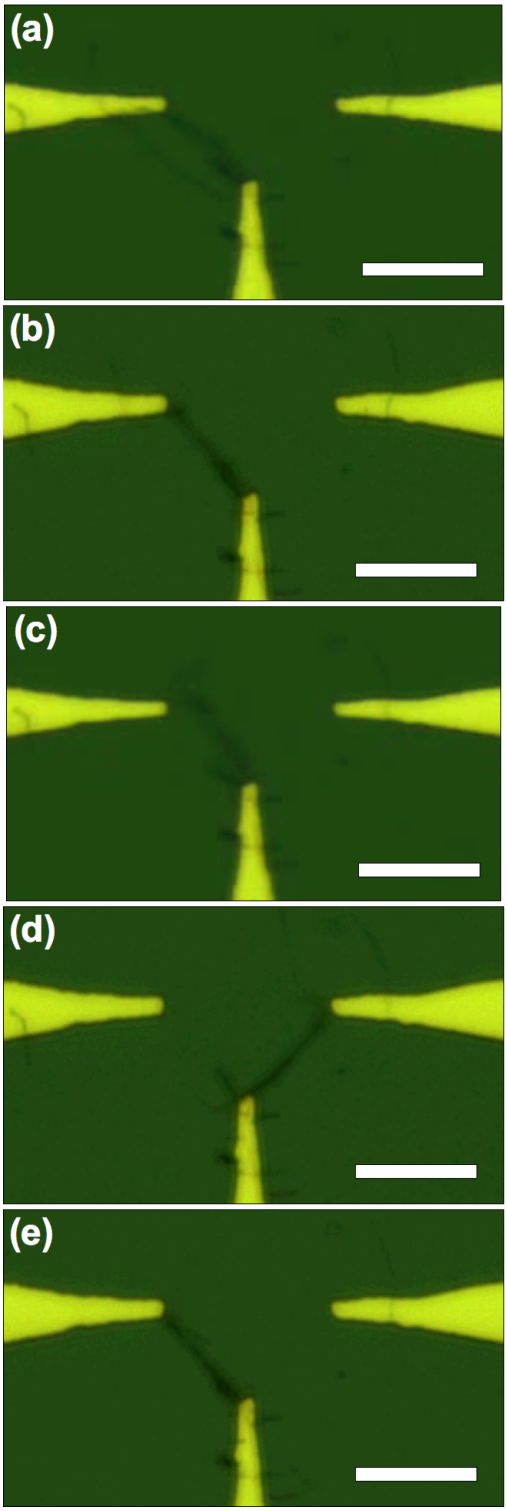

Figure 3.7: Microscope images of 3-electrode serial reconfiguration of nanowires. The relative phase between the left (source) and middle (latch) electrodes is modulated from (a,b) 180° to (c,d) 0° to (e) 180°. Scale bars are 15 μm.

phase of the diagonal pairs was inverted. Dielectric breakdown of some nanowires occurred and short fragments were visible around the connecting nanowires.

3.3.5 Comparison to Theory

For theoretical comparison, we now calculate how rapidly a nanowire might be dielectrophoretically reconfigured. The dielectrophoretic force per unit length on a cylindrical nanowire with length l_{wire} and diameter d_{wire} is given by

$$F_{\text{dep}} = \frac{1}{8}\epsilon_{\text{solv}}\pi d_{\text{wire}}^2 \Re\left\{\vec{K}(f)\cdot\vec{\nabla}(\vec{E}^2)\right\}\hat{\nabla}(\vec{E}^2),$$

where ϵ_{solv} is the solvent permittivity and $\vec{K}(f)$ is the frequency-dependent Clausius-Mossotti factor [38]. For $l_{\text{wire}} \gg d_{\text{wire}}$, the Clausius-Mossotti component perpendicular to the nanowire axis is approximately

$$K_{\perp} = \frac{\tilde{\epsilon}_{\text{wire}} - \tilde{\epsilon}_{\text{solv}}}{\tilde{\epsilon}_{\text{solv}}(1-\frac{\pi}{8}) + \tilde{\epsilon}_{\text{wire}}(\frac{\pi}{8})},$$

where $\tilde{\epsilon}_{\text{X}} \equiv \epsilon_{\text{X}} - \text{i}\sigma_{\text{X}}/(2\pi f)$ are the complex permittivities of nanowire and solvent (the solvent is assumed to be non-conductive at trapping frequencies). Approximating the gradient of the field energy density in the inter-electrode space as uniform, $\nabla(\vec{E}^2) \sim V_{\text{sd}}^2/L^3$, where L is the distance between electrode tips.

The dielectrophoretic force is opposed by Stokes drag. The drag coefficient for an infinitely long, cylindrical nanowire [56] is given by

$$C_{\text{D}} \equiv \frac{F_{\text{drag}}}{\frac{1}{2}\rho_{\text{wire}}u^2 d} \approx \frac{8\pi}{Re\,(2.002 - \ln Re)},$$

where F_{drag} is the drag force per unit length, ρ_{wire} is the nanowire density, u is the nanowire velocity, and $Re \sim d\rho_{\text{solv}}u/\mu$ is the Reynolds number for solvent density ρ_{solv}

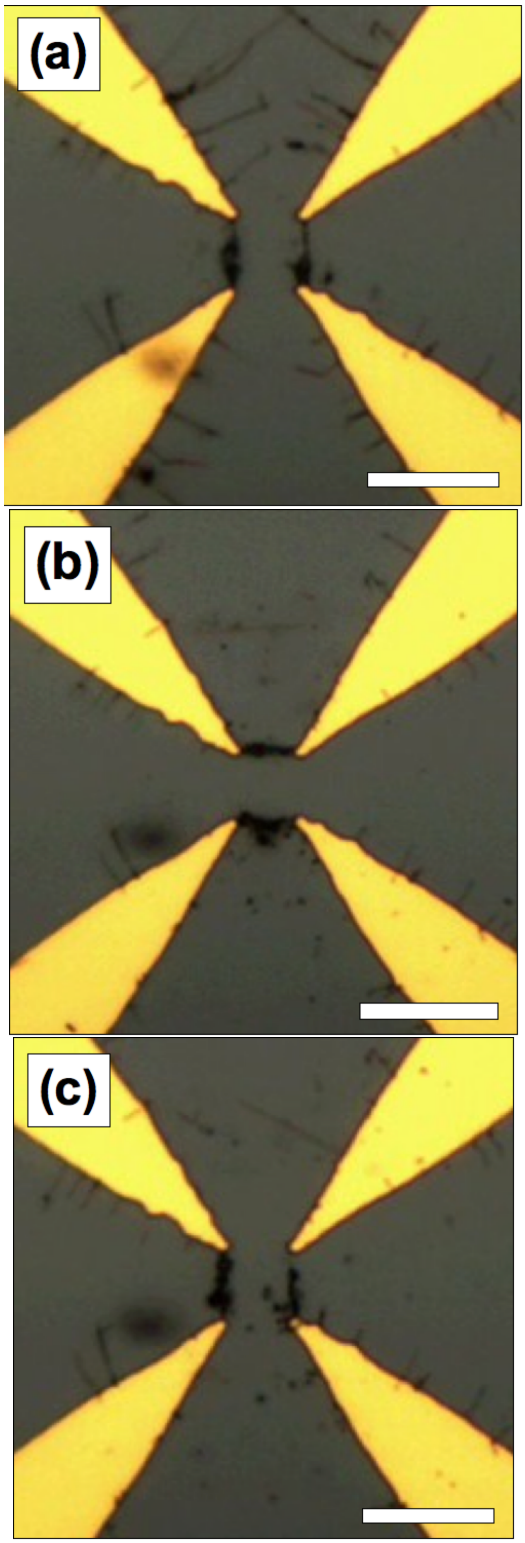

Figure 3.8: Microscope images of 4-electrode parallel reconfiguration of nanowires. Each pair of diagonally opposite electrodes is held at a constant relative phase of 180°, while the relative phase between the upper-left and upper-right electrodes is modulated from (a) 0° to (b) 180° to (c) 0°. Scale bars are 20 μm.

and dynamic viscosity μ. Assuming bulk mechanical properties of silicon and benzyl alcohol [49] and matching drag and dielectrophoretic forces, the terminal velocity during switching perpendicular to the nanowire axis is calculated to be $u_{\perp} \approx 30$ μm/s, implying a 0.3-s reconfiguration time. This time is consistent with the serial reconfigurations observed, validating our model.

3.3.6 Interconnect Disassembly

Finally, it should be mentioned that electrically-driven nanowire disassembly was also found to occur. In an example of this effect, a single nanowire that was initially trapped on one electrode, as shown in Figure 3.9(a), was pulled into the inter-electrode region and a gas bubble immediately formed there, as shown in Figure 3.9(b). After the bubble dispersed, only short nanowire fragments remained, as shown in Figure 3.9(c). This effect was observed for about 1/3 of the nanowires trapped in inter-electrode regions and might be explained by variation in the nanowire conductivities and/or the formation of exceptionally good contacts, which could lead to current densities as high as 5×10^{10} A·m^{-2} and thermal detonation. After the original nanowires were destroyed, the inter-electrode regions were typically able to trap new interconnects, so this effect might prove useful in fault-tolerant applications for severing connections to non-functioning components.

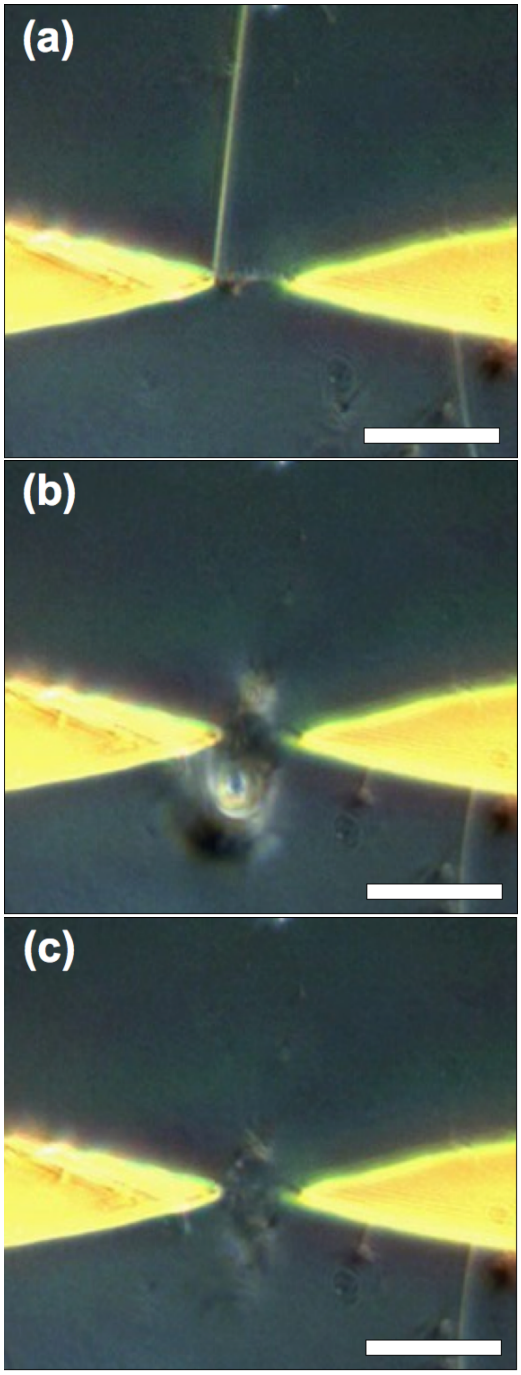

Figure 3.9: Disassembly of nanowire interconnects by thermal detonation. (a) Stably trapped nanowire before detonating voltage pulse. (b) Vapour bubble resulting from thermal detonation. (c) Only sub-micron fragments remain. Scale bars are 20 μm.

3.4 Conclusion

3.4.1 Summary

The first assembly, reconfiguration, and disassembly of nanowire interconnects through dielectrophoresis has been demonstrated. Silicon nanowires up to 55 μm long were trapped, and solvent-based transport studies show a 50% conductivity enhancement in the presence of the nanowires. Once assembled, these nanowire interconnects could then be reconfigured and disassembled using periodic voltage bursts. These results open up the possibility of colloidal, nanostructured connection architectures for computation. With our discussion of individual component reconfigurability concluded, we now advance to such an exploration of the feasibility of larger-scale dielectrophoretic architectures. For dielectrophoresis to find real-world applications to nanocomputation, logic at least at the gate level must be demonstrated.

3.4.2 1×1 Crossed Interconnects

Earlier, we described the reconfiguration of interconnects geometrically occupying single sides or pairs of sides of a square. As a next step toward larger-scale architectures, we should also consider interconnects that do not lie on the circumference of the trapping region, but instead span it. In particular, we may estimate the value of the term ∇E^2 , which is crucial to the dielectrophoretic strength, for either type of configuration, as shown schematically in Figure 3.10.

Recall that we may approximate the trapping force by assuming a uniform electric field gradient near the energy minimum. Therefore, for the geometry shown in

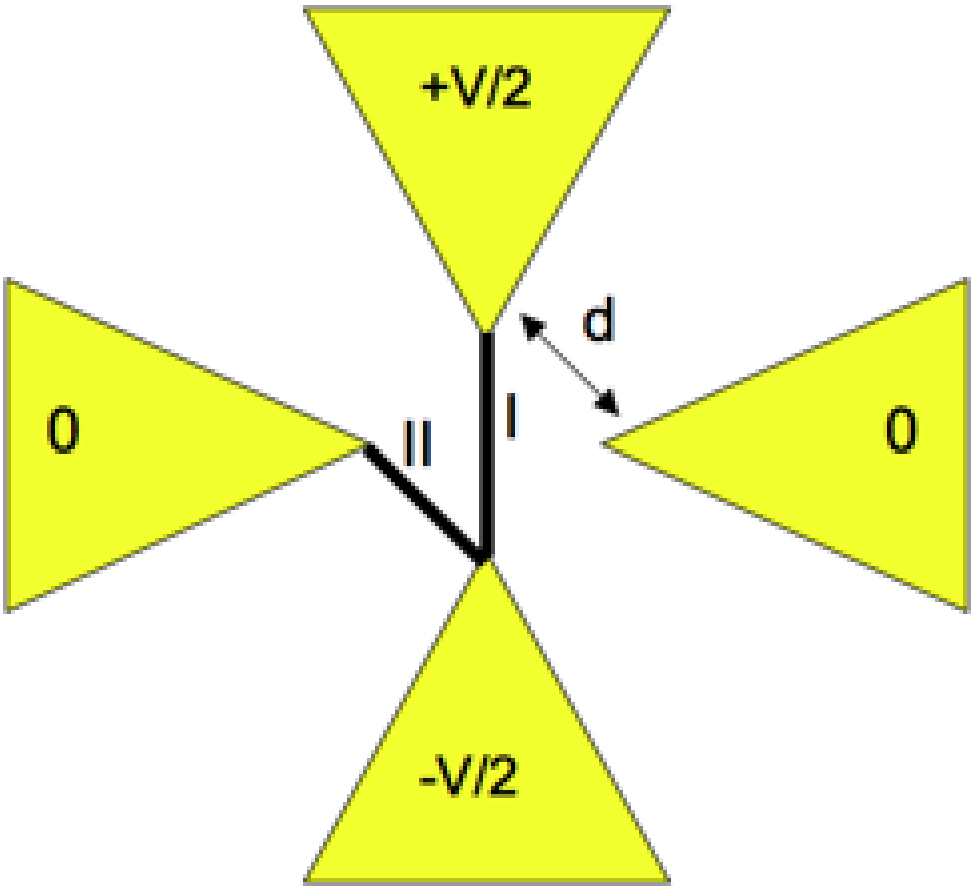

Figure 3.10: Schematic diagram for circumferential (II) versus non-circumferential (I) interconnects in a 1×1 crossbar.

Figure 3.10, for the non-circumferential interconnect (I),

$$\nabla E^2 \sim (V)^2/(d\sqrt{2})^3 = \frac{1}{2^{3/2}} \cdot \frac{V^2}{d^3}$$

, and for the circumferential interconnect (II),

$$\nabla E^2 \sim (V/2)^2/(d)^3 = \frac{1}{2^2} \cdot \frac{V^2}{d^3}$$

. Since the value is larger for the non-circumferential case, stable trapping of diagonal interconnects should be possible. (There is suggestive experimental data that stable diagonal interconnects can indeed be achieved [46], although the substrate in that case was dried before imaging.) Moreover, since $K_\perp \ll K_\parallel$, a short field burst perpendicular to an existing wire should not disrupt it.

3.4.3 2×2 Crossbar

We can perform a similar, albeit more entailed, analysis to determine the feasibility of stable non-circumferential interconnects in larger crossbars, such as the 2×2 geometry we now consider.

For the specific octagonal electrode tip geometry and voltages shown in Figure 3.11, we can calculate all force values ($F \equiv \nabla E^2$):

$$\frac{F_2}{F_1} = \frac{\left(\frac{1}{2} - a\right)^2}{\left[\frac{1}{\sqrt{2}}(1-p)\right]^3},$$

$$\frac{F_3}{F_1} = \frac{(2a)^2}{p^3},$$

$$\frac{F_4}{F_1} = \frac{\left(\frac{1}{2} + a\right)^2}{\left[\sqrt{\frac{1}{2} + \frac{p^2}{2}}\right]^3},$$

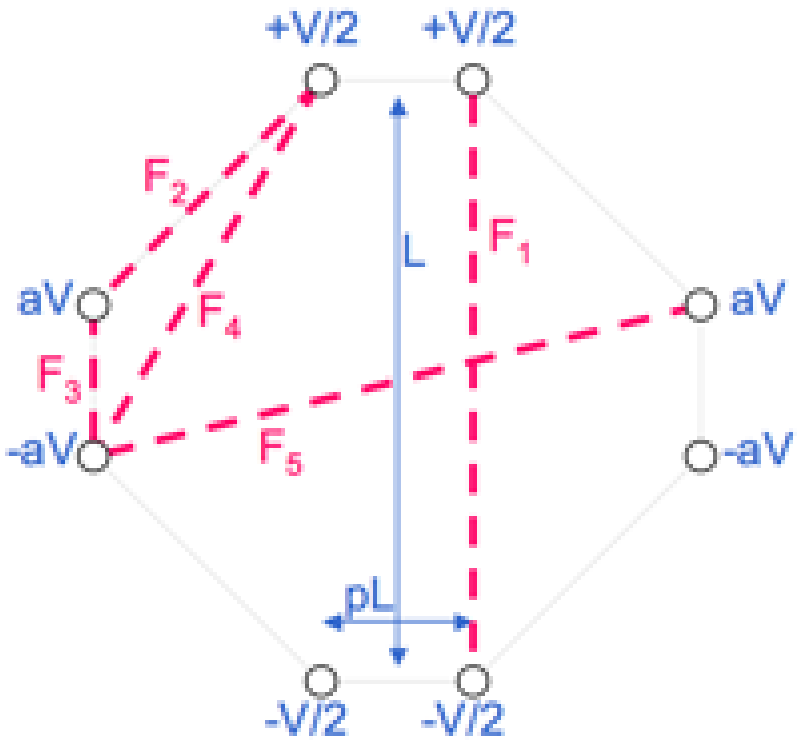

Figure 3.11: Schematic diagram for dielectrophoretic force constants for various interconnects in a 2×2 crossbar geometry. Circles indicate electrode tips.

$$\frac{F_5}{F_1} = \frac{(2a)^2}{\left[\sqrt{p^2+1}\right]^3}.$$

In order to estimate the proper conditions for trapping of non-circumferential interconnects, particularly the interconnect at F_1, we are most interested in the parameters $0 < a < 1/2, 0 < p < 1$ that cause all of these ratios to fall below 1. We survey this phase space in Figure 3.12, and find that – at least by this prediction method – long crossbar-style interconnects should be possible as long as the parallel electrode pitch is 10-20 times smaller than the interconnect length ($0.05 < p < 0.1$) and electrodes uninvolved in the trapping are kept grounded ($a = 0$).

3.4.4 Field-programmable gates

In addition to interconnect architectures, it should also be possible to more directly build logic based on dielectrophoretic reconfiguration of nanodevices. In particular, with the proper arrangement of pairs of the latching electrodes shown in Figure 3.7, digital logic gates can be reproduced. In these gates, as depicted in Figure 3.13, the relative phase of two electrodes determines the position of interconnects which can then carry or block a current path specific to the logical operation required.

3.4.5 Packaging

In order to enable the vision of dielectrophoretic architectures for self-repairing computer components, development of stable colloidal reservoirs of components will be crucial. Fortunately, many dielectric solvents, such as the benzyl alcohol used in the reconfigurable nanowire work discussed above, have low vapor pressures. This property may enable colloidal reservoirs of replacement components to be stably

sealed into a chip carrier package, as shown in Figure 3.14. In preliminary tests, sealed reservoirs of benzyl alcohol for dielectrophoretic manipulation remained stable, in the sense that nanowires remained suspended and there was no visible leakage of solvent, for more than a week under refrigeration.

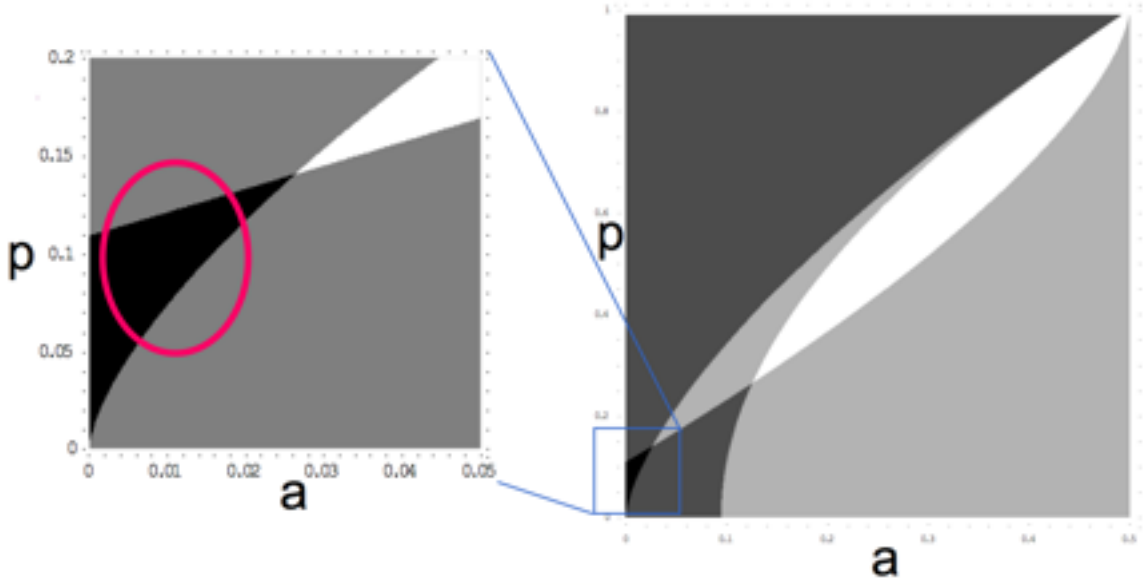

Figure 3.12: Phase diagram of dielectrophoretic forces $(F_2, F_3, F_4, F_5)/F_1$ in the space of dimensionless electrode voltages (a) versus electrode spacings (p) in a 2×2 crossbar geometry. Darker regions indicate that more of F_2, F_3, F_4, F_5 are less than F_1.

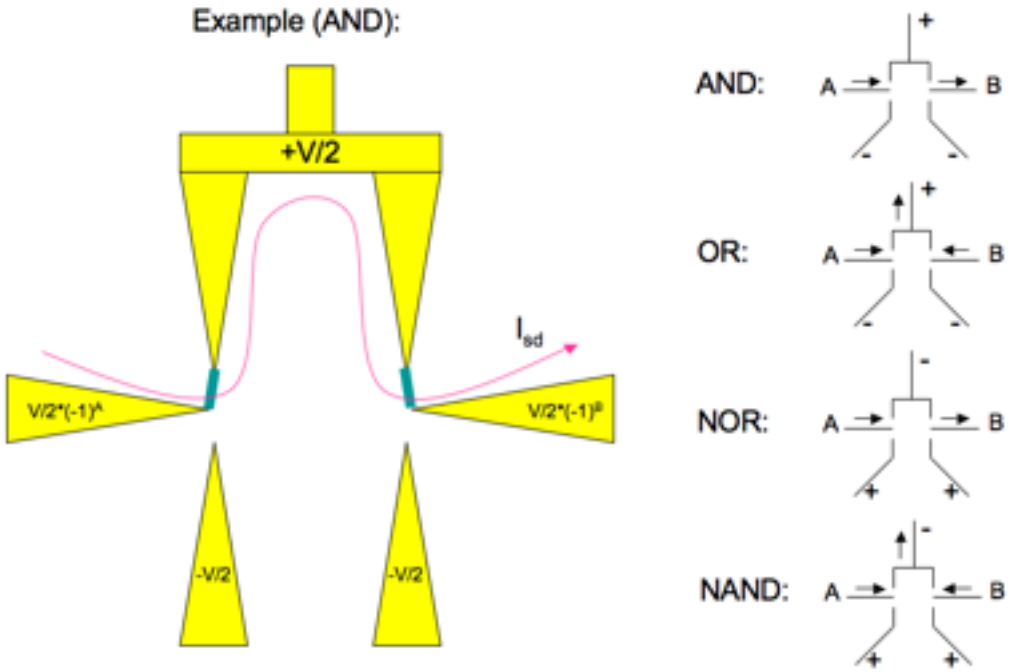

Figure 3.13: Field programmable gates in which short voltage pulses on two electrodes serve as input (phase indicated by sign), and current indicated by arrows serves as output.

Figure 3.14: Packaged nanowire reservoir.

Chapter 4

Thermal Programmability

4.1 Introduction

Recent advances in the synthesis of large-area diamond and diamond-like carbon films are opening up new applications for wear-resistant prosthetics [57-59], artificial heart valves [60], and joint replacements [61, 62]. While the wear resistance of diamond is dramatically superior to titanium and stainless steel, its blood clotting response as measured by fibrinogen adhesion is slightly worse than these materials [63]. Moreover, the possibility has been raised that nanostructured surface features of diamond might abrade tissue [64]. In the present work, we show for the first time that chemically modified diamond (111) films can stabilize remarkably long-ranged orderings of ice up to human body temperatures and at ambient pressure. The soft and hydrophilic ice multilayers sustained by this unique physical effect might enable diamond-coated medical devices that reduce abrasion and are highly resistant to protein absorption [64].

Low-temperature and short-range interfacial ordering of water has been previously predicted and observed on a variety of other planar substrates, including muscovite mica [65-67], platinum [68], chlorine-terminated silicon [69], quartz [70, 71], and graphite [72]. Ordering on these substrates has been attributed to electrofreezing [72], lattice matching to partially charged surface atoms [65-67, 69, 71], polar binding of the first monolayer [68], confinement effects [70], and combined electrofreezing and confinement [73]. Of these mechanisms, only lattice matching to surface ions (in particular, exposed K^+ ions on muscovite mica) has been demonstrated to passively sustain ordering on an open surface at room temperature [66]. Yet, even the ice phase on mica is not stable when thicker than a single bilayer. Molecular dynamics simulations [74] show a first-order freezing transition for water films of bilayer thickness in nanopores, but for five or six layers there is no transition. Specular x-ray reflection studies of mica (001)-water interfaces [75] reveal a density oscillation amplitude significantly reduced beyond 3 Å, while recent Monte Carlo simulations [76] suggest that an ice Ih layer may not even exist at this interface.

In order to stabilize ice coatings with the nanometer-scale thicknesses relevant to macromolecular adsorption, at temperatures relevant to *in vivo* applications, a novel substrate is therefore needed. In particular, for a stronger ordering effect without external fields and at ambient conditions, a more stable surface chemistry than silicate-intercalated ions is required: in the case of mica, at least half of the surface K^+ counterions may be removed by rinsing and replaced with H_3O^+ [75, 76]. The counterions are displaced at two distinct distances from the surface and none remains on the surface, suggesting that the relatively weak solvation efficiency of K^+ ions (as

compared to Li^+ ions, for example) is responsible for the stronger pinning of water molecules on the surface [76].

A substrate that solves this surface stability problem, the (111) diamond surface partially terminated by alkali ions, was proposed recently [77]. Diamond is an interesting candidate for achieving extreme hydrophilic behavior on a substrate suitable for biomedical applications. It can be grown over large areas in polycrystalline form [78] and exhibits high corrosion resistance, making it attractive as a surface finish for biomedical devices and implants [79]. Moreover, its submonolayer surface structure has the added advantage of minimal lattice mismatch with ice Ih (less than 2%), reducing any strain effects that could be detrimental to the stability of ice layers. Motivated by these considerations, we study here the stabilizing effect of the chemically modified diamond (111) surface on the melting transition of interfacial ice. We specifically consider the synthetically accessible [77] diamond surface in which 1/3 of the H atoms in the original termination (denoted by C(111)-H in the following) are replaced by Na atoms (denoted by C(111)-Na).

4.2 Simulation Details

4.2.1 Initial Configuration

Direct simulations of the freezing phase transition are challenging [80], so we focus instead on understanding the stability of initially crystalline ice layers. We chose to use the TIP4P/Ice water model [81], in order to reproduce the melting temperature of ice at 1 atm and the stability of the Ih phase. (The recently released TIP4P/2005

model [82] correctly reproduces the phases of ice over a broad temperature and pressure range, but at systematically depressed temperatures.) We begin with a configuration in which eight bilayers [83] of ice Ih are aligned epitaxially with the Na atoms, which are covalently bonded to the C(111) surface, as shown in Figure 4.2(a). The ice is initially completely polarized parallel to the C-Na dipoles. The initial Na-O distance is 2.38 Å, as calculated previously [77].

4.2.2 Thermostat Preparation

A major consideration when attempting to simulate two thermally interacting materials is their differing energy densities. This effect becomes more pronounced when one of the materials is near a phase transition. An initial perturbation away from the ground state of the higher energy density material can release enough energy, as that material relaxes, to vaporize the lower energy-density material through thermal conduction. In fact, an even more spectacular and unphysical effect can take place if there is a global thermostat in place. As the perturbation relaxes and kinetic energy is released, energy is then withdrawn from other degrees of freedom. This artificial cooling effect can be so dramatic that the epitaxy between the two solids shifts in phase as the surface atoms of one solid come to rest in the troughs between the surface atoms of the other. On a longer time scale, heat then propagates through the hard solid and then to the soft solid, again vaporizing it. The solution to this problem is to place independent thermostats on both the soft and hard solids to prevent heat transfer. However, only a single thermostat should be placed on the soft solid because more than one will prevent heat transfer to latent heat or heat of fusion

between components.

4.2.3 Barostat Preparation

A second unique consideration for our simulations is that of pressure. The commonly-used Andersen method [84] for implementing a barostat in molecular dynamics simulations entails adding the universe volume as a degree of freedom, and consequently can introduce unphysical volume "ringing" during a system's equilibration.An example of this pitfall is shown in Figure 4.1. The ringing and its effects were minimized by moving the system's center of mass to the center of the universe and by only measuring displacements of molecules in the melting solid relative to their surrounding molecules rather than in absolute terms. Moreover we selected a relatively short, 100-fs relaxation time for the barostat [85] to further minimize the ringing effects.

An Anderson barostat [84, 85] with a 100-fs relaxation time was used and two independent thermostats were maintained for the diamond and the ice multilayer to prevent unphysical heat transfer.

4.2.4 Force Field Details

The interaction between atoms is represented by a Lennard-Jones (LJ) potential and a Coulomb potential with a 14.69-Å cutoff, using LJ parameters for surface H adapted from [86], surface Na from [87], and diamond C from [88]. The LJ potential for an atom pair, X-Y, was approximated by averaging the diatomic potentials for X-X and Y-Y. For the diatomic potential form, $U_{\text{X-X}}(r) = 4\epsilon_{\text{X}}[(\sigma_{\text{X}}/r)^{12} - (\sigma_{\text{X}}/r)^{6}]$ the parameters used to model the surface were $\epsilon_{\text{H}} = 0.0157$ kcal/mol, $\sigma_{\text{H}} = 1.3248$ Å,

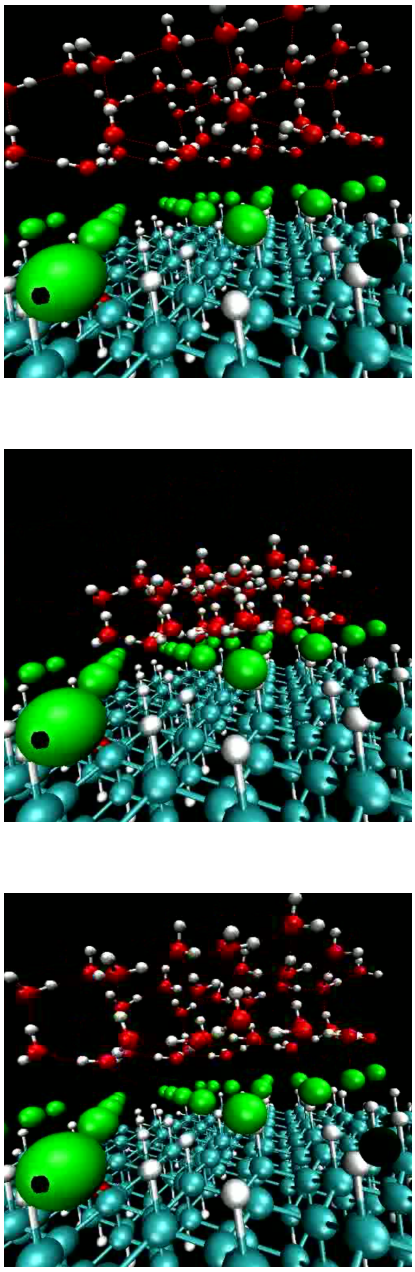

Figure 4.1: Volume oscillation (top to bottom) resulting from barostat equilibration.

$\epsilon_{\mathrm{C}} = 0.1094$ kcal/mol, $\sigma_{\mathrm{C}} = 1.6998$ Å, $\epsilon_{\mathrm{Na}} = 0.00277$ kcal/mol, $\sigma_{\mathrm{Na}} = 1.6642$ Å. The bond lengths for C-Na (2.5 Å) are adapted from [77], and for C-C (1.5 Å) and C-H (1.09 Å) from [89]. The C(111) surface is represented by a 33.94 Å $\times$ 29.39 Å periodic supercell in the lateral dimensions and two bilayers in the (111) direction, capped by H atoms on the far side from the ice. The H and Na atoms have partial charges of $+0.1e$ and $+0.4e$, respectively, as determined from *ab initio* quantum mechanical calculations [77], which are neutralized by the directly bonded C atoms.

4.2.5 Melting Criterion

We turn next to the method of determining melting of the ice layers. In two-dimensional melting, mean square displacements diverge [90] and are not a good criterion to distinguish between liquid and solid states [91]. Instead, we adapted a shell-relative-displacement criterion [92] to intra-bilayer neighbor shells: we define the local displacement

$$\mathbf{u}_i(t) = \frac{1}{a}\left(\mathbf{r}_i(t) - \frac{1}{3}\sum_{j\in \mathrm{NN}} \mathbf{r}_j(t)\right), \tag{4.1}$$

where $\mathbf{r}_i$ is the position of a water O atom i, the sum is taken over the positions of the 3 initial nearest-neighbor O atoms within the bilayer of that atom, and $a = 2.75$ Å is the measured O-O separation in ice Ih [83]. The atomic Lindemann parameter is defined as the deviation

$$s_i(t) = \left[\frac{1}{t+1}\sum_{l=0}^{t} \mathbf{u}_i^2(l) - \left(\frac{1}{t+1}\sum_{l=0}^{t} \mathbf{u}_i(l)\right)^2\right]^{1/2}, \tag{4.2}$$

where the sums are taken over all previous time steps. The Lindemann parameter for bilayer n is then naturally defined as $\delta_n(t) = \langle s_i(t)\rangle$, where the average is over

all O atoms in the bilayer. The displacements and Lindemann parameters defined above are independent of bilayer shear. This feature proved essential since, at 240 K, bilayer 1 was observed to relax laterally from its initial epitaxial alignment such that, after 1 ps, the bottom-most O atoms close-packed between Na atoms. However, at 310 K, bilayer 1 remained approximately epitaxial to the Na submonolayer, as shown in Figure 4.2(b).

A dynamic criterion for determining if a bilayer has melted at a given temperature can be defined in terms of the dynamic Lindemann parameter $\delta_n(t)$. When bilayers melt, the motion of each water molecule becomes uncorrelated with the motion of its initial nearest neighbors, allowing the displacement $\mathbf{u}_i$ to diffuse freely, and causing $\delta_n(t)$ to grow linearly with time [91]. In contrast, for layers that have not yet melted, $\delta_n(t)$ saturates asymptotically to a constant value [91]. For sufficiently long simulation times τ, this melting transition manifests as a first-order discontinuity in $\delta_n(\tau)$ versus $\delta_n(\tau) - \delta_n(\tau/2)$, since $\delta_n(\tau) - \delta_n(\tau/2)$ approaches zero asymptotically as a function of τ below the melting point. The critical $\delta_n(\tau)$ value separating the linearly growing versus constant values is then used as the effective Lindemann criterion δ_L [91].

4.2.6 Visual Representation

Finally, we found that a useful static visual representation for rapidly assessing the melting state of solid layers was the image average over long melt trajectories. For example, we were able to compare ice in three different environments at 310 K using this method, as shown in Figure 4.3. Melted molecules, with a higher Lindemann value, appear blurred whereas unmelted molecules appear sharply defined. Surface

melting became visible on both faces of free ice (Fig. 4.3*A*) and the single free face of ice on C(111)-H (Fig. 4.3*B*). A hard-wall effect [75] is visible for the C(111)-H environment as a flattening of the interfacial bilayers, as expected. In contrast, melting was only visible in the 2 bilayers farthest from a C(111)-Na surface (Fig. 4.3*C*). Additionally, partial melting was visible at the lateral faces of the supercell for ice in the free and C(111)-H environments, but not in the C(111)-Na environment.

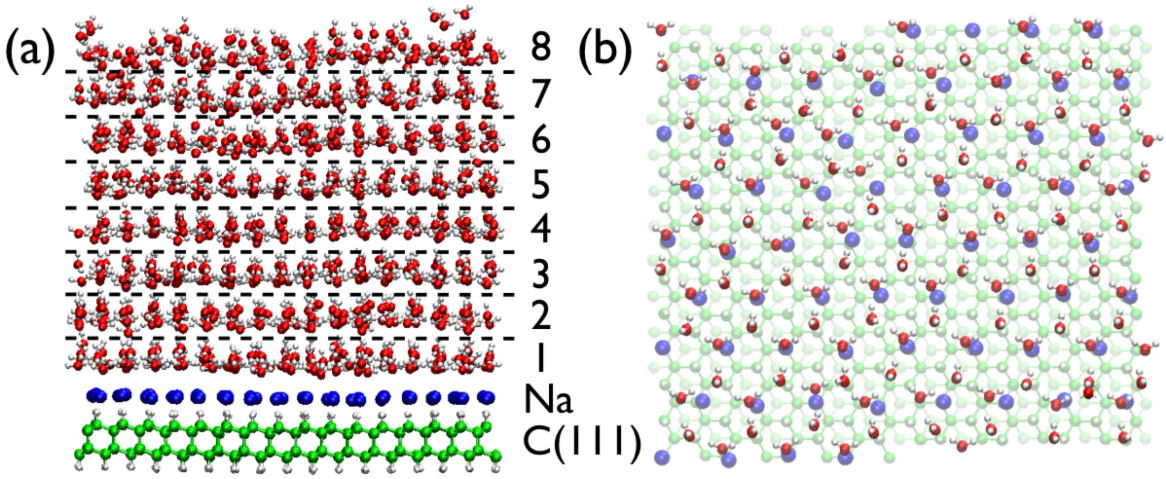

Figure 4.2: Visualization of epitaxial ice bilayers on the modified diamond surface. (a) Side view, showing the slab representing the C(111)-Na substrate at the bottom and the eight initially-distinct bilayers of ice separated by dashed lines in an instantaneous configuration after 5 ps at 310 K. The distance between dashed lines is 3.7 Å. (b) Top view of bilayer 1 with C(111)-Na surface in background.

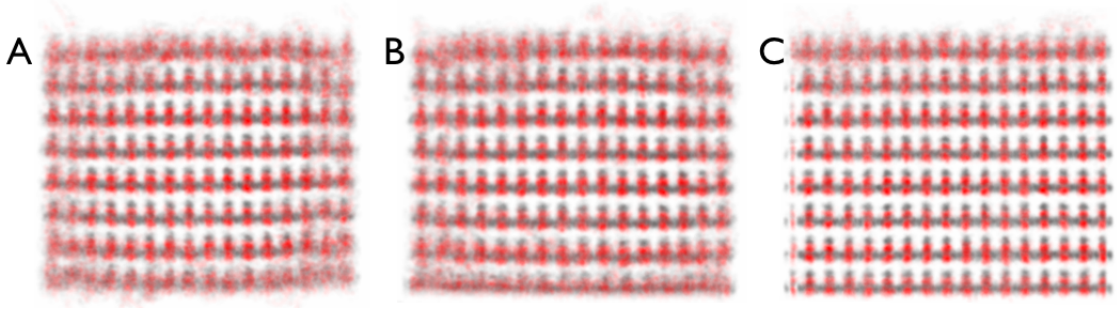

Figure 4.3: Mean molecular field of ice bilayers at 310 K in different environments. The environments considered are (*A*) free ice, (*B*) ice on C(111)-H, and (*C*) ice on C(111)-Na.

4.3 Results and Discussion

4.3.1 Evolution of Lindemann Parameters

With these definitions, we can extract a value for δ_L from the molecular dynamics simulations. By examining collectively the evolutions over time $\tau = 5$ ps of all ice bilayers under a range (240-340 K) of ice thermostat values, we find $\delta_L = 0.161 \pm 0.009$ (corresponding to a 0.44 Å r.m.s. shell displacement), as shown in Figure 4.4. This value agrees well with the threshold of 0.167 predicted by the cooperative motion model of 2D melting, in which layers slide past each other [92, 93]. As additional confirmation, Lindemann parameters that rose above δ_L tended to continue to increase monotonically, while those below saturated. Finally, the ice vapor pressure was found to be nonzero when the Lindemann parameters of the top-most layers rose above δ_L, as seen by the molecules about to be released from layer 8 in Figure 4.2(a).

4.3.2 Calculation of Bilayer Melting Temperature

To solve for the melting point of each bilayer, δ_L must be equated to the Lindemann parameter, as a function of temperature, for that bilayer. Since $\delta_n(t)$ for a melted bilayer does not saturate with time, the Lindemann function was calculated after the finite time $\tau = 5$ ps. Cubic spline interpolation, with quadratic extrapolation for boundary temperatures, was then applied to each Lindemann function to solve for its unique melting point. The final parameters $\delta_n(\tau)$ are shown in Figure 4.5 over the temperature range 210-350 K, for all ice bilayers in three different environments: free ice, ice on C(111)-H, and ice on C(111)-Na. For $\delta(\tau) < \delta_L$, the functions $\delta(\tau)$ of

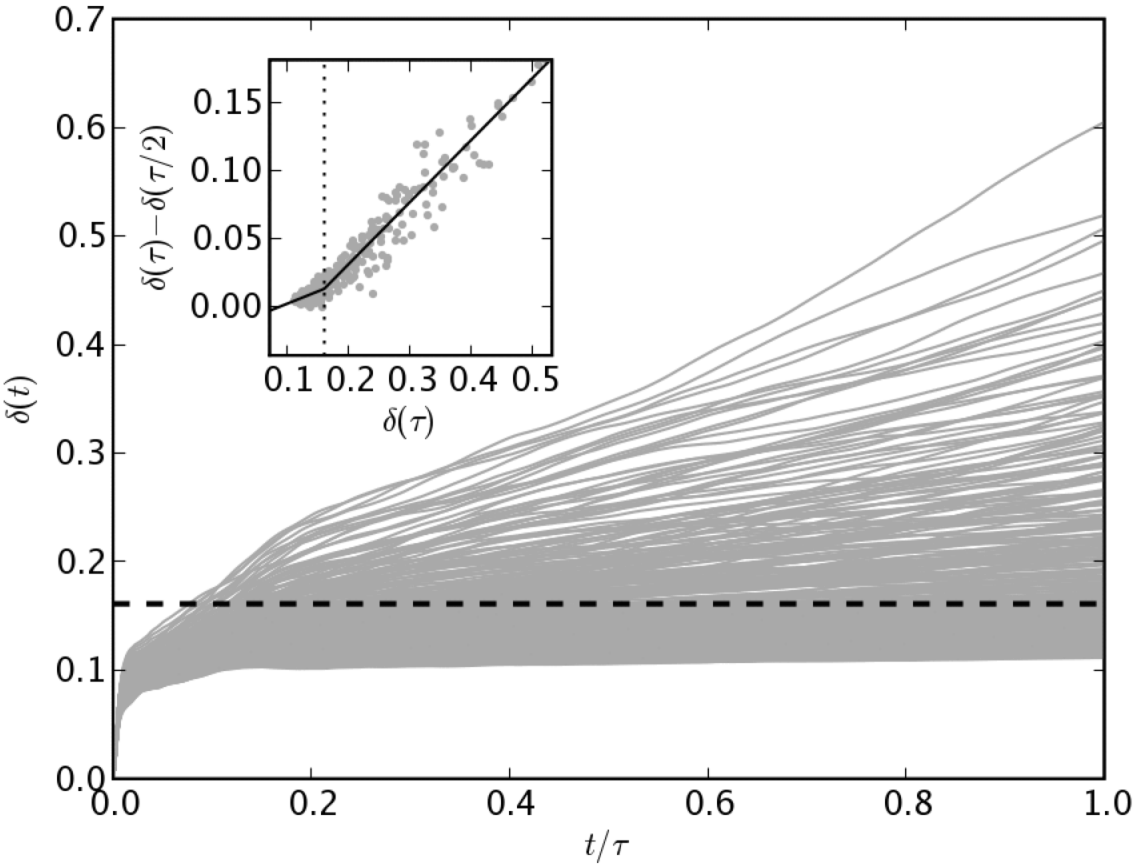

Figure 4.4: Calculation of the bilayer melting threshold. Main figure: Time evolution of Lindemann parameters $\delta_n(t)$ for all ice bilayers over a range of temperatures. Inset: Extraction of δ_L from a piecewise linear fit of $\delta_n(\tau)$ versus $\delta_n(\tau) - \delta_n(\tau/2)$. The fitted value of δ_L is indicated with dashed lines.

temperature T scale roughly with $T^{1/2}$, which is expected for diffusion in a harmonic potential. For $\delta(\tau) > \delta_L$, the functions scale linearly or superlinearly with temperature, which is suggestive of ballistic motion and energy transfer to melted molecules in those bilayers.

The calculated melting temperatures for bilayers in each environment are shown in Figure 4.6(a-c). The primary source of error in each melting curve is the uncertainty in δ_L. We discuss first the melting curves in free ice and ice on C(111)-H, which are our reference systems, the first being devoid of any substrate effects, the second being a hydrophobic surface [94]. The melting curves for both environments show an approximate symmetry, with bilayers 1 and 8 melting at temperatures much lower (by 70-115 K) than the melting temperature of the middle bilayers. The difference in melting temperature between layers 1 and 8 of 20-45 K is attributable to the polarization of the ice film, which exposes asymmetric ice surface structures. The close correspondence between the behavior of free ice and ice on C(111)-H is consistent with the latter exhibiting hydrophobic behavior.

In sharp contrast to these two control environments, ice on C(111)-Na shows an increase of the melting temperature by 130 K for bilayer 1 relative to free ice. Moreover, the increase in melting temperature persists through the entire ice film, as shown in Figure 4.6(d), such that six bilayers (2.2 nm thick) are predicted to remain frozen at 310 K (human body temperature) and seven bilayers (2.6 nm thick) remain frozen at 298 K (room temperature). The average melting temperature of free ice is 265 ± 37 K, in agreement with the established 1-atm value, and ice on C(111)-H has only a moderately elevated average melting temperature of 275 ± 34 K. In contrast,

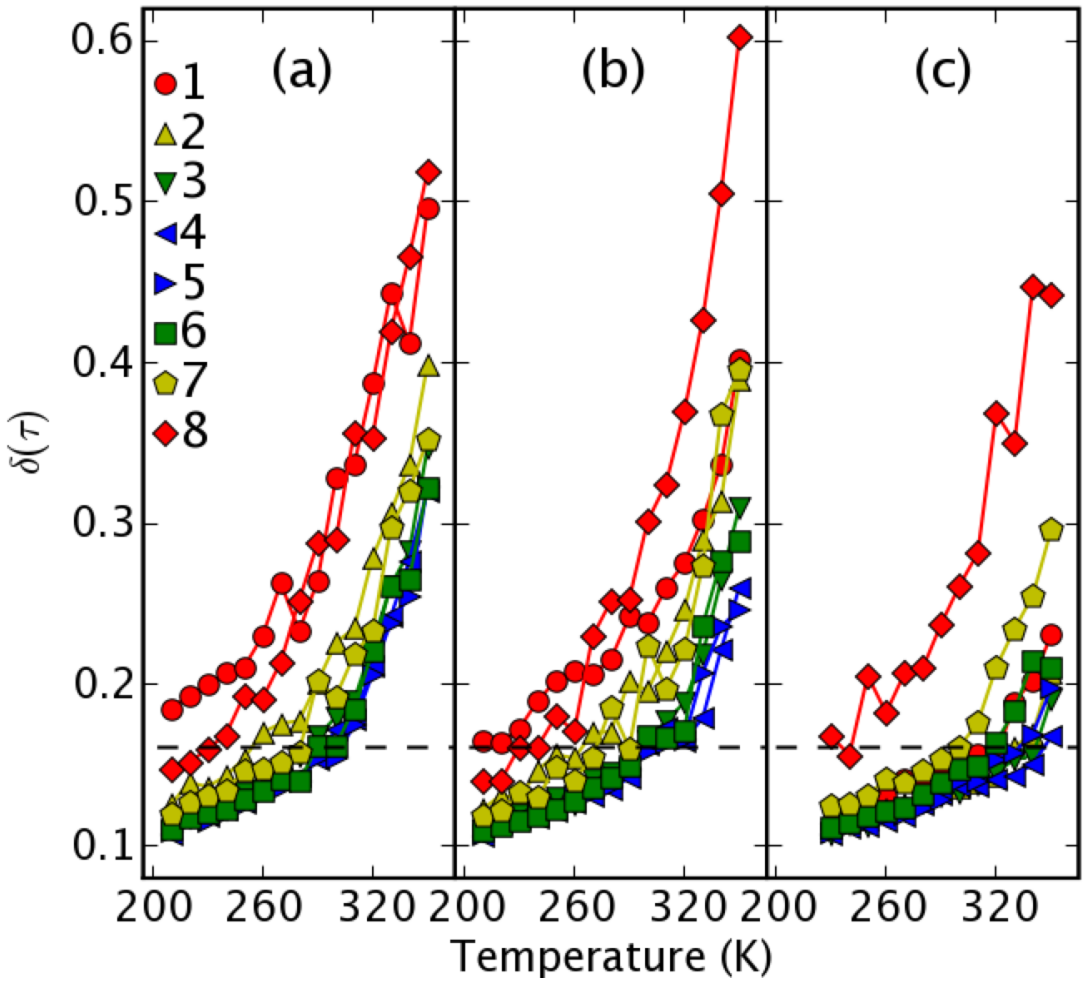

Figure 4.5: Temperature dependence of Lindemann parameters for ice bilayers in different environments. The environments considered are (a) free ice, (b) ice on C(111)-H, and (c) ice on C(111)-Na. The melting threshold, δ_L, is indicated with dashed lines.

ice on C(111)-Na has an average melting temperature of 314 ± 30 K.

4.3.3 A Phenomenological Model

We next develop a phenomenological model to explain the observed temperature elevation, by considering separately the electrostatic stabilization of bilayer 1 and the stabilization of each subsequent bilayer by the previous bilayer. Assume that each molecule in bilayer n experiences a planar potential well $V_n(\mathbf{r}, z) = A_n \mathbf{r}^2 \delta(z - z_n)$ centered at its equilibrium position in the ice phase. The Boltzmann position distribution is then given by

$$P_n(\mathbf{r}) = \frac{A_n}{\pi k_B T} \exp\left(-\frac{A_n \mathbf{r}^2}{k_B T}\right). \tag{4.3}$$

Furthermore, if the planar potentials in bilayer $n > 1$ are centered at the projected molecular positions in bilayer $n-1$, the individual thermal distributions are convolved, $P'_n(\mathbf{r}) = P_1(\mathbf{r}) * P_2(\mathbf{r}) * \ldots * P_n(\mathbf{r}) \propto \exp\left(-B_n \mathbf{r}^2 / k_B T\right)$, with $B_n \equiv (\sum_{i=1}^{n} A_i^{-1})^{-1}$. Since the dipole-dipole interaction strength drops off as z^{-3}, we can neglect surface field effects for $n > 1$ and assume that $A_2 = A_3 = \ldots = A_n$. Therefore, molecules in bilayer n experience an additional effective potential from the diamond surface,

$$V'_n(\mathbf{r}, z) = \left(A_1^{-1} + (n-1)A_2^{-1}\right)^{-1} \mathbf{r}^2 \delta(z - z_n). \tag{4.4}$$

For a thermalized molecule in this effective potential, $\langle \mathbf{r}_n^2 \rangle = \left(A_1^{-1} + (n-1)A_2^{-1}\right) k_B T$, and therefore the melting temperature at the Lindemann threshold $\langle \mathbf{r}_n^2 \rangle \sim \delta_L^2 a^2$ is given by $T_n = \left(A_1^{-1} + (n-1)A_2^{-1}\right)^{-1} \delta_L^2 a^2 / k_B$. The observed temperature elevation is reproduced well with $A_1 = 0.94$ J/m^2 and $A_2 = 1.18$ J/m^2, as shown in Figure 4.6(d). To justify the value of A_1, we consider the strength of the potential in the equilibrium

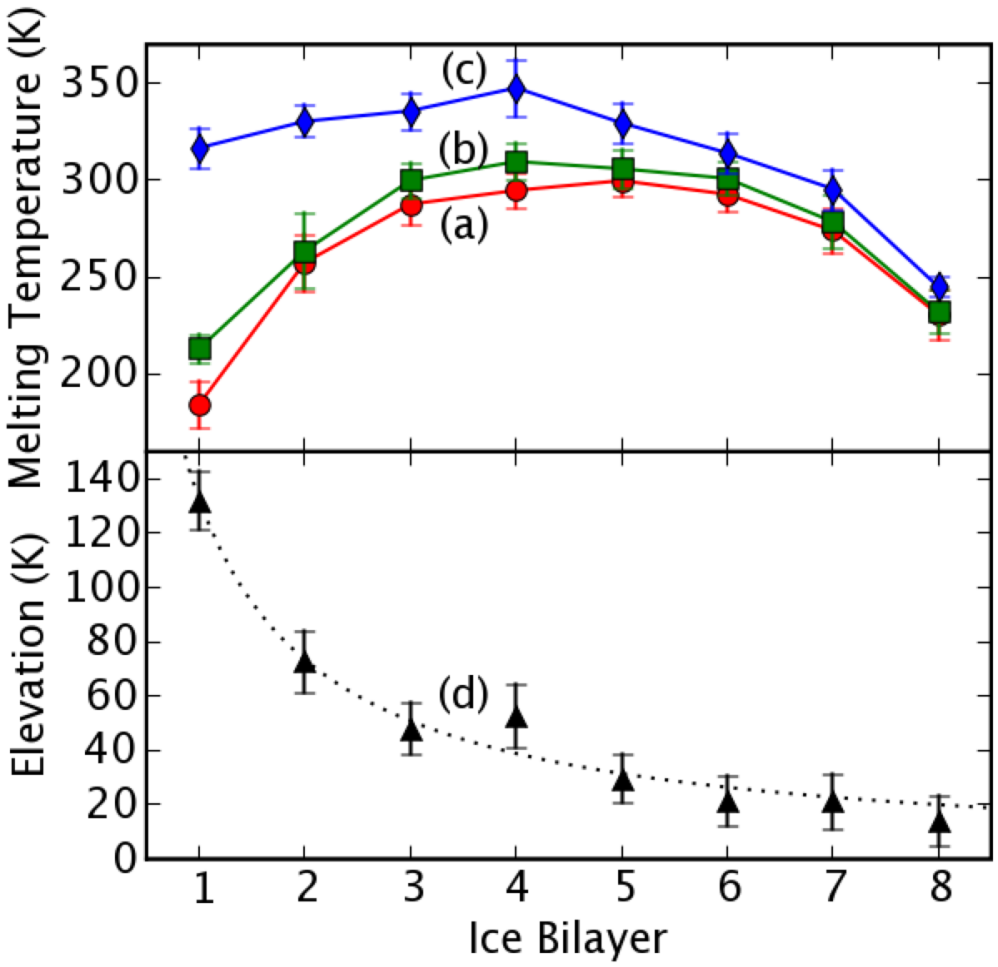

Figure 4.6: Calculated melting points for ice bilayers in different environments. Melting temperatures are shown for each bilayer in (a) free ice, (b) ice on C(111)-H, and (c) ice on C(111)-Na. (d) The melting point elevation of bilayers in ice on C(111)-Na relative to free ice, with the phenomenological fit shown as dotted line.

plane of a bilayer-1 water molecule epitaxial to the diamond surface, due to near-field dipole-dipole interaction with ions on the modified diamond surface. For surface charges $q = 0.4e$ with separation $d = 2.5$ Å, a nearly epitaxial water molecule with dipole moment p parallel to the surface dipole experiences an in-plane quadratic potential $V_1(\mathbf{r}, z) = A_1' \mathbf{r}^2 \delta(z - z_1)$ with strength

$$A_1' = \frac{3pq}{8\pi\epsilon_0} \left(\frac{1}{(z - d/2)^4} - \frac{1}{(z + d/2)^4} \right). \tag{4.5}$$

For sub-melting displacements at a distance z away from the surface, with $z_1 \leq z \leq z_1 + \delta_L$, we obtain $A_1' = 1.04 \pm 0.26$ J/m^2, in excellent agreement with the value obtained from the fit of Eq.(4.3.3). This suggests that the electrostatic interaction of molecules in bilayer 1 with the neighboring Na^+ sites dominates the observed melting temperature elevation for that bilayer.

4.4 Conclusion

In summary, we have shown through simulation that chemically modified diamond may stabilize, at elevated temperatures, ice multilayers substantially thicker than experimentally observed on other surfaces. This work opens up the possibility of protective ice finishes for *in vivo* diamond applications without cryogenics.

Such unique thermal characteristics might also be useful for solar energy applications. In particular, the diamond-ice phase might be able to compensate for variability in the insolation supply by locally buffering the thermal output of solar collectors using hot water sequestered on such diamond surfaces. This water-based approach to small-scale solar energy storage and buffering would have the potential advantage

of being more environmentally friendly than lithium-ion batteries or organic phase-change materials. The results reported in this chapter suggest that the stabilized solid-liquid transition of water can be elevated close to its liquid-vapor transition, allowing above 50% more latent heat to be stored near the melting point than with a heat exchanger based on the normal solid-liquid transition. When there is a supply surplus, steam could be passed over the H-terminated face of diamond, transferring heat to the opposite Na-modified face where the stabilized ice phase is melted and acts as a buffer. When there is a supply deficit, hot liquid water could be run over the H-terminated face to draw energy back from the buffer and be vaporized. Diamond is an ideal material for this heat exchange process because of its high thermal conductivity, and might be economically scaled up to deal with larger volumes of water using pebble beds.

Chapter 5

Hydrodynamic Programmability

5.1 Introduction

Recently, there has been significant interest in nanoscale tubes, channels, and pores because of their potential for improved chemical separations [95-98], applicability to the analysis and fundamental study of DNA and other nucleic acids [99-103], and usefulness for observing the physics of nanoconfined fluids [104, 105]. Whereas carbon nanotubes [106] and other fullerene-like structures [107-111] have been studied extensively, the templated growth of tubes composed of oxides [95, 112-114], gallium nitride [115, 116] and undoped silicon [117-119] has received attention more recently. However, a synthetic route toward single-crystal semiconductor nanotubes with controllable size, geometry, and electrical properties has not been demonstrated to date. Such materials would have important applications for the development of integrated fluid transport and sensing devices [120-123] with ionic fluid conductance tuned through local electrostatic gating [124-127] or chemical surface modification

[128]. Previous methods for preparing nanotubes include deposition in the openings of nanoporous membranes [112, 129]. After selective etching of the membrane, only the tubes remain. However, this approach limits the structural diversity of tubes to that of the shape and geometry of available membranes. A more robust method utilized recently is to grow a nanowire template, the size and shape of which is more readily controlled. The tubes, deposited as shells on the template by chemical vapor deposition (CVD), remain after the etching of the template cores [113, 116, 119].

5.2 Experimental Details

5.2.1 Hollow Nanostructure Synthesis

The growth of silicon shells on germanium cores is an ideal route toward nanotubes because of the control achievable over the core size and geometry [130, 131], ease with which epitaxy can be controlled [132, 133], and ability to etch Ge while leaving Si intact. For our experiments, Ge wire templates were grown and conformal Si shells deposited epitaxially using established methods.

Crystalline Ge cores were grown by using Au nanocluster catalysts, 2.3% GeH_4 in a carrier gas of ultrapure H_2 at 450 torr and 315°C. Tapered Ge wires for conical shells were grown using 5 nm Au nanocluster catalysts, with 10% GeH_4 reactant in H_2 carrier at 380°C and 80 torr. Growth occurred at a radial rate of ∼10 nm/min and axial rate of ~ 1 μm/min. Intrinsic Si shells were grown using SiH_4 reactant at 5 torr and 450°C, yielding a radial growth rate of ∼0.5 nm/min. P-type Si shells (1500:1) were grown using SiH_4 reactant (28%) and B_2H_6 (0.072%) dopant in ultrapure H_2 at

450°C for 1 min while ramping pressure from 0 to ∼20 torr. The core-shell structures were annealed at 600°C (intrinsic) or 800°C (p-type) under vacuum for 2 hours to achieve single-crystal shells.

The heterostructures were removed from the growth substrate and suspended in a 30% H_2O_2:H_2O solution by ultrasonication. The solution was heated to 90°C for ∼1 hour to etch the Ge cores and then repeatedly centrifuged at 14 krpm (10 min) and diluted with ethanol to replace the HO.

5.2.2 Electrical Characterization

For electrical characterization, devices were fabricated on a degenerately doped Si wafer, which served a the gate electrode, with a 50 nm oxide layer as the gate dielectric. Ni electrical contacts (65 nm) were defined by electron beam lithography and deposited by thermal evaporation of the metal, then annealed at 350°C for 60 seconds.

5.2.3 Fluidic Transport

For fluidic transport experiments, the substrates used were glass cover slips (Corning) upon which gold electrodes had previously been fabricated. First, Ge/Si heterostructures wires were deposited, then SU8-25 (MicroChem Corp., Newton, MA) was spin coated (3000 rpm, 30 sec) for barrier fabrication. The barriers were defined using photolithography; the wall separating the two chambers was 10 μm wide. After development, the entire chip was hardbaked (180°C for 30 min) to increase crosslinking of the polymer. Finally, the chips were submerged in 30% H_2O_2:H_2O for ca. 12

hours at room temperature. Environmental Scanning Electron Microscopy (ESEM) with Energy Dispersive X-ray Spectroscopy (EDS) detection was used to confirm that the germanium had been completely etched away. The etched chip was mounted on an inverted lens confocal microscope with epifluorescence capabilities. Oregon Green dye was excited using the 488-nm line of an argon ion laser and fluorescence was observed through a 500-550-nm band pass filter.

5.3 Results and Discussion

5.3.1 Structural Characterization

This process selectively etched the germanium core while leaving the crystalline silicon tube intact (Figure 1A). Transmission electron microscopy (TEM) images of the wires and tubes confirm that the growth is epitaxial (Figure 1B) and that the etch process causes minimal oxidation of the surface of the shells (Figure 1C). A Fourier transform of the image (Figure 1C, inset) indicates that the growth direction of the template is along the <112> axis. Our scheme of rational control allows us to produce a sample containing tubes of uniform geometry (Figure 1D). Few catalyst particles were observed; a typical sample consisted mainly of tubes open at both ends (Figure 1D, inset).

5.3.2 Electrical Characterization

Electrical transport measurements demonstrate that single-crystal boron-doped silicon nanotubes can be used as p-channel field effect transistors (FETs). Such

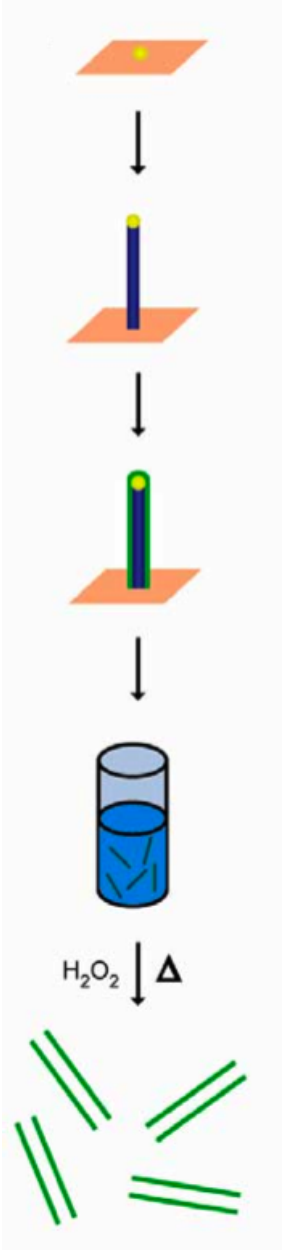

Figure 5.1: Nanotubes are produced by growing germanium nanowires (blue), then coating with silicon (green). The wires are removed from the substrate by sonication, and then the germanium is etched in a heated hydrogen peroxide solution.

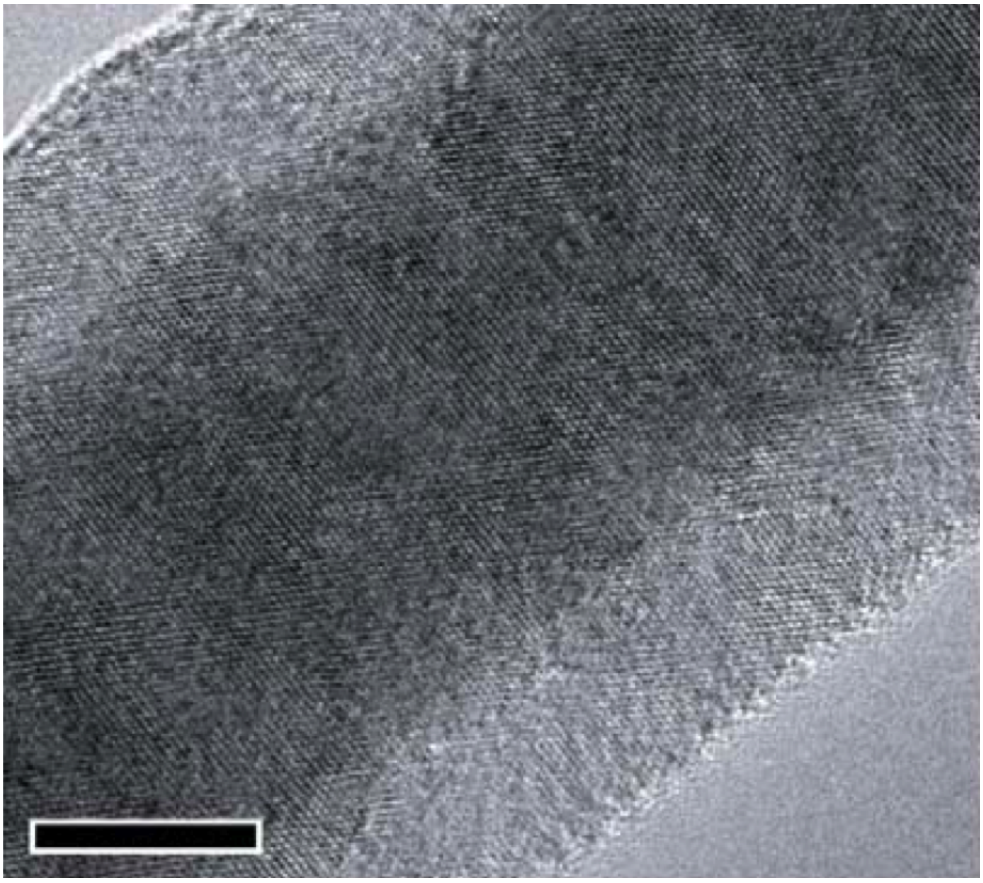

Figure 5.2: High resolution TEM image shows that an intrinsic silicon shell grows evenly and epitaxially on a germanium core.

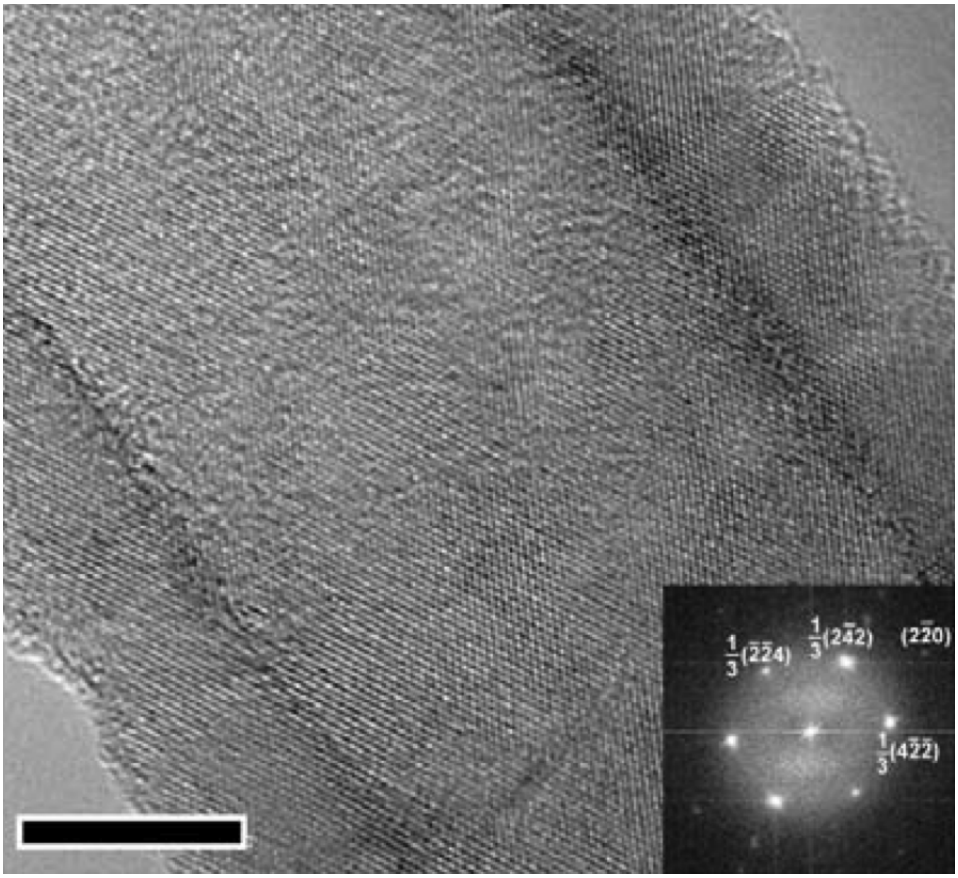

Figure 5.3: After etching, only the crystalline Si shell remains. Scale bars are 10 nm. Inset, Two-dimensional Fourier transform of the image.

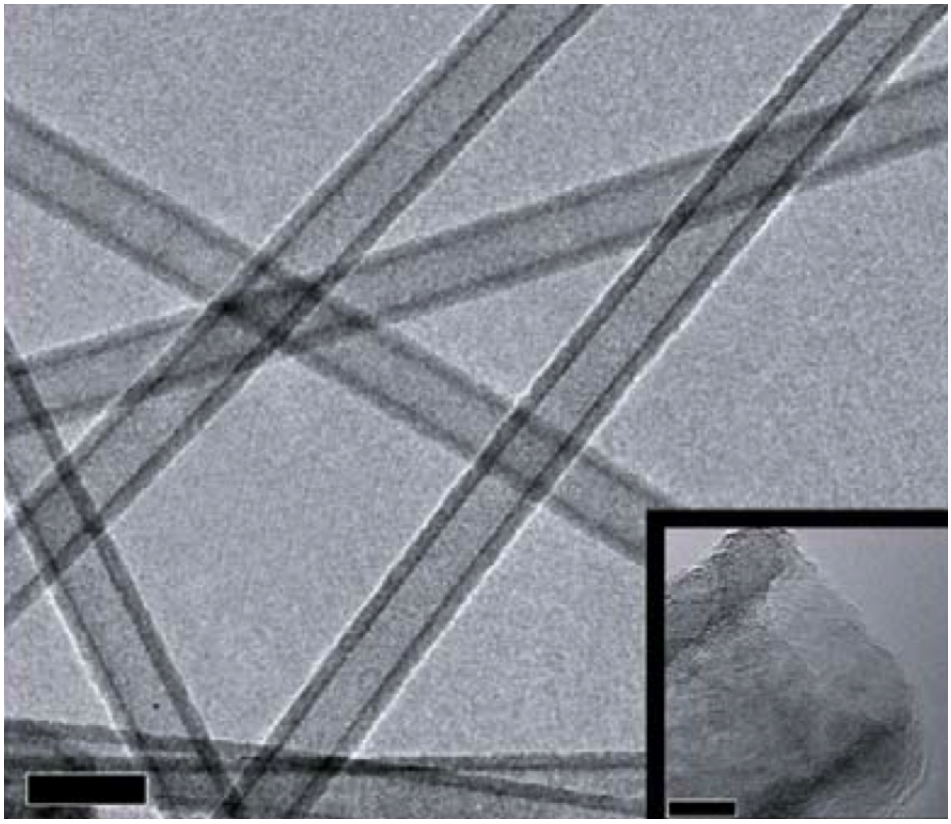

Figure 5.4: Low resolution picture of several nanotubes demonstrates uniformity. Scale bar is 50 nm. Inset, The end of a typical nanotube clearly exhibits a hollow center and stable walls. Scale bar is 5 nm.

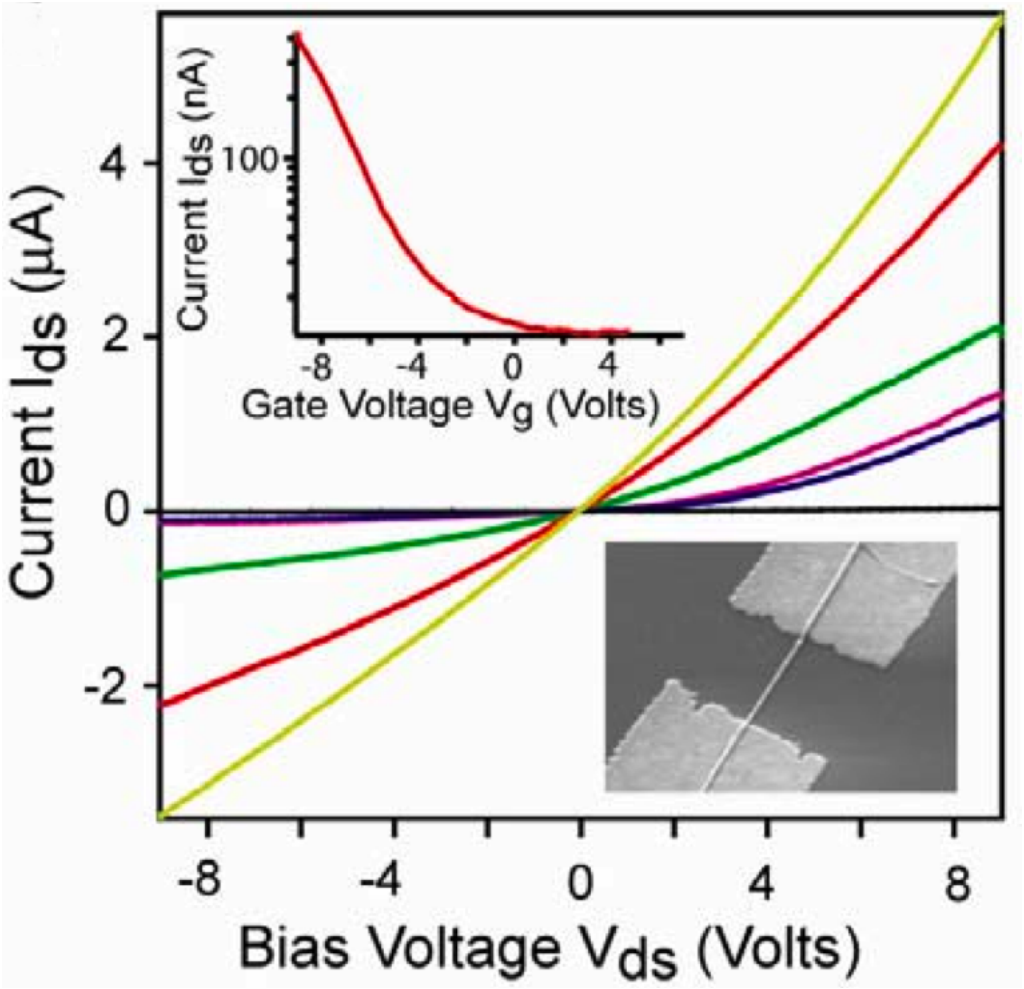

Figure 5.5: Single nanotube transport measurements show typical p-channel FET behavior. Curves were recorded at equally spaced gate voltages ranging from 4V (black) to -6V (yellow). Upper inset, Current versus gate voltage for the same device recorded at a drain-source bias of -2V shows that the current can be completely turned off. Lower inset, scanning electron micrograph (SEM) of actual device. The distance between electrodes is 2 μm.

devices mimic the local gating effects that would be utilized by nanotube sensors. Nanotube transistor devices were fabricated in a back gate geometry [134]. Figure 1E shows the drain-source current (I_{ds}) versus bias voltage (V_{ds}) for a typical nanotube device (grown with a Si:B feed ratio of 1500:1). To measure the gate response of these tubes, we measured Ids versus back gate potential (V_g) at a constant drain-source bias (V_{ds} = -2V). The device shows characteristic FET behavior [135, 136] in which the current turns off around V_g=1V (Figure 1E, inset). This behavior was reproducible over several devices. Of particular note is the strong gate effect. Whereas past studies have dealt with the sensing of molecules and biological species bound to receptor molecules on nanowires [120-123] silicon nanotubes may prove to be unique since every analyte molecule passing through the tube would lie within one Debye length of the gateable channel.

5.3.3 Geometric Control

A unique characteristic of our approach is that it enables independent control of the tube inner diameter and wall thickness. To demonstrate the precision of the growth technique, we grew and characterized samples using a variety of catalyst sizes and shell deposition times. Tubes grown using 5-, 20-, and 80-nm catalyst particles (Figure 2, A-C) were found to have uniform inner diameters of 7.2 ± 1.7, 19.2 ± 2.5, and 75.6 ± 4.3 nm, respectively. Shells deposited on 10-nm cores for 5, 20, and 50 min (Figure 2, D-F) were found to have thicknesses of 3.4 ± 0.5, 5.1 ± 0.3, and 12.3 ± 0.9 nm, respectively, confirming that thickness is a function of deposition time. This type of rational control might enable size and conformation selection of passing molecules,

a desirable attribute for biotechnological applications like nanopore DNA sequencing [100].

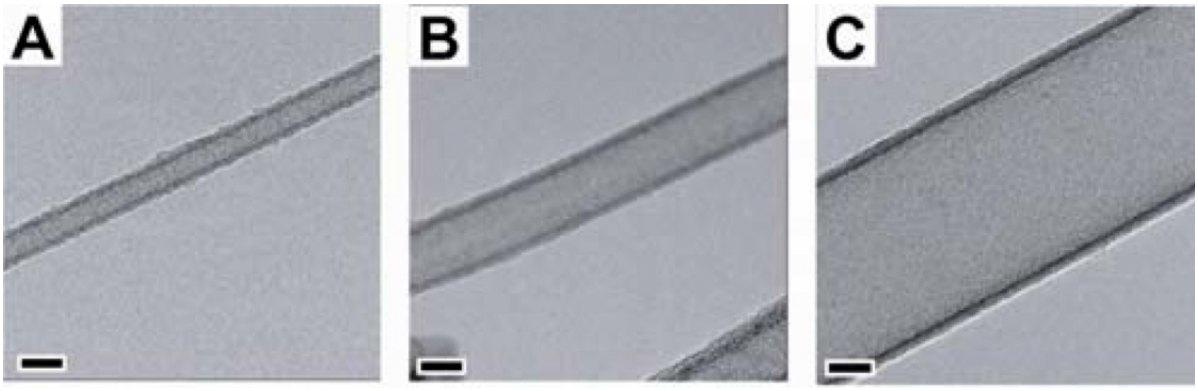

Figure 5.6: Silicon nanotubes having inner diameters of (a) 5 nm, (b) 20 nm, and (c) 80 nm were synthesized using Au catalyst particles of the desired diameter. All scale bars are 20 nm.

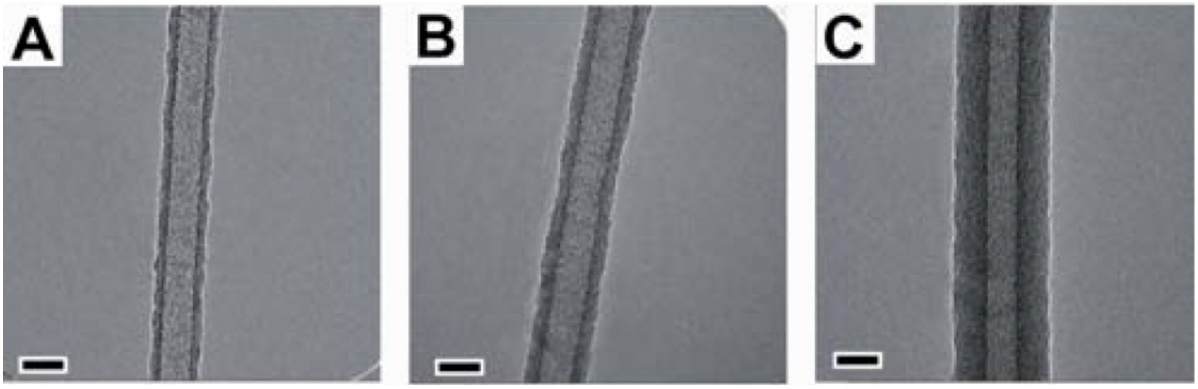

Figure 5.7: Control of wall thickness was also demonstrated by CVD deposition of the shell for (a) 5 min., (b) 20 min., and (c) 50 min. All scale bars are 20 nm.

5.3.4 Nanocones

Our approach can be readily extended to produce a diversity of hollow nanostructure classes. Hollow cones were templated from tapered Ge nanowires formed through a combination of catalyzed axial growth and uncatalyzed radial growth. Such radial growth is promoted by vapor deposition at higher temperatures and germane partial pressures than those used for non-tapered cores. The cone angle increases with core growth temperature, a result of faster overcoating. Cone tapering angles at growth temperatures of 380°C and 400°C (Figure 3, A and B) were respectively measured to be $3.2 \pm 0.7°$ and $8.6 \pm 2.2°$, indicating that the angle can be controlled by deposition temperature. At the higher temperature, the growth substrate was also overcoated with Ge, leading to cones connected by free- standing silicon films (Figure 3B, inset) up to several square millimeters in area, a size scale relevant for filtering applications. Previously, cones have been studied in carbon, but were synthesized in only a few taper angles that were limited by the fullerene lattice [137]. Ours exhibit a further degree of controllability since both the taper angle and wall thickness can be rationally controlled. Such structures could find utility in molecular pumps [138].

5.3.5 Nanotube Networks

Growth of a second derivative class, branched nanotube networks, was inspired by recent work on branched Si, GaN, and GaP nanowire structures [139, 140]. Branched Ge nanowire networks were grown and then etched away after the deposition of a Si shell. Apertures between parent and branch nanotubes were fully open (Figure 3C). Using a higher catalyst density resulted in multiple branches within close proximity

Figure 5.8: Nanocones templated from highly tapered Ge cores grown at 380°C. Scale bar is 200 nm. Inset: The base of a typical cone, viewed at an oblique angle, is round and hollow (scale bar, 200 nm).

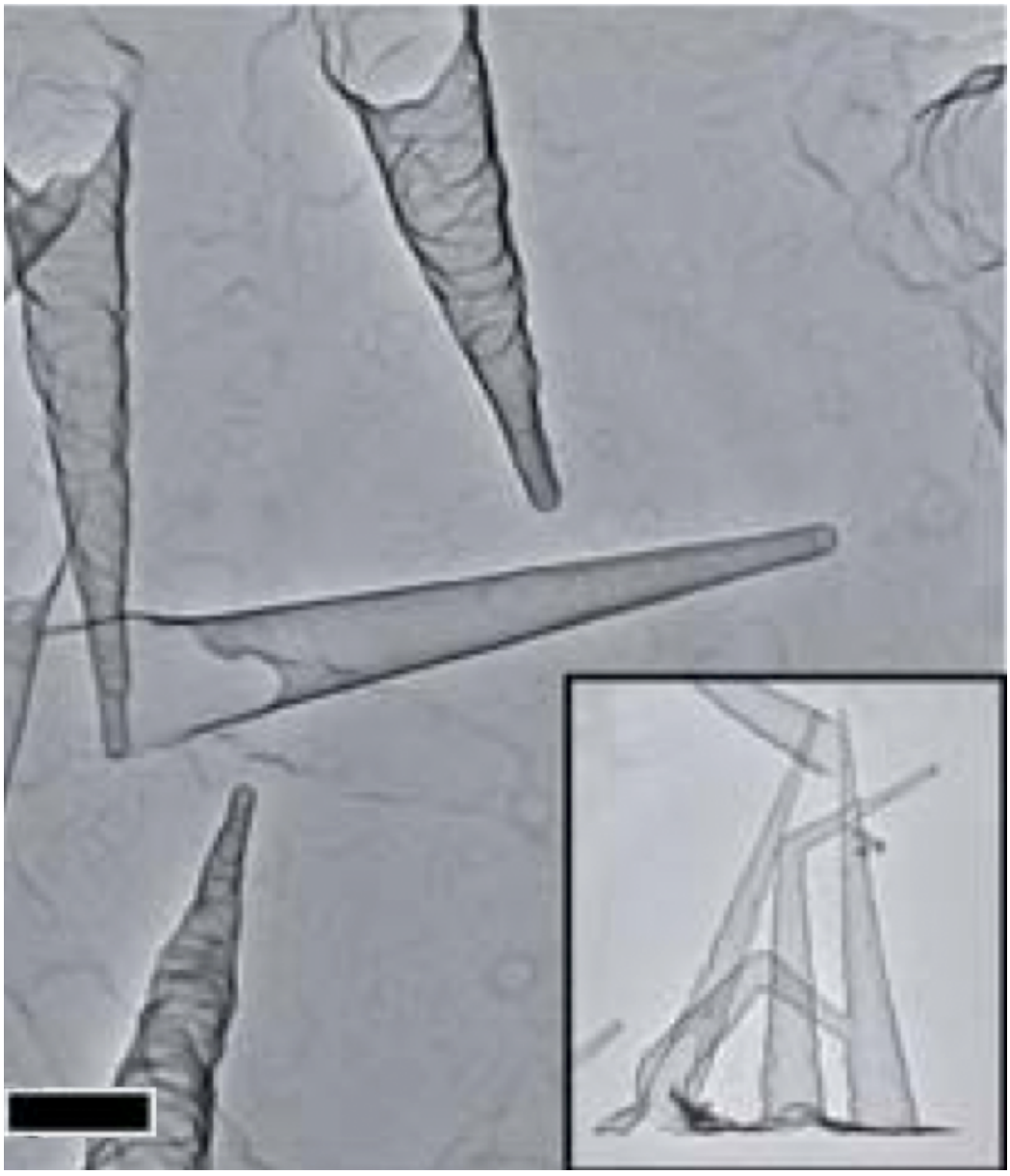

Figure 5.9: Nanocones templated from highly tapered Ge cores grown at 400°C. Scale bar is 200 nm. Inset: At the higher temperature, the cones are connected by a solid silicon film.

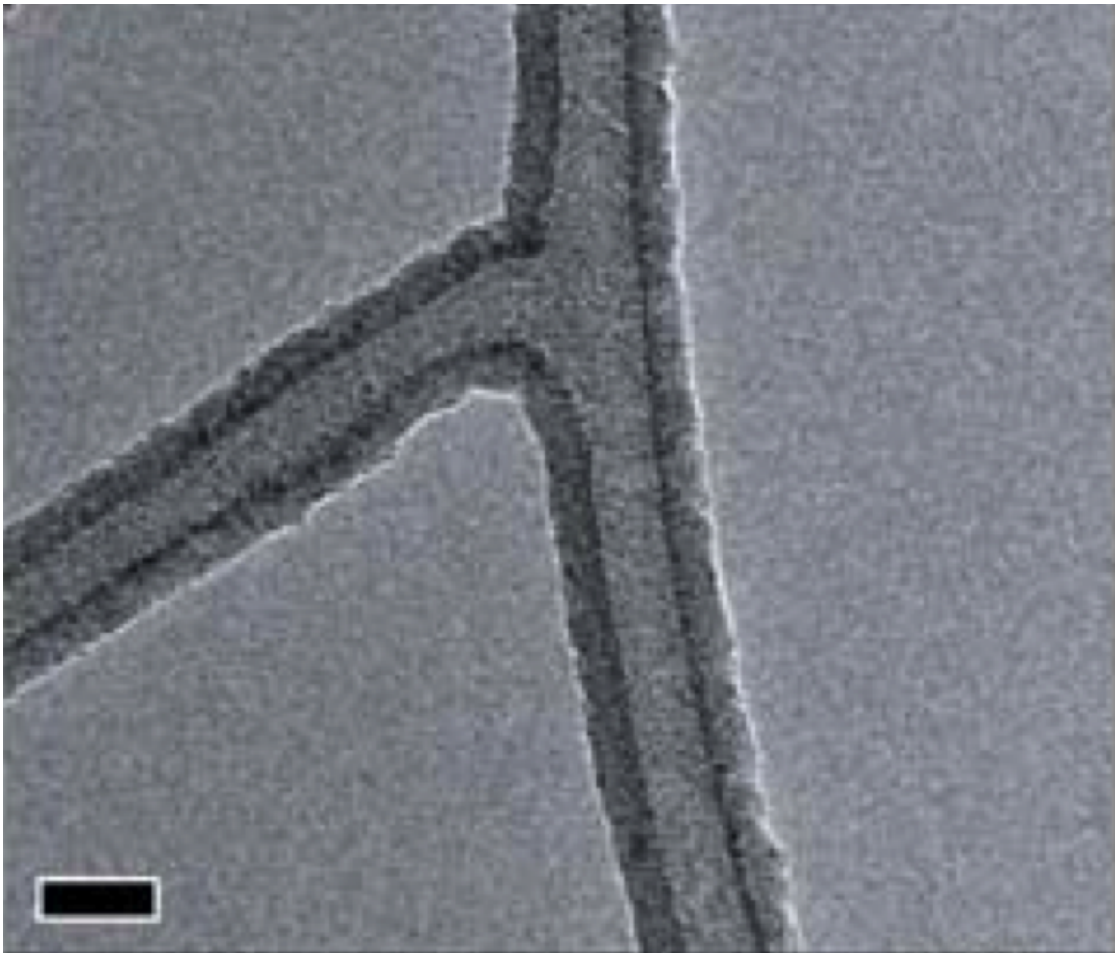

Figure 5.10: Grafted heterostructures were etched to yield branched Si nanotube networks with open junctions. Examples of a singly-branched nanotube is shown. Scale bar is 20 nm.

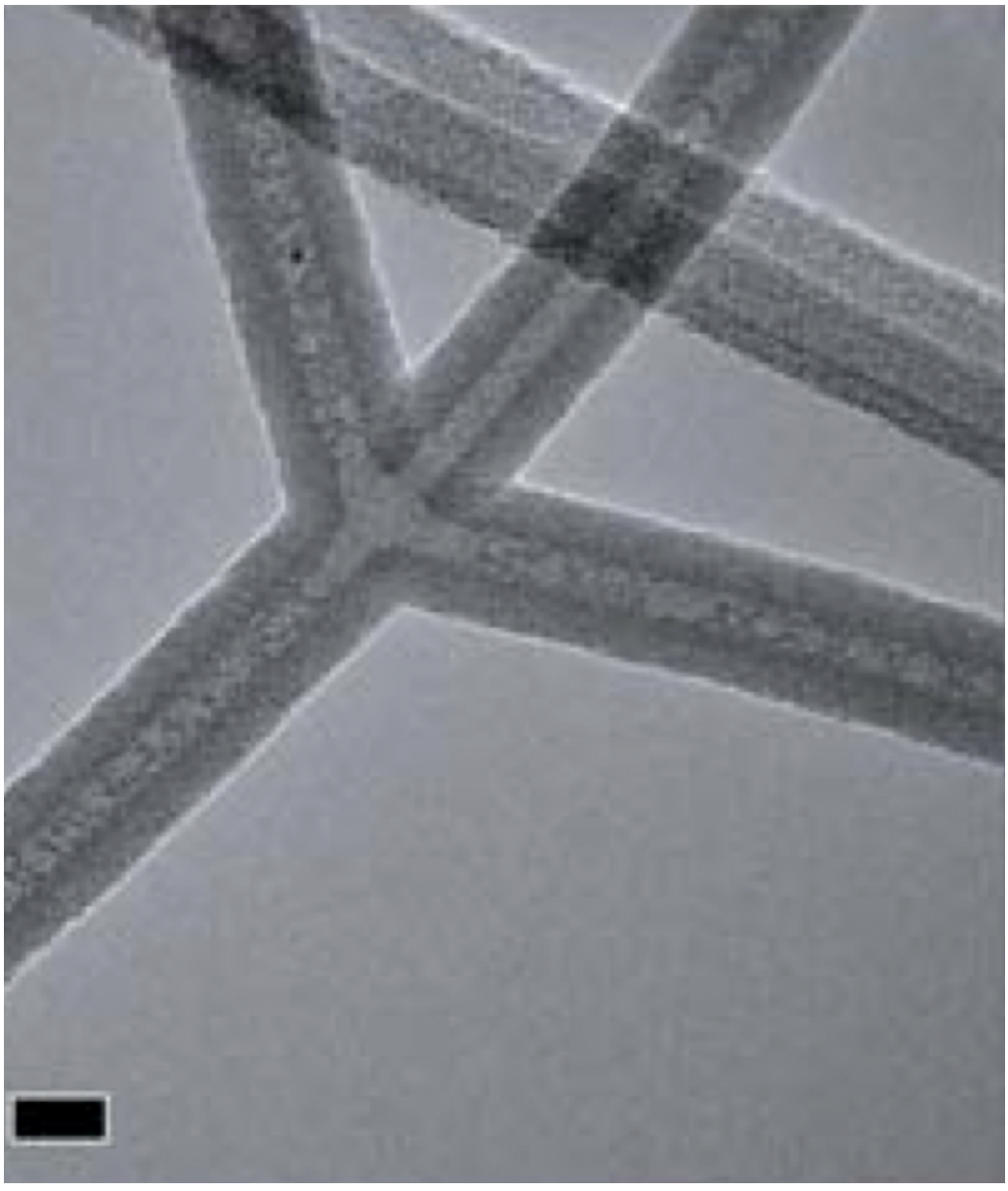

Figure 5.11: Grafted heterostructures were etched to yield branched Si nanotube networks with open junctions. Examples of a doubly-branched nanotube is shown. Scale bar is 20 nm.

(Figure 3D). In both cases, the branch angles with respect to the parent nanowire axis were measured to be ca. $60° - 70°$, consistent with previously reported data [139]. These branches could be useful for fluid delivery, enabling delivery of an ionic flow to multiple locations by selectively pinching off flows with local electrical gates [125-127].

5.3.6 Electroosmotic Transport

To demonstrate electroosmotic transport of fluids, a silicon nanotube was used to connect two fluid reservoirs separated by a 10-μm polymer barrier. A pair of gold electrodes, lithographically defined on the glass substrate prior to barrier fabrication, allowed an electric field to be imposed (Figure 4A,B). To demonstrate transport, one reservoir was filled with 90 μM (aqueous) Oregon Green 488 dye (2',7'- difluorofluorescein) while the other was filled with water. Confocal microscopy was used to observe the fluorescence and hence the diffusion/migration of the dye. Before applying a field, the tube appeared dark (Figure 4C). Initially, the dye did not diffuse into the tube because of repulsive forces between the negatively charged molecule and the oxidized silicon surface. Applying a field of ca. 10 kV/cm across the tube drove the dye through the structure. Each reservoir measured 1 cm $\times$ 1 cm. The electrodes were 5 mm apart (with the separating barrier in the middle). Modeling the system as series resistances, one can assume that nearly the entire potential drop occured across the fluid-filled nanotube because of its relatively minuscule cross sectional area. Fluorescence was observed clearly through the wall of the tube (Figure 4D) as well as at the open end (Figure 4E) where the dye diffused into the water-filled reservoir.

5.4 Conclusion

Thus, we have demonstrated that it is possible not only to achieve gateable electronic behavior, but also to achieve molecular transport under applied fields. These novel functionalities, in addition to our ability to finely control size and geometry, indicate that our single-crystal nanotubes are candidates for integrated electro-fluidic devices capable of simultaneously transporting, processing and sensing fluids on the sub-attoliter scale.

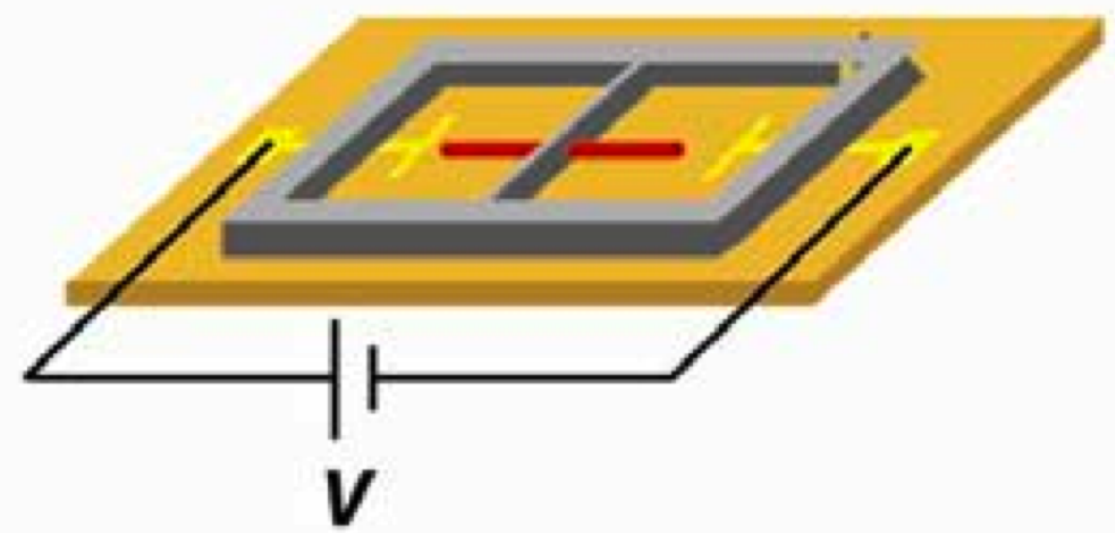

Figure 5.12: Schematic of single nanotube device with fluid reservoirs on either end.

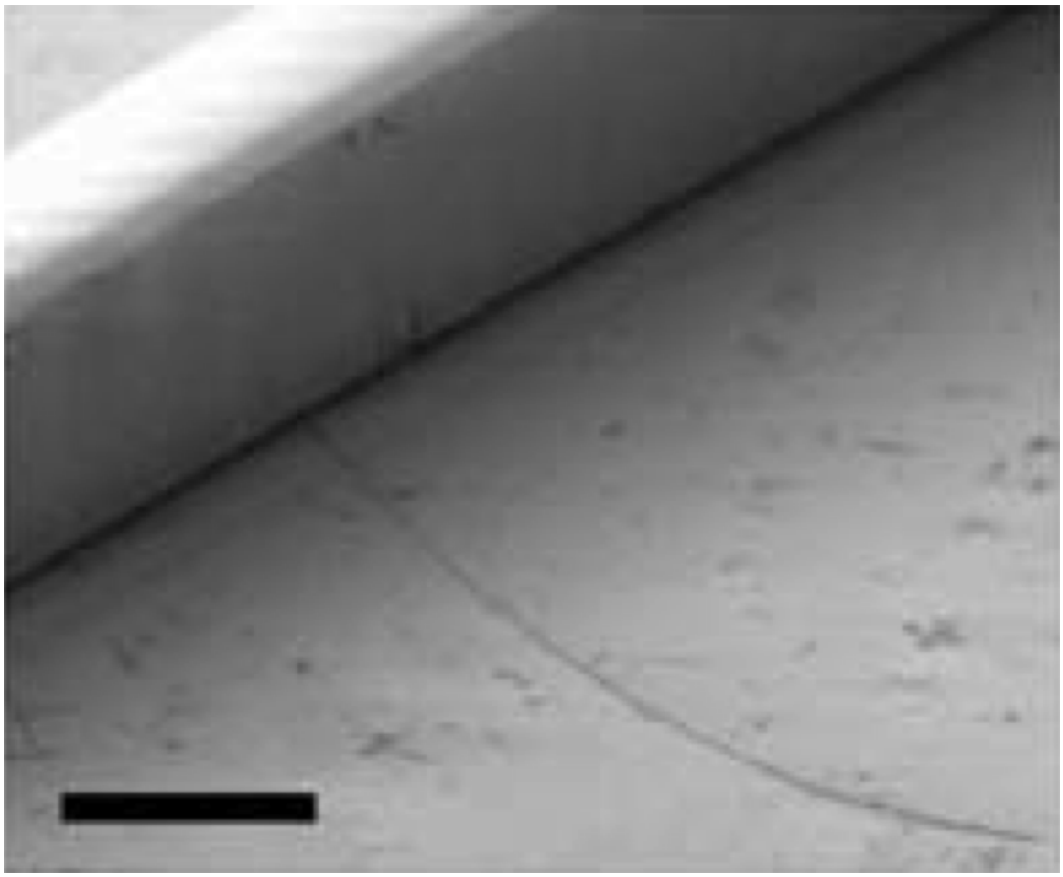

Figure 5.13: SEM of a representative nanotube device taken at a 45° tilt. Scale bar is 20 μm.

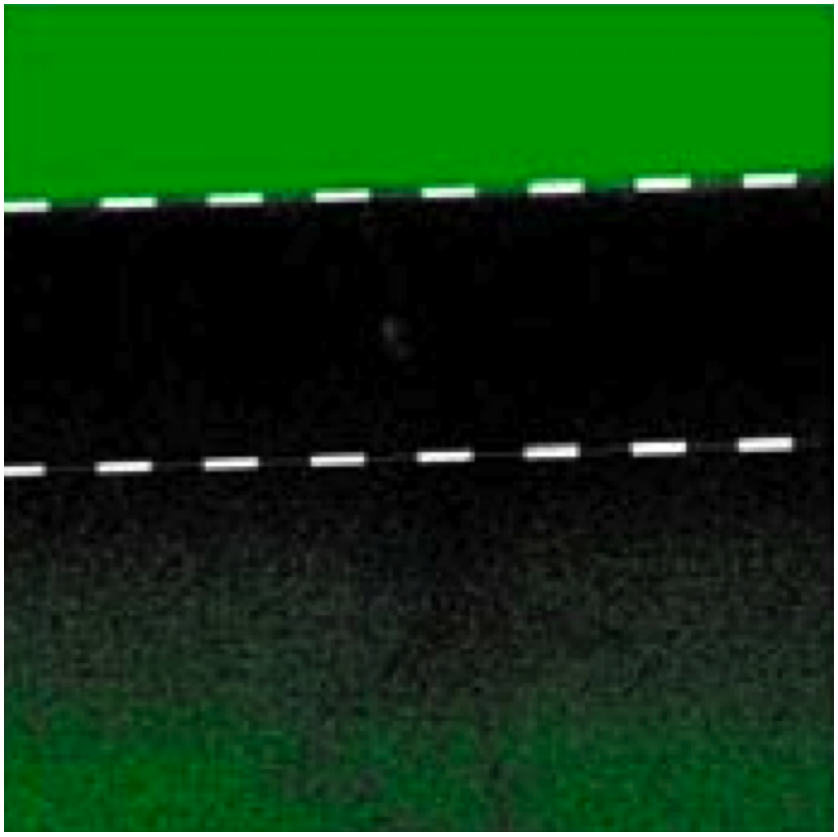

Figure 5.14: Epifluorescence microscopy was used to study the transport of dye between two reservoirs via tubes. Initally, the tube did not contain dye.

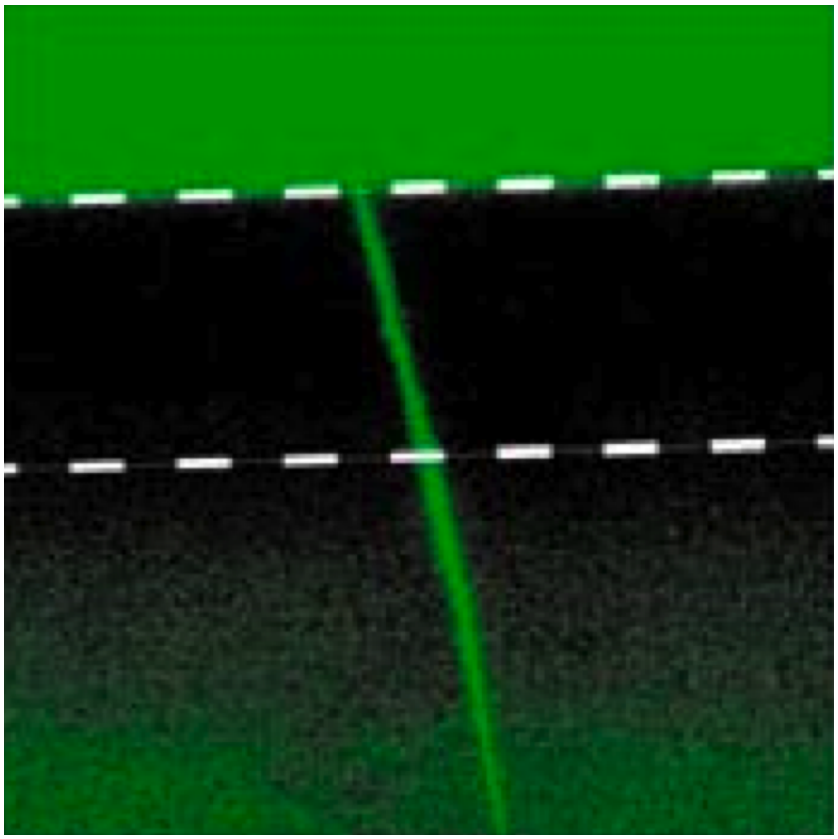

Figure 5.15: Upon applying an electric field, the dye solution filled the tube and was transported to the other (water-filled) reservoir. The dotted line shows the position of the SU8 barrier.

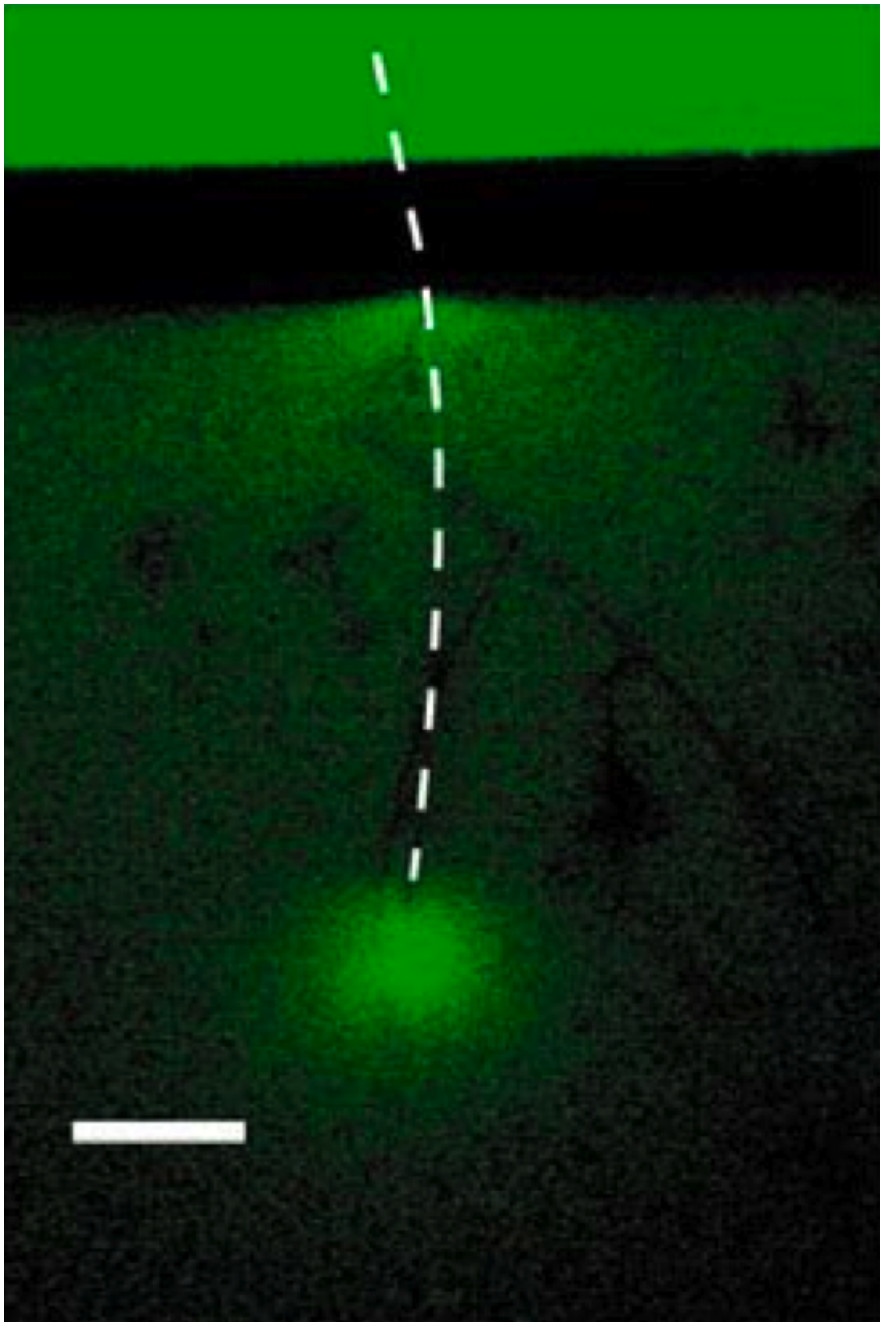

Figure 5.16: Image of same tube, showing diffusion of dye away from the open end. The dotted line shows the position of the tube. Scale bar is 20 μm.

Chapter 6

Mechanical Programmability

6.1 Introduction

Granular fluids are an industrially and scientifically relevant class of vibrationally programmable matter [141]. Thin layers of hard spheres in a vertically oscillated container have demonstrated a rich set of spatial patterns beyond Faraday wave predictions that can be selected by tuning the container floor's oscillation frequency and amplitude [142-144]. More complex patterns can be selected with multiple frequency forcing [144]. In the continuum limit, arbitrary wave fields have even been demonstrated in traditional liquid tanks [145].

Such programmability suggests that granular fluid patterns might be harnessed as force fields for parallel manipulation tasks. Parallel manipulation of small numbers of parts using many degrees of actuation has received considerable theoretical [146, 147] and experimental [148] attention. Parallel positional control of free bodies as short as 3 mm and as light as 8.6 g has been achieved using arrays of MEMS actuators

[149]. However, the inverse problem of manipulating large numbers of parts with only a few degrees of actuation ("minimalist manipulation") has received less attention. The most noteworthy accomplishment in this direction has been the demonstration of a planar manipulator with global rotational and translational degrees of freedom [150]. So far, such planar manipulators have only been able to positionally address centimeter-scale objects, necessitating new methods for minimalist manipulation at smaller length scales. Controlled tossing of surface impurities by patterned granular fluids is one promising approach, since granule diameters can be scaled down to 100 μm while preserving pattern formation [151].

While the vertical dynamics of a large intruder particle submerged in a deep granular bed have been investigated previously (e.g., in connection with the Brazil nut effect), both experimentally [152, 153] and numerically [154], the dynamics of an intruder at or near the surface of a thin granular layer have not been addressed. This report addresses the dynamics of surface impurities on vibrofluidized granular patterns with two-dimensional numerical simulations.

6.2 Simulation Details

6.2.1 Granular Interactions

A hard-disk two-dimensional molecular dynamics simulation was constructed, incorporating angular momentum, friction, and inelastic collapse avoidance [155]. The simulated container had a high ceiling and width W delimited by fixed horizontal boundaries. At the beginning of each trial run, a granular bed of N monodisperse

Table 6.1: Parameters used for inelastic collisions.

Parameter	Granule-granule	Granule-boundary
μ	0.2	0.2
β_0	0.0	0.0
ϵ_0	0.4	0.2

disks with diameter d_0 was initialized. Granules were initially placed in a square lattice with separation $2d_0$, horizontal and vertical velocity components randomly distributed in the interval $[-0.1, 0.1]$ ms^{-1}, and no angular momentum.

The simulation was event-driven. A calendar with the next scheduled collision event for each granule was kept, and selectively recalculated after each collision [156]. In collisions of granules with container walls and each other, a velocity-dependent coefficient of restitution [157],

$$\epsilon(v) = 1 - \epsilon_0(v/v_0)^{0.2}, \tag{6.1}$$

was used where v is the component of the relative velocity normal to the tangent plane of collision, $v_0 = 1.0$ ms^{-1}. Additional energy was dissipated by friction, parameterized by the coefficient μ. Following Rapaport [158], relative tangential restitution above a critical impact angle was eliminated, with a maximum coefficient of tangential restitution, β_0. Inelastic collapse was avoided by setting $\epsilon(v) = 1.0$ below a cutoff $v_{\text{crit}} = 10^{-6}$ ms^{-1}. The collisional parameters used for these experiments are summarized in Table 6.1.

6.2.2 Floor Vibration

By convention, the floor height $y(t)$ of a vibrated container evolves as

$$y(t) = -\Gamma g(2\pi f)^{-2}\cos(2\pi f t), \tag{6.2}$$

for frequency f and dimensionless amplitude Γ. To determine the accuracy of the numerical implementation, the dependence of λ on f, Γ, and N was measured. These tests were performed in an aperiodic container with $d_0 = 1.5$ mm, $W = 100d_0$, $N = 600$, $\Gamma = 3.6$, and $f = 10$ Hz unless otherwise varied. Wavelengths were extracted by calculating the first nonzero peak in the autocorrelation function of the granules' horizontal distribution:

$$C_{x,x}(\lambda') = (W - \lambda')^{-1} \int_0^{W-\lambda'} h(x)h(x + \lambda')dx. \tag{6.3}$$

The horizontal distribution was found by integrating granule positions over 10 s. Previous results [157] were well reproduced across a broad parameter range.

6.2.3 Measurements

The main experiment was conducted with parameter values $\Gamma = 3.6$, $f = 10$ Hz, $g = 9.8$ ms^{-2}, $N = 180$, and $d_0 = 1.5$ mm. The horizontally periodic container, with $W = 30d_0$, was chosen to favor the fundamental mode of the 6-layer bed oscillated at the given values of f and Γ [155], in which at most one pattern peak existed at any time. In addition to the computational benefit of this container geometry, the granular force field resembled the desired application of multiple intruders being consecutively tossed by a single peak.

The time evolutions of intruders were measured. The granular fluid was first given $t_0 = 0.6$ s to develop patterns, after which one diameter d_0 and mass m_0 granule was removed and reintroduced as an intruder with diameter d_I and mass m_I. The intruder was created at rest at a height of $40d_0$ above the mean floor position, and horizontally centered (an undistinguished position, as the boundary conditions were periodic).

Simulations were halted after 2 s. For each combination of $d_I/d_0 = 1, 3, 5, \ldots, 23$ and $m_I/m_0 = 1, 2, 4, 8,$ 100 trials were conducted in which the initial granule velocities were randomized. An example of an intruder being tossed is shown in Figure 6.1.

6.3 Results and Discussion

6.3.1 Evolution of Intruder Displacement

The mean square horizontal displacement $\langle \Delta x^2 \rangle$ of the intruder ensemble over these trials was calculated as a function of time over their 1.4-s existence. At $m_I = m_0$ and $d_I \geq 5d_0$, the time evolution of $\langle \Delta x^2 \rangle$ was approximately linear after 0.1 s and consistent with Brownian diffusion (see Figure 6.2). Self-diffusion coefficients were therefore fitted to the last 1.2 s of $\langle \Delta x^2 \rangle$, ignoring the first 0.2 s of ensemble relaxation.

The self-diffusion coefficients calculated for each intruder diameter and mass are shown in Figure 6.3.

6.3.2 Comparison with Theory

Consider, as a model for surface intruder dynamics, self-diffusion in a standing wave potential

$$U(x,t) = A \sin(2\pi x/\lambda) \sin(\pi f t), \tag{6.4}$$

for pattern wavelength λ and container vibration frequency f, parameterized by horizontal self-diffusion coefficient D, defined by

$$D \equiv \frac{1}{2} \lim_{t \to \infty} \frac{\langle [x(t_0 + t) - x(t_0)]^2 \rangle}{t}. \tag{6.5}$$

Since $U(x,t)$ is the sum of equal counterpropagating waves with $\omega_1 = \omega_2$ and $k_1 = -k_2$, no intruder drift velocity (Stokes drift) can be induced without diffusion [159].

However, discrete collisions of a large surface intruder with supporting granules constitute a diffusion mechanism. The drift velocity including diffusion [159] is given by

$$v \propto (1+\alpha_1^2)^{-1} - (1+\alpha_2^2)^{-1}, \tag{6.6}$$

where $\alpha_i = D|k_i|^2\omega_i^{-1}$ and $i = 1, 2$. For a pure standing wave, this expression vanishes. Consider therefore an imperfect standing wave with $k_1 + k_2 = \delta k$, which is more realistic for granular patterns. In this case, it follows that

$$v \propto \frac{D^2\omega_1^{-2}|k_1|^3\delta k}{\left(1+(D\omega_1^{-1}k_1^2)^2\right)^2}. \tag{6.7}$$

If diffusion dominates the classical Stokes drift, then $\alpha_1 \gg 1$ and $v \propto D^{-2}$, while if the classical drift dominates, then $\alpha_1 \ll 1$ and $v \propto D^2$. In the case of surface intruder tossing, classical drift is expected to dominate, since the intruder will spend much of its time in free flight above the granular bed. The acceleration of an intruder in contact with a rising pile of granules will be proportional to its diameter and inversely proportional to its mass (assuming constant bed pressure), so $v \propto m_I^{-1}d$ and $D \propto m_I^{-0.5}d_I^{0.5}$.

The diffusivity relation was fit by the power law

$$D = k(m_I/m_0)^\alpha(d_I/d_0)^\beta, \tag{6.8}$$

for $k = (19.1\pm2.8)$ cm^{2}s^{-1}, $\alpha = -0.74\pm0.07$, and $\beta = 0.37\pm0.06$. The fitted exponent β was more consistent with the 0.5 exponent expected from dominant Stokes drift

than the -0.5 exponent expected from dominant diffusion in a continuum. The fitted value of α was 3.5σ away from the -0.5 value expected for intruder tossing.

6.3.3 Analysis of Horizontal Self-Diffusion

For the intruder to remain near a single trough in the granular bed, it should remain within $\pm\lambda/4$ of the trough's horizontal position, because the distance between a peak and the adjacent peak that rises after time T is $\lambda/2$. Hence, the desirable self-diffusivities are constrained:

$$D \leq (\lambda/2)^2/(2T) = f\lambda/8. \tag{6.9}$$

For the standard parameters [157] of the main experiment reported here, the intruder types that are positionally stable are constrained by

$$\frac{f\lambda}{(m_I/m_0)^\alpha (d_I/d_0)^\beta} \geq 152.8 \text{ cm}^2\text{s}^{-1}. \tag{6.10}$$

Additionally, the average height of the bottom of the intruder was measured as a function of diameter for various masses. For $d_I \geq 5d_0$, the bottom height saturated at $\sim 25d_0$, indicating that the intruder was, in fact, supported by the granular bed and did not crush it.

6.4 Conclusion

The horizontal self-diffusivities of surface impurities of various diameters and masses were found to scale with mass exponent -0.74 ± 0.07 and diameter exponent 0.37 ± 0.06, consistent with dominant Stokes drift. A constraint on the relative

masses and diameters of impurities that diffused slowly enough to remain horizontally stable over multiple container oscillations was derived.

This result is a step toward granular fluidic manipulation, in which the container oscillation function is tuned to individually address the motion of multiple impurities of different masses and diameters. In particular, by varying the container frequency, intruder particles might be made to cross this boundary in mass-diameter phase space and be immobilized, while a few are freed for manipulation by additional degrees of freedom. A better understanding of such degrees of freedom as horizontal shaking [160] should therefore be relevant for future studies.

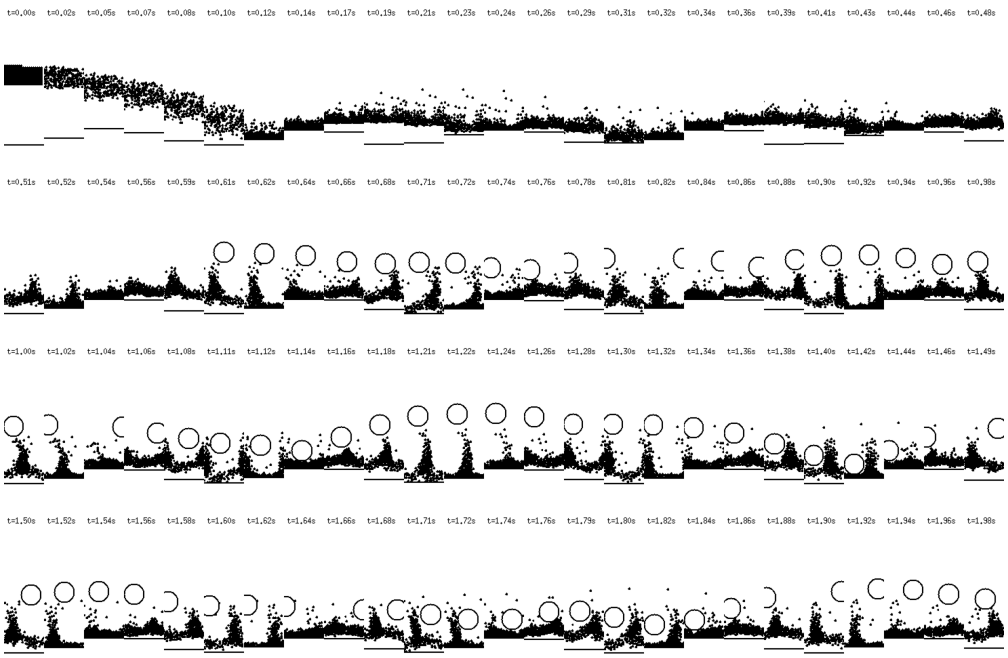

Figure 6.1: Evolution of an intruder ($m_I/m_0 = 1$, $d_I/d_0 = 15$) tossed by a granular pattern over 2 s.

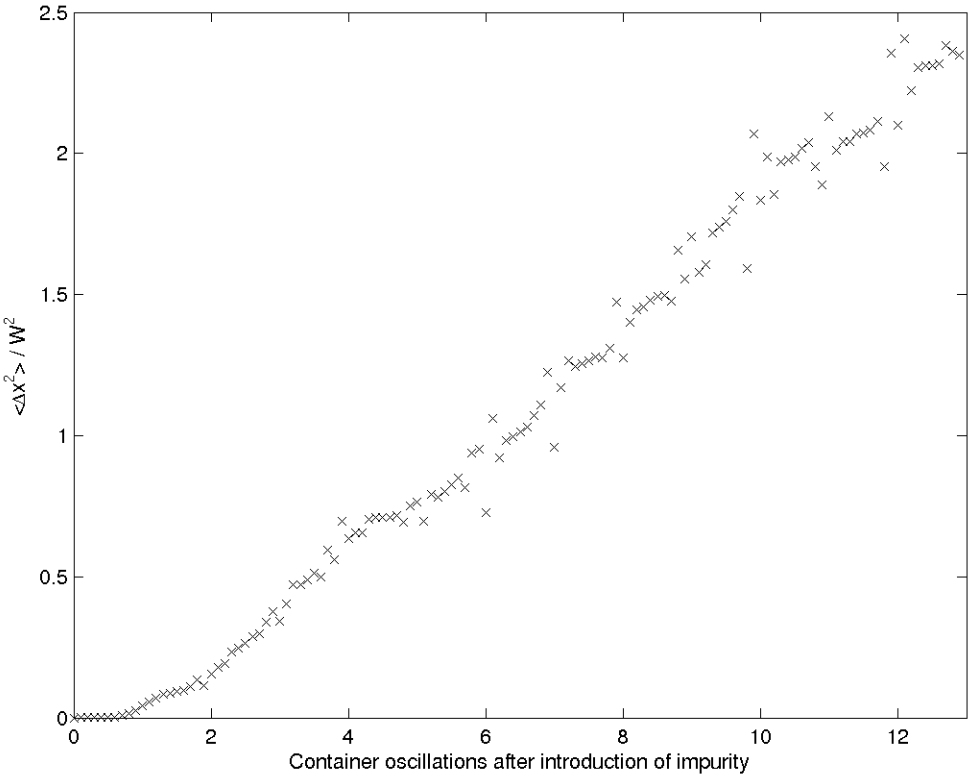

Figure 6.2: Example evolution of intruder ensemble's mean square horizontal displacement ($m_I/m_0 = 1$, $d_I/d_0 = 7$), normalized by the squared container width.

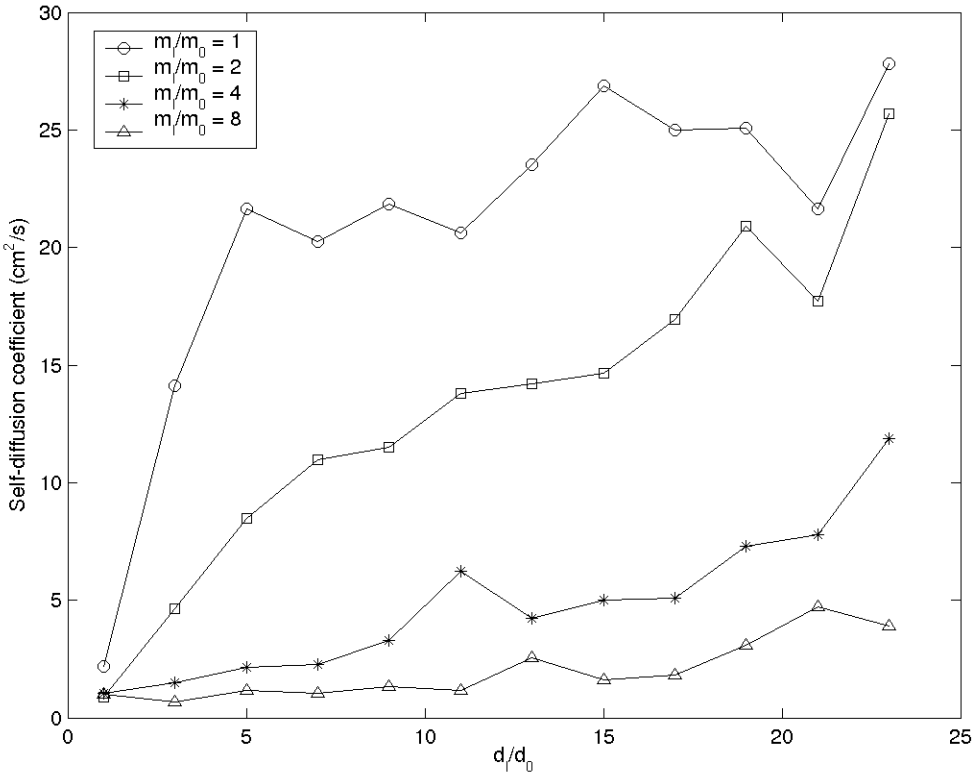

Figure 6.3: Horizontal self-diffusion rates for various relative intruder masses, m_I/m_0, and diameters, d_I/d_0.

Chapter 7

Magnetic Programmability

7.1 Introduction

There has been much recent interest in programmable self-assembly of biological and material components [161-163]. Two very general features of self-assembly are particularly noteworthy for such applications. First, for a collection of n components, each of which can take one of k states, the total number of possible (not necessarily local) instantaneous interactions is $k^{k^{O(n)}}$, since the future state of each component can be determined by any subset of the collection of current component states. In contrast, the total number of configurations of the collection is only kn, and so it may be concluded that interaction spaces are generically larger than configuration spaces. Second, self-assembly often necessitates multiple cooperating or competing interactions as seen, for example, in genetic coexpression [164] and hydrophobic-hydrophilic protein folding [165]. It would therefore be interesting if an entire interaction space could be systematically surveyed to eventually enable rational tuning of multiple

interactions for controlled self-assembly.

Ising spin lattices are an excellent testing ground for such self-assembly processes as applied to magnetic programmability. It has been shown previously that the equilibrium statistical mechanics of Ising models in $d + 1$ dimensions are dual to the time development of cellular automata in d dimensions [166]. Therefore, in order to exercise programmable control over the magnetic state of a 2-dimensional surface, it is reasonable to focus our attention on the rich time evolutions of 1-D cellular automata, which we shall do in this chapter. Of course, cellular automata are attractive models in their own right for self-assembly [167].

In particular, the 256 rules of elementary cellular automata (ECA) [168] are a model class of the dual local interactions whose approximations and statistical behavior have been studied in detail [169, 170]. It has been found that single iterations under the elementary cellular automata rule set are approximately linearized by a surprisingly small number of principal components [170]. However, single iterations do not capture the rich behaviors of cellular automata that require feedback between sites [168]. In the present work, in order to better understand the co-expressive behaviors of cellular automata rule spaces, we study for the first time the co-evolution of common initial configurations under ensembles of entire rule classes. In contrast to single-iteration studies [170], the ensembles considered in this paper consist of multiple applications of individual rules, which introduce nonlinearity that has not, to the best of our knowledge, been studied previously.

Rule ensembles may not have received significant attention previously because they typically include non-quiescent rules [171] that invert null initial states. (In this

work, periodic boundaries are imposed, in part to avoid boundary artifacts from such non-quiescent rules.) While ensembles can certainly be approximated by typically large samples of stochastic cellular automata, stochastic ensembles of small finite state automata have received the most scrutiny [172]. Finally, an ensemble of ECA can be embedded in a 2^{256}-color automaton, so perceived complexity may also have discouraged previous studies.

7.2 Simulation Details

In this work, we will focus primarily on the mean evolution of entire classes of transition rules, and in particular the ECA class. We define the equal weighting of ECA rules at position x and iteration n as

$$e_{n,x} \equiv \frac{1}{256} \sum_{k=0}^{255} s_n^k(x),$$

where $s_n^k(x)$ is the value at position x and iteration n of an elementary cellular automaton obeying transition rule k (following Wolframs notation [168]) that acts on a periodic configuration of size L. For simplicity, our early discussion assumes an initial configuration of $\overbrace{1000\cdots000}^{L-1}$. However, in later discussion, other initial configurations and transition rule classes are considered, while maintaining an equal rule weighting.

7.3 Results and Discussion

7.3.1 Ensemble Evolution

Consider the evolution of a single site, averaged with equal weighting over all elementary rules, as shown in Figure 7.1(a). The evolution is eventually periodic with period 2, because that is the least common multiple of cycle sizes over the 4 possible 2-state automata rules. The same periodicity is reflected in the alternating behavior of backgrounds under non-quiescent rules [168]. Because the rule set is symmetric in site replacement values, the ensemble takes the value 1/2 at iteration 1. For subsequent even iterations, the ensemble takes the value 3/4 because 3 of the 4 possible 2-state automata are stationary after a single iteration and the remaining automaton is a 2-cycle that returns to its initial state after two iterations. Uniform-valued initial configurations must also have this ensemble oscillatory behavior by translational symmetry.

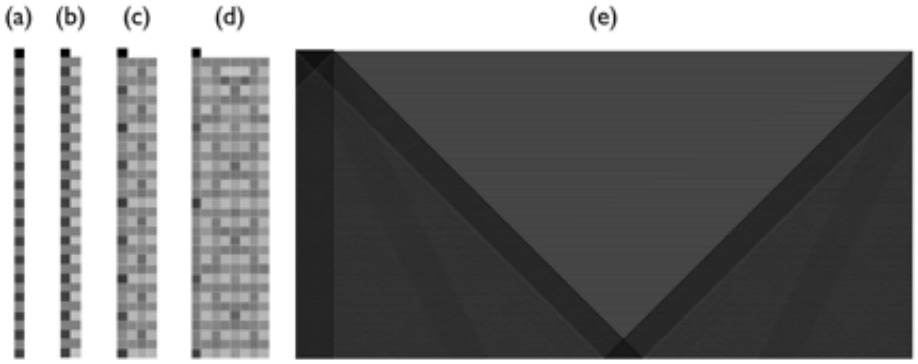

Figure 7.1: Visualization of evolution of configurations of different sizes. (a-d) Evolutions for time T=32 of initial configurations with a single nonzero initial site and sizes (a) 1, (b) 2, (c) 4, and (d) 8. (e) Evolution of 32 adjacent nonzero sites in a configuration of size L=512 over time T=256. Contrast is enhanced to reveal the presence of fronts with speeds 0, $\pm c/2$, $\pm c$. The downwards direction corresponds to successive iterations.

More interesting behavior is observed in the evolution of initial configurations of larger sizes consisting of a single nonzero site. For configuration sizes $L = 2, 4, 8$, as shown in Figure 7.1(b-d), propagation fronts traveling at the maximum allowed velocities $\pm c$ are discernible against a background 2-cycle. Surprisingly, the propagation fronts reach finite asymptotic amplitudes, and do not weaken through intersection, despite the fact that few elementary rules are linear [173]. Moreover, in the evolution of large configurations, faint fronts traveling at velocities $\pm c/2$ are also visible, as seen in Figure 7.1(e). Such narrow peaks do not appear to be present in any of the individual cellular automata evolutions from individual sites [173]. These well-defined structures beg the question of what other collective velocities, if any, are represented in the dispersion of elementary cellular automata ensembles, which we will revisit shortly.

7.3.2 Density Evolution

But let us first examine the asymptotic behavior of these ensembles, since they appear not to homogenize, as might be naively expected for the average of uncorrelated discrete evolutions. The fraction or density of sites at iteration n with value 1, $\lambda(n)$, is a useful statistical measure of a cellular automaton's equilibration [168]. Here, we will define $\lambda(n)$ as additionally averaging over an entire rule set. As visible in Figure 7.1(b-d), for a range of configuration sizes, $\lambda(n)$ follows approximately a 2-periodic orbit. The even-iteration value in the orbit appears to approach 1/3 with increased configuration size, while the odd-iteration value approaches $\sim$0.531, as can be seen in the large-configuration limit of Figure 7.2(a-b). After L/c iterations, the

even- and odd-iteration density attractors both remain within 2% of their respective asymptotic averages. An odd-iteration attractor close to 1/2 is expected because that is the density in early odd iterations in the limit of large, nearly empty configurations. However, the origin of these particular limit values is still anomalous. Equilibration occurs partially after $L/(2c)$ iterations and almost completely after approximately L/c iterations, consistent with the times required for fronts with speed c to first cross each other and then traverse the entire configuration. Additionally, Figure 7.2(a-b) confirms that the fronts are wave-like and spatially localized, since the densities do not converge to 1.

By examining the evolution from initial configurations of varying densities, it is also possible to separate out the asymptotic contribution of the propagation fronts from the background, as shown in Figure 7.2(c-d). The asymptotically linear interference of the propagation fronts is reflected by the quasi-linearity of both curves. This quasi-linear density dependence is somewhat surprising given the sensitive, non-linear dependence on initial conditions of many individual rules. It should be noted, however, that initial densities $\lambda(0)$ near 0.0 or 1.0 lead to asymptotic densities $\lambda(T), \lambda(T-1)$ that diverge from the linear trend. For example, while $\lambda(T) \to 1/3$ as $\lambda(0) \to 0^+$, $\lambda(T) = 1/4$ for $\lambda(0) = 0$.

7.3.3 Velocity Spectrum

Now that we have discussed the non-interaction of the fronts, we return to our analysis of the front velocities, motivated by the visibility of faint $\pm c/2$-velocity fronts in ensembles. In particular, let us examine the ensemble that evolves from a single

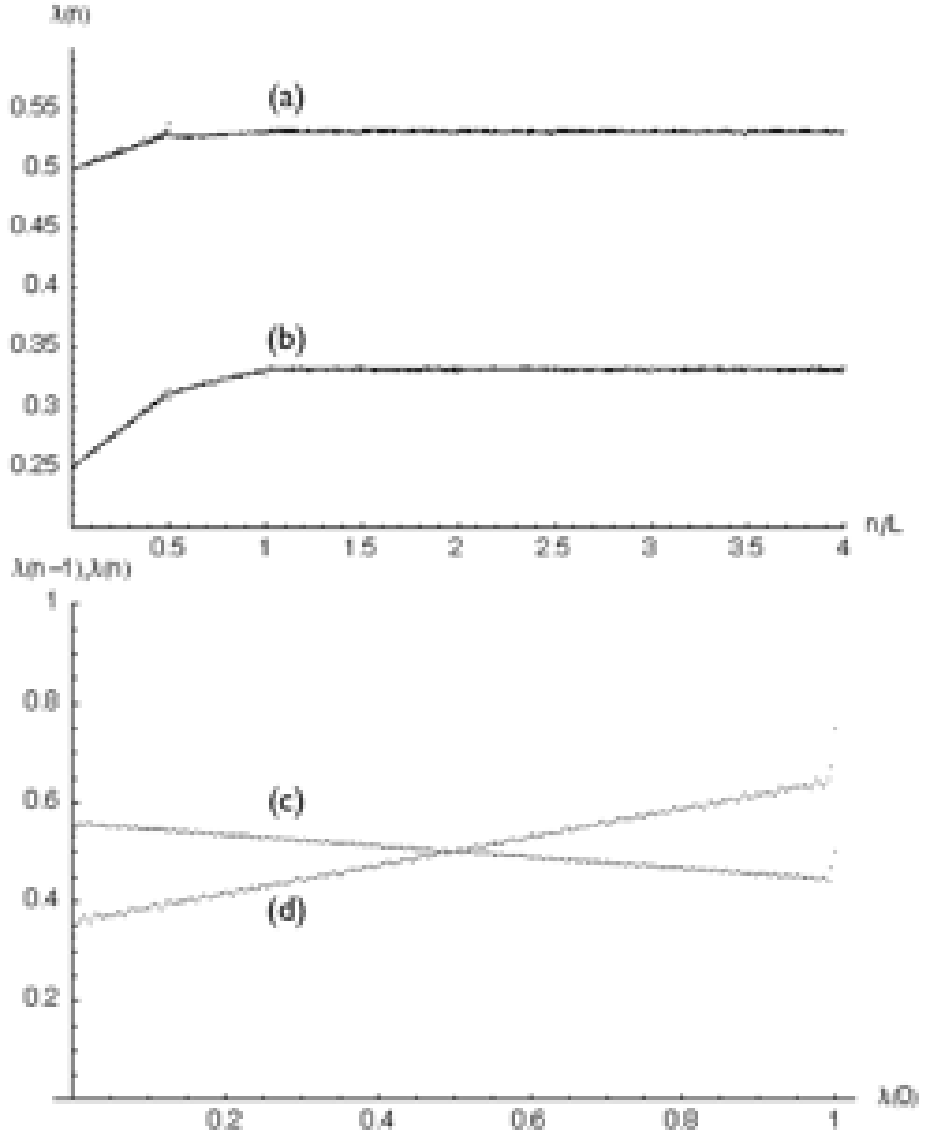

Figure 7.2: Equilibration of ensemble patterns. (a-b) Evolution of density $\lambda(n)$ for (a) odd and (b) even n (L=512, T=2048). (c-d) Equilibrium densities at (c) odd and (d) even iterations from initial configurations with varying density $\lambda(0)$ (L=256, T=256.)

site over time $T \gg L/c$ (i.e., after the primary $\pm c$ fronts have crossed many times), according to the correlation measure,

$$f_0(v) = \frac{2}{T-1} \sum_{n\text{even}, 0 \le n \le T-2} \Big((\lfloor vcn \rfloor + 1 - vcn) \cdot e_{n,\lfloor vcn \rfloor} + (vcn - \lfloor vcn \rfloor) \cdot e_{n,\lfloor vcn \rfloor + 1} \Big)$$

$$f_1(v) = \frac{2}{T-1} \sum_{n\text{odd}, 1 \le n \le T-1} \Big((\lfloor vcn \rfloor + 1 - vcn) \cdot e_{n,\lfloor vcn \rfloor} + (vcn - \lfloor vcn \rfloor) \cdot e_{n,\lfloor vcn \rfloor + 1} \Big)$$

where v is the fractional velocity and $e_{n,x}$ is the mean ensemble value at iteration n and displacement x from the single nonzero initial site. Note that linear interpolation was used in the above measure to avoid aliasing artifacts. The resulting velocity spectra over odd and even iterations are shown in Figure 7.3(a-b). Further interference modes with low-denominator fractional speeds become evident, the most prominent being $c/5$, $2c/5$, $3c/5$, and $4c/5$ on even and odd iterations and $c/3$ and $2c/3$ on odd iterations. We believe that the origin of such well-defined collective speeds in the mean ensemble over the entire ECA rule class is worthy of further investigation.

7.3.4 Principal Component Analysis

There is a second natural way to decompose the ECA ensemble besides by velocity in the equally weighted sum over all rules – namely, by principal components. In our principal component analysis, the space-time evolutions of rules are treated as vectors, which undergo an orthogonal linear transformation to a new coordinate system with the property that the greatest variance of the vector set is parallel to the first coordinate, the second greatest variance of the vector set is parallel to the second coordinate, and so on [174]. Principal component analysis can therefore reveal reduced-dimensional representations of the ECA rules. In fact, the persistent non-

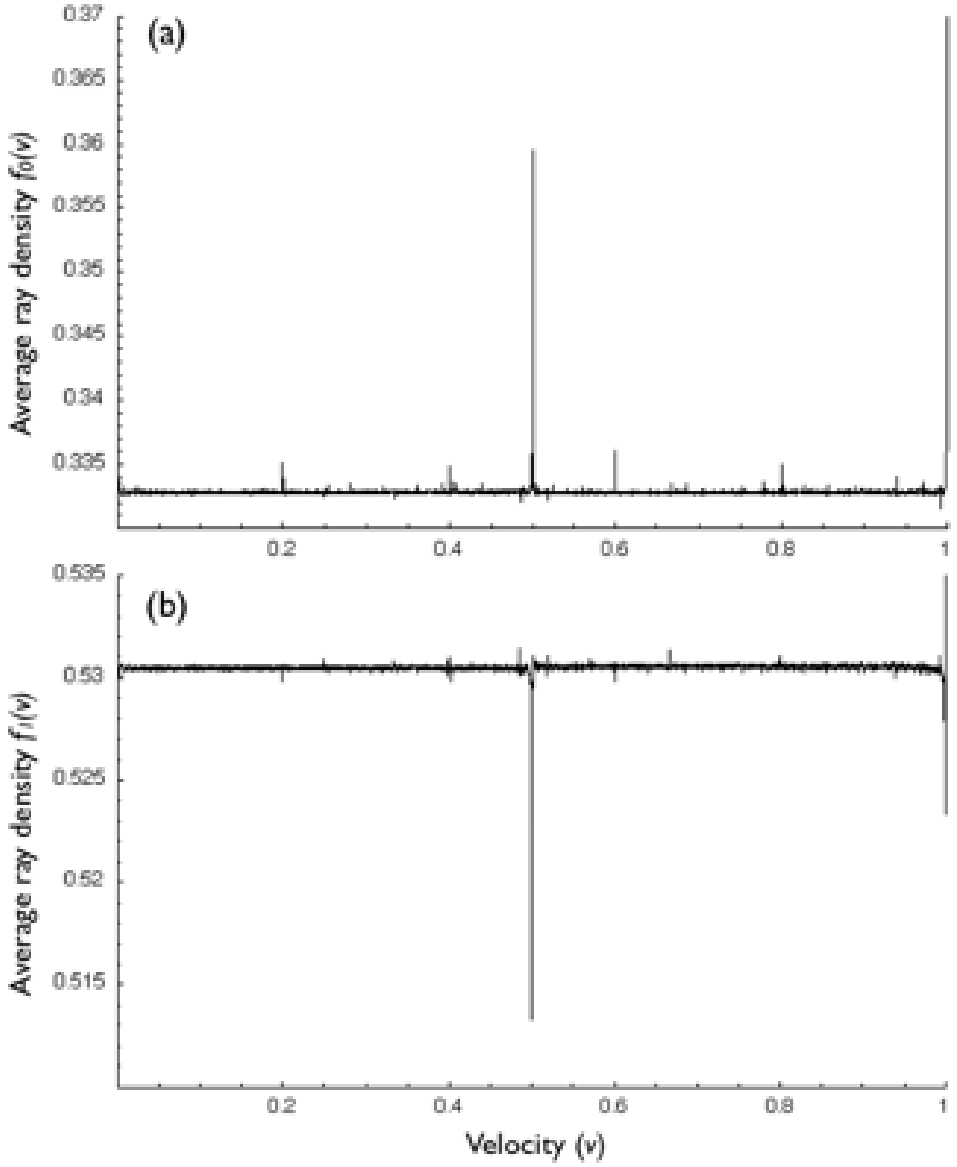

Figure 7.3: Dispersion spectra as measured by average density radiated outward from a single site at each velocity over (a) even and (b) odd iterations. (L=256, T=32768.)

interacting structures in the ensemble mean already suggested the presence of simple linearly independent components as a partial basis set. A full principal component set for the ECA over a finite time and configuration size is shown in Figure 7.4. In the principal component analysis of a configuration with $L = 16$ over time $2L/c$, starting from a single nonzero site, 111 components were found, a surprisingly small count compared to the number, 256, of ECA rules. A sharp dropoff in eigenvalue is visible in the 5 most dominant principal components, which appear geometrically simple and feature the $\pm c$ fronts and the even/odd iteration alternating densities. The next 9 components featured additional structure propagating at speeds of $\pm c$, but still appear simple at large scales. The presence of at least some geometrically simple principal components in the ECA may prove useful for attempts at self-assembly based on linearly combining cellular automata rules.

7.3.5 Generalizations

We now conclude our study of linear ensembles of CA rule classes by demonstrating that the rich behaviors observed thus far are not limited to the elementary cellular automata, but are, in fact, quite generic and present in a variety of other rule classes as well. As shown in Figure 7.5, rich patterning beyond simple traveling fronts appears to be present whenever, for example, more than one nearest neighbor affects the outcome of the rules for 2 colors, but requires only one nearest neighbor for 3 colors. This requirement suggests that there is a minimum threshold of rule class complexity needed to produce nontrivial patterning in the ensemble mean that depends on both the number of colors and the neighborhood size. It should therefore not be surprising

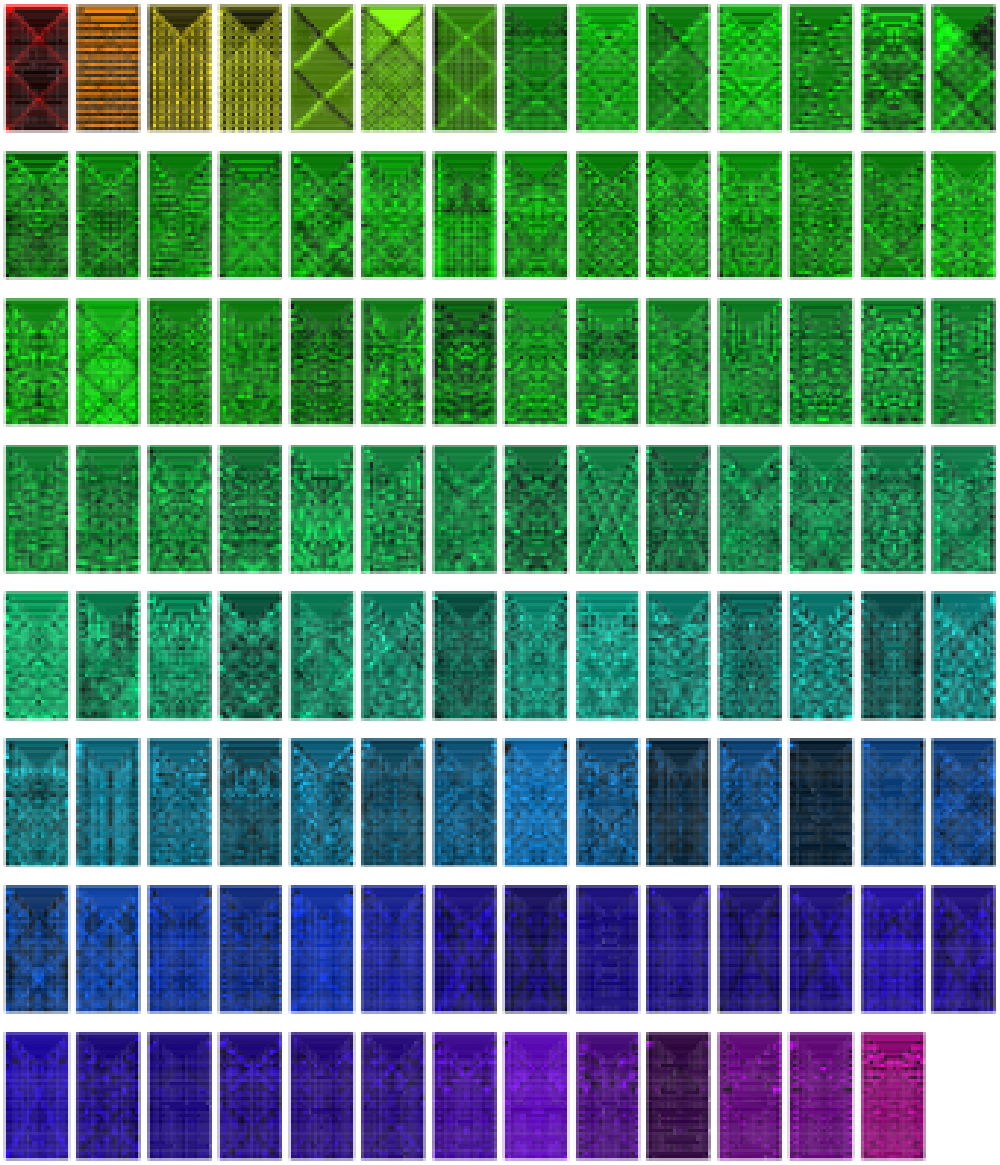

Figure 7.4: Principal component decomposition of the elementary cellular automata rules. The 111 principal components for the ensemble (L=16, T=32) are ordered by decreasing eigenvalue (first principal component is red), first from left to right, then top to bottom. The hue of each component represents the scaled logarithm of that components eigenvalue, and the sharp dropoff of eigenvalues in the first 5 components is visualized as a comparatively rapid transition from red to green as compared to the finer spectrum of the remaining components.

that similar patterning is observed in the 2-dimensional, 5-nearest-neighbor case as well, as shown in Figure 7.6.

7.4 Conclusion

We have shown, for the first time, that averages over spaces of iterated cellular automata rules produce rich interference structures rather than simple homogenization. A number of questions regarding the origin of the velocity and density of the structures remain open, and would be interesting to pursue in future work, since the mean ensemble we consider is such a natural encapsulation of the elementary cellular automata. Regardless, we have demonstrated with this simple system that rich patterning based on local interactions is possible without favoring any single interaction, which should be useful knowledge for future work in self-assembly.

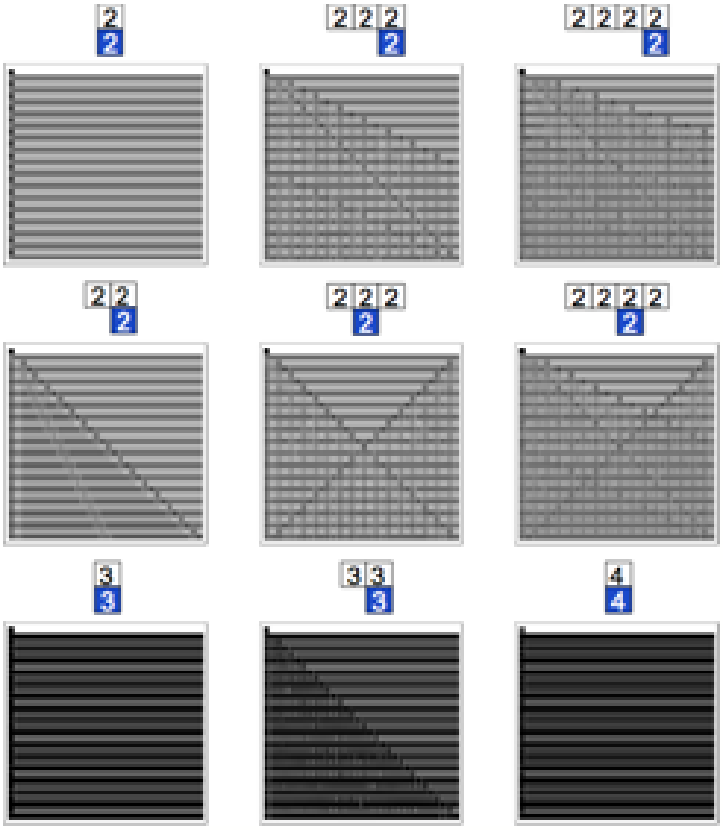

Figure 7.5: Ensembles means of other 1-D rule classes, with various numbers of site colors and neighbor dependencies. The number of colors per site and the neighbor dependence are indicated above each ensemble. (L=32, T=32.)

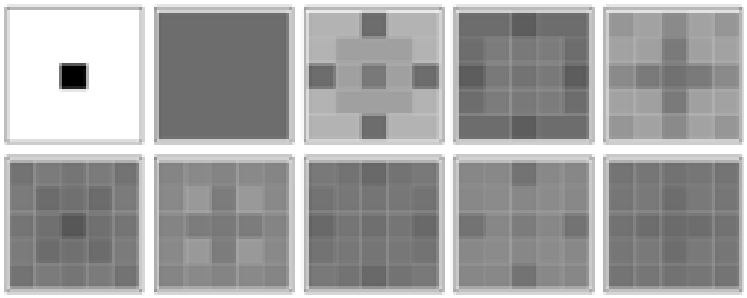

Figure 7.6: Ensemble mean of the first 10 iterations of all 2^{32} 2-dimensional, 5-nearest-neighbor rules.

Bibliography

[1] R. Kurzweil. *The Singularity is Near*. Penguin Group, 2005.

[2] N. Gershenfeld. *When Things Start to Think*. Henry Holt and Company, Inc., 1999.

[3] R. Waser. *Nanoelectronics and Information Technology*. Wiley-VCH, 2003.

[4] R. A. Freitas Jr. and R. C. Merkle. *Kinematic Self-Replicating Machines*. Landes Bioscience, 2004.

[5] D. Mulhall. *Our Molecular Future*. Prometheus Books, 2002.

[6] K. E. Drexler. *Nanosystems: Molecular Machinery, Manufacturing and Computation*. John Wiley and Sons, 1992.

[7] V. Colvin. From opals to optics: colloidal photonic crystals. *MRS Bulletin*, 26:637, 2001.

[8] S. Y. Chou. Patterned magnetic nanostructures and quantized magnetic disks. *Proc. IEEE*, 85:652, 1997.

[9] R. K. Soong, G. D. Bachand, H. P. Neves, A. G. Olkhovets, H. G. Craighead, and C. D. Montemagno. Powering an inorganic nanodevice with a biomolecular motor. *Science*, 290:1555, 2000.

[10] R. P.Andres, J. D. Bielefeld, J. I. Henderson, D. B. Janes, V. R. Kolagunta, C. P. Kubiak, W. Mahoney, and R. G. Osifchin. Self assembly at a two-dimensional superlattice of molecularly linked metal clusters. *Science*, 273:1690, 1996.

[11] S. J. Park, A. A. Lazarides, C. A. Mirkin, P. W. Brazis, C. R. Kannewurf, and R. L. Letsinger. The electrical properties of gold nanoparticle assemblies linked by dna. *Angew. Chem.*, 39:3845, 2000.

[12] U. C. Fischer and H. P. Zingsheim. Submicroscopic pattern replication with visible light. *J. Vac. Sci. Technol.*, 19:881, 1981.

[13] H. W. Deckman and J. H. Dunsmuir. Natural lithography. *Appl. Phys. Lett.*, 41:377, 1982.

[14] H. W. Deckman and J. H. Dunsmuir. Applications of surface textures produced with natural lithography. *J. Vac. Sci. Technol. B*, 1:1109, 1983.

[15] J. C. Hulteen and R. P. Van Duyne. Nanosphere lithography: a materials general fabrication process for periodic particle array surfaces. *J. Vac. Sci. Technol. A*, 13:1553, 1995.

[16] C. L. Haynes, A. D. McFarland, M. T. Smith, J. C. Hulteen, and R. P. Van-Duyne. Angle-resolved nanosphere lithography: manipulation of nanoparticle size, shape, and interparticle spacings. *J. Phys. Chem. B*, 106:1898, 2002.

[17] C. L. Haynes and R. P. Van Duyne. Nanosphere lithography: a versatile nanofabrication tool for studies of size-dependent nanoparticle optics. *J. Phys. Chem. B*, 105:5599, 2001.

[18] T. R. Jensen, M. D. Malinsky, C. L. Haynes, and R. P. Van Duyne. Nanosphere lithography: tunable localized surface plasmon resonance spectra of silver nanoparticles. *J. Phys. Chem. B*, 104:10549, 2000.

[19] J. Boneberg, F. Burmeister, C. Schafle, P. Leiderer, D. Reim, A. Fery, and S. Herminghaus. The formation of nano-dot and nano-ring structures in colloidal monolayer lithography. *Langmuir*, 13:7080, 1997.

[20] A. Hatzor and P. S. Weiss. Molecular rulers for scaling down nanostructures. *Science*, 291:1019, 2001.

[21] M. E. Anderson, R. K. Smith, Z. J. Donhauser, A. Hatzor, P. A. Lewis, L. P. Tan, H. Tanaka, M. W. Horn, and P. S. Weiss. Exploiting intermolecular interactions and self-assembly for ultrahigh resolution nanolithography. *J. Vac. Sci. Technol. B*, 20:2739, 2002.

[22] M. E. Anderson, L. P. Tan, H. Tanaka, M. Mihok, H. Lee, M. W. Horn, and P. S. Weiss. Advances in nanolithography using molecular rulers. *J. Vac. Sci. Technol. B*, 21:3116, 2003.

[23] H. Tanaka, M. E. Anderson, M. W. Horn, and P. S. Weiss. Position-selected molecular ruler. *Jpn. J. Appl. Phys.*, 43:L950, 2004.

[24] M. E. Anderson, M. Mihok, H. Tanaka, L.-P. Tan, M. W. Horn, G. S. McCarty, and P. S. Weiss. Hybrid approaches to nanolithography: photolithographic structures with precise, controllable nanometer-scale spacings created by molecular rulers. *Adv. Mat.*, 18:1020, 2006.

[25] S. D. Evans, A. Ulman, K. E. Goppert-Berarducci, and J. L. Gerenser. Self-assembled multilayers of ω-mercaptoalkanoic acids: selective ionic interactions. *J. Am. Chem. Soc.*, 113:5866, 1991.

[26] S. Guo, L. Konopny, R. Popovitz-Biro, H. Cohen, H. Porteanu, E. Lifshitz, and M. Lahav. Thioalkanoates as site-directing nucleating centers for the preparation of patterns of cds nanoparticles within 3-d crystals and lb films of cd alkanoates. *J. Am. Chem. Soc.*, 121:9589, 1999.

[27] K. Grieve, P. Mulvaney, and F. Grieser. Synthesis and electronic properties of semiconductor nanoparticles quantum dots. *Curr. Opin. Colloid & Interface Sci.*, 5:168, 2000.

[28] J. Rose, A. el Gamal, and A. Sangiovanni-Vincentelli. Architecture of field-programmable gate arrays. *Proc. IEEE*, 81:1013, 1993.

[29] Ö. Türel and K. Likharev. Crossnets: possible neuromorphic networks based on nanoscale components. *Int. J. Circ. Theor. Appl.*, 31:37, 2003.

[30] J. C. Ellenbogen and J. C. Love. Architectures for molecular electronic computers: 1. logic structures and an adder designed from molecular electronic diodes. *Proc. IEEE*, 88:386, 2000.

[31] J. Moser, R. Panepucci, Z. P. Huang, W. Z. Li, Z. F. Ren, A. Usheva, and M. J. Naughton. Individual free-standing carbon nanofibers addressable on the 50 nm scale. *J. Vac. Sci. Technol. B*, 21:1004, 2003.

[32] P. K. Lala. *Self-Checking and Fault-Tolerant Digital Design.* Academic Press, 2001.

[33] Y. Huang, X. Duan, Q. Wei, and C. M. Lieber. Directed assembly of one-dimensional nanostructures into functional networks. *Science*, 291:630, 2001.

[34] R. Agarwal, K. Ladavac, Y. Roichman, G. Yu, C. M. Lieber, and D. G. Grier. Manipulation and assembly of nanowires with holographic optical traps. *Opt. Express*, 13:8906, 2005.

[35] P. J. Pauzauskie, A. Radenovic, E. Trepagnier, H. Shroff, P. Yang, and J. Liphardt. Optical trapping and integration of semiconductor nanowire assemblies in water. *Nat. Mater.*, 5:97, 2006.

[36] J. E. Jang, S. N. Cha, Y. Choi, G. A. J. Amaratunga, D. J. Kang, D. G. Hasko, J. E. Jung, and J. M. Kim. Nanoelectromechanical switches with vertically aligned carbon nanotubes. *Appl. Phys. Lett.*, 87:163114, 2005.

[37] T. Rueckes, K. Kim, E. Joselevich, G. Y. Tseng, C. L. Cheung, and C. M. Lieber. Carbon nanotube-based nonvolatile random access memory for molecular computing. *Science*, 289:94, 2000.

[38] H. A. Pohl. *Dielectrophoresis*. Cambridge University Press, 1978.

[39] P. Y. Chiou, A. T. Ohta, and M. C. Wu. Massively parallel manipulation of single cells and microparticles using optical images. *Nature*, 436:370, 2005.

[40] L. Dong, J. Bush, V. Chirayos, R. Solanki, J. Jiao, Y. Ono, J. F. Conley Jr., and B. R. Ulrich. Dielectrophoretically controlled fabrication of single-crystal nickel silicide nanowire interconnects. *Nano Lett.*, 5:2112, 2005.

[41] X. Duan, Y. Huang, Y. Cui, J. Wang, and C. M. Lieber. Indium phosphide nanowires as building blocks for nanoscale electronic and optoelectronic devices. *Nature*, 409:66, 2001.

[42] T. H. Kim, S. Y. Lee, N. K. Cho, H. K. Seong, H. J. Choi, S. W. Jung, and S. K. Lee. Dielectrophoretic alignment of gallium nitride nanowires (gan nws) for use in device applications. *Nanotechnology*, 17:3394, 2006.

[43] Z. Chen, Y. Yang, F. Chen, Q. Qing, Z. Wu, and Z. Liu. Controllable interconnection of single-walled carbon nanotubes under ac electric field. *J. Phys. Chem. B*, 109:11420, 2005.

[44] S. W. Lee and R. Bashir. Dielectrophoresis and electrohydrodynamics-mediated fluidic assembly of silicon resistors. *Appl. Phys. Lett.*, 83:3833, 2003.

[45] O. Harnack, C. Pacholski, H. Weller, A. Yasuda, and J. M. Wessels. Rectifying behavior of electrically aligned zno nanorods. *Nano Lett.*, 3:1097, 2003.

[46] C. S. Lao, J. Liu, P. Gao, L. Zhang, D. Davidovic, R. Tummala, and Z. L. Wang. Zno nanobelt/nanowire schottky diodes formed by dielectrophoresis alignment across au electrodes. *Nano Lett.*, 6:263, 2006.

[47] L. Shang, T. L. Clare, M. A. Eriksson, M. S. Marcus, K. M. Metz, and R. J. Hamers. Directed assembly and electrical characterization of nanowire bridges using biomolecular recognition elements. *Nanotechnology*, 16:2846, 2005.

[48] Y. Cui, L. J. Lauhon, M. S. Gudiksen, J. Wang, and C. M. Lieber. Diameter-controlled synthesis of single-crystal silicon nanowires. *Appl. Phys. Lett.*, 78:2214, 2001.

[49] D. R. Lide (ed). *CRC Handbook of Chemistry and Physics*. CRC Press, 82 edition, 2001.

[50] B. Nair. *J. Toxicol.*, 20 S3:23, 2001.

[51] M. S. Gudiksen, L. J. Lauhon, J. Wang, D. Smith, and C. M. Lieber. Growth of nanowire superlattice structures for nanoscale photonics and electronics. *Nature*, 415:617, 2002.

[52] E. A. Mayeda, L. L. Miller, and J. F. Wolf. Electrooxidation of benzylic ethers, esters, alcohols, and phenyl epoxides. *J. Am. Chem. Soc.*, 94:6812, 1972.

[53] S. Y. Kishioka, M. Umeda, and A. Yamada. Electrooxidation of benzylalcohol derivatives in aqueous solution. In *Proc. Electrochem. Soc.*, page Extended Abstract 2474, Paris, 2003.

[54] M. S. Fuhrer, A. K. L. Lim, L. Shih, U. Varadarajan, A. Zettl, and P. L. McEuen. Transport through crossed nanotubes. *Physica E*, 6:868, 2000.

[55] B. L. Smith and E. H. Rhoderic. *Solid-St. Electron.*, 14:71, 1971.

[56] D. J. Tritton. *Physical Fluid Dynamics*. Oxford University Press, 1988.

[57] R. Lappalainen, A. Anttila, and H. Heinonen. Diamond coated total hip replacements. *Clin. Orthop. Relat. R.*, 352:118, 1998.

[58] S. Mitura, K. Zolynski, P. Witkowski, A. Kaluzny, Z. Has, and P. Niedzielski. Implants with hard carbon layers for application in pseudoarthrosis femoris sin. ostitis post fracturam apertam olim factam. *J. Chem. Vap. Dep.*, 4:232, 1996.

[59] D. P. Dowling, P. V. Kola, K. Donnelly, T. C. Kelly, K. Brumitt, L. Lloyd, R. Eloy, M. Therin, and N. Weill. Evaluation of diamond-like carbon-coated orthopaedic implants. *Diam. Relat. Mater.*, 6:390, 1997.

[60] J. Franks and D. Finch. *Nanotechnology in Medicine and the Biosciences*. Gordon and Breach Publishers, 1996.

[61] C. Du, X. W. Su, F. Z. Cui, and X. D. Zhu. Morphological behaviour of osteoblasts on diamond-like carbon coating and amorphous c-n film in organ culture. *Biomaterials*, 19:651, 1998.

[62] G. Dearnaley. Diamond-like carbon: a potential means of reducing wear in total joint replacements. *Clin. Mater.*, 12:237, 1993.

[63] L. Tang, C. Tsai, W. W. Gerberich, L. Kruckeberg, and D. R. Kania. Biocompatibility of chemical-vapor-deposited diamond. *Biomaterials*, 16:483, 1995.

[64] Jr. R. A. Freitas. *Nanomedicine, Volume IIA: Biocompatibility*. Landes Bioscience, 2003.

[65] J. Hu, X.-D. Xiao, D. F. Ogletree, and M. Salmeron. Imaging the condensation and evaporation of molecularly thin films of water with nanometer resolution. *Science*, 268:267, 1995.

[66] P. B. Miranda, L. Xu, Y. R. Shen, and M. Salmeron. Icelike water monolayer adsorbed on mica at room temperature. *Phys. Rev. Lett.*, 81:5876, 1998.

[67] M. Odelius, M. Bernasconi, and M. Parrinello. Two dimensional ice adsorbed on mica surface. *Phys. Rev. Lett.*, 78:2855, 1997.

[68] X. Su, L. Lianos, Y. Ron Shen, and G. A. Somorjai. Surface-induced ferroelectric ice on pt(111). *Phys. Rev. Lett.*, 80:1533, 1998.

[69] C.-Y. Ruan, V. A. Lobastov, F. Vigliotti, S. Chen, and A. H. Zewail. Ultrafast electron crystallography of interfacial water. *Science*, 304:80, 2004.

[70] R. Zangi. Water confined to a slab geometry: a review of recent computer simulation studies. *J. Phys.: Condens. Matter*, 16:S5371, 2004.

[71] V. Ostroverkhov, G. A. Waychunas, and Y. R. Shen. New information on water interfacial structure revealed by phase-sensitive surface spectroscopy. *Phys. Rev. Lett.*, 94:046102, 2005.

[72] E.-M. Choi, Y.-H. Yoon, S. Lee, and H. Kang. Freezing transition of interfacial water at room temperature under electric fields. *Phys. Rev. Lett.*, 95:085701, 2005.

[73] R. Zangi and A. E. Mark. Electrofreezing of confined water. *J. Chem. Phys.*, 120:7123, 2004.

[74] K. Koga, X. C. Zeng, and H. Tanaka. Freezing of confined water: A bilayer ice phase in hydrophobic nanopores. *Phys. Rev. Lett.*, 79:5262, 1997.

[75] L. Chen, P. Fenter, K. L. Nagy, M. L. Schlegel, and N. C. Sturchio. Molecular-scale density oscillations in water adjacent to a mica surface. *Phys. Rev. Lett.*, 87:156103, 2001.

[76] S.-H. Park and G. Sposito. Structure of water adsorbed on a mica surface. *Phys. Rev. Lett.*, 89:085501, 2002.

[77] S. Meng, Z. Zhang, and E. Kaxiras. Tuning solid surfaces from hydrophobic to superhydrophilic by submonolayer surface modification. *Phys. Rev. Lett.*, 97:036107, 2006.

[78] H. Okushi. High quality homoepitaxial cvd diamond for electronic devices. *Diamond Relat. Mater.*, 10:281, 2001.

[79] A. Dorner-Reisel, C. Schürer, G. Irmer, F. Simon, C. Nischan, and E. Müller. Diamond-like carbon coatings with ca-o-incorporation for improved biological acceptance. *Anal. Bioanal. Chem.*, 374:753, 2002.

[80] M. Matsumoto, S. Saito, and I. Ohmine. Molecular dynamics simulation of the ice nucleation and growth process leading to water freezing. *Nature*, 416:409, 2002.

[81] J. L. F. Abascal, E. Sanz, R. Garcia Fernndez, and C. Vega. A potential model for the study of ices and amorphous water: Tip4p/ice. *J. Chem. Phys.*, 122:234511, 2005.

[82] J. L. F. Abascal and C. Vega. A general purpose model for the condensed phases of water: Tip4p/2005. *J. Chem. Phys.*, 123:234505, 2005.

[83] V. F. Petrenko and R. W. Whitworth. *Physics of Ice*. Oxford University Press, 2002.

[84] H. C. Andersen. Molecular dynamics simulations at constant pressure and/or temperature. *J. Chem. Phys.*, 72:2384, 1980.

[85] K. Hinsen. The molecular modeling toolkit: A new approach to molecular simulations. *J. Comp. Chem.*, 21:79, 2000.

[86] W. L. Jorgensen and J. Tirado-Rives. The opls [optimized potentials for liquid simulations] potential functions for proteins, energy minimizations for crystals of cyclic peptides and crambin. *J. Am. Chem. Soc.*, 110:1657, 1988.

[87] J. Aqvist. Ion-water interaction potentials derived from free energy perturbation simulations. *J. Phys. Chem.*, 94:8021, 1990.

[88] D. C. Spellmeyer and K. N. Houk. A force-field model for intramolecular radical additions. *J. Org. Chem.*, 52:959, 1987.

[89] S. J. Weiner, P. A. Kollman, D. T. Nguyen, and D. A. Case. An all atom force field for simulations of proteins and nucleic acids. *J. Comp. Chem.*, 7:230, 1986.

[90] J. Fröhlich and C.-E. Pfister. On the absence of spontaneous symmetry breaking and of crystalline ordering in two-dimensional systems. *Commun. Math. Phys.*, 81:277, 1981.

[91] K. Zahn and G. Maret. Dynamic criteria for melting in two dimensions. *Phys. Rev. Lett.*, 85:3656, 2000.

[92] X. H. Zheng and J. C. Earnshaw. On the lindemann criterion in 2d. *Europhys. Lett.*, 41:635, 1998.

[93] B. J. Alder, W. G. Hoover, and T. E. Wainwright. Cooperative motion of hard disks leading to melting. *Phys. Rev. Lett.*, 11:241, 1963.

[94] Y. Kaibara, K. Sugata, M. Tachiki, H. Umezawa, and H. Kawarada. Control wettability of the hydrogen-terminated diamond surface and the oxidized diamond surface using the atomic force microscope. *Diamond Rel. Mat.*, 12:560, 2003.

[95] D. T. Mitchell, S. B. Lee, L. Trofin, N. Li, T. K. Nevanen, H. Soderlund, and C. R. J. Martin. Smart nanotubes for bioseparations and biocatalysis. *J. Am. Chem. Soc.*, 124:11864, 2002.

[96] S. A. Miller, V. Y. Young, and C. R. J. Martin. Electroosmotic flow in template-prepared carbon nanotube membranes. *J. Am. Chem. Soc.*, 123:12335, 2001.

[97] A. L. Garcia, L. K. Ista, D. M. Petsev, M. J. OBrien, P. Bisong, A. A. Mammoli, S. R. J. Brueck, and G. P. López. Electrokinetic molecular separation in nanoscale fluidic channels. *Lab on a Chip*, 5:1271, 2005.

[98] Y.-C. Wang, A. L. Stevens, and J. Han. Million-fold preconcentration of proteins and peptides by nanofluidic filter. *Anal Chem.*, 77:4293, 2005.

[99] H. Chang, F. Kosari, G. Andreadakis, M. A. Alam, G. Vasmatzis, and R. Bashir. Dna-mediated fluctuations in ionic current through silicon oxide nanopore channels. *Nano Lett.*, 4:1551, 2004.

[100] P. Chen, J. Gu, E. Brandin, Y.-R. Kim, Q. Wang, and D. Branton. Probing single dna molecule transport using fabricated nanopores. *Nano Lett.*, 4:2293, 2004.

[101] J. O. Tegenfeldt, C. Prinz, H. Cao, S. Chou, W. W. Reisner, R. Riehn, Y. M. Wang, E. C. Cox, J. C. Sturm, P. Silberzan, and R. H. Austin. The dynamics of genomic-length dna molecules in 100-nm channels. *Proc. Natl. Acad. Sci. U.S.A.*, 101:10979, 2004.

[102] J. J. Nakane, M. Akeson, and A. Marziali. Recognizing a single base in an individual dna strand: A step toward dna sequencing in nanopores. *J. Phys.: Cond. Matt.*, 15:R1365, 2003.

[103] A. F. Sauer-Budge, J. A. Nyamwanda, D. K. Lubensky, and D. Branton. Unzipping kinetics of double-stranded dna in a nanopore. *Phys. Rev. Lett.*, 90:238101, 2003.

[104] A. Hibara, T. Saito, H.-B. Kim, M. Tokeshi, T. Ooi, M. Nakao, and T. Kitamori. Nanochannels on a fused-silica microchip and liquid properties investigation by time-resolved fluorescence measurements. *Anal. Chem.*, 74:6170, 2002.

[105] N. R. Tas, P. Mela, T. Kramer, J. W. Berenschot, and A. van den Berg. Capillarity induced negative pressure of water plugs in nanochannels. *Nano Lett.*, 3:1537, 2003.

[106] M. S. Dresselhaus, G. Dresselhaus, and P. Eklund. *Science of Fullerenes and Carbon Nanotubes*. Academic Press, 1996.

[107] R. Tenne, M. Homyonfer, and Y. Feldman. Inorganic fullerene-like and nanotube materials: Synthesis, characterization and potential applications. *Chem. Mater.*, 10:3225, 1998.

[108] M. Nath, A. Govindaraj, and C. N. R. Rao. Simple synthesis of mos_2 and ws_2 nanotubes. *Adv. Mat.*, 13:283, 2001.

[109] N. G. Chopra, R. J. Luyken, K. Cherry, V. H. Crespi, M. L. Cohen, S. G. Louis, and A. Zettl. Boron nitride nanotubes. *Science*, 269:966, 1995.

[110] Y. R. Hacohen, E. Grunbaum, J. Sloan, J. L. Hutchison, and R. Tenne. Cage structures and nanotubes of $nicl_2$. *Nature*, 395:336, 1998.

[111] Y. Li, J. Wang, Z. Deng, Y. Y. Wu, X. Sun, S. Fan, , D. Yu, and P. Yang. Bismuth nanotubes: a rational low-temperature synthetic route. *J. Am. Chem. Soc.*, 123:9904, 2001.

[112] B. B. Lakshimi, C. J. Patrissi, and C. R. Martin. Sol-gel template synthesis of semiconductor oxide micro- and nanostructures. *Chem. Mater.*, 9:2544, 1997.

[113] J. Hwang, B. Min, J. S. Lee, K. Keem, K. Cho, M.-Y. Sung, M.-S. Lee, and S. Kim. Al_2o_3 nanotubes fabricated by wet etching of zno/al_2o_3 core/shell nanofibers. *Adv. Mat.*, 16:422, 2004.

[114] M. Yada, M. Mihara, S. Mouri, M. Kuroki, and T. Kijima. Rare earth (er, tm, yb, lu) oxide nanotubes templated by dodecylsulfate assemblies. *Adv. Mat.*, 14:309, 2002.

[115] J. Hu, Y. Bando, D. Golberg, and Q. Liu. Gallium nitride nanotubes by the conversion of gallium oxide nanotubes. *Angew. Chem. Int. Ed.*, 115:3617, 2003.

[116] J. Goldberger, R. He, Y. Zhang, S. Lee, H. Yan, H.-J. Choi, and P. Yang. Single crystal gallium nitride nanotubes. *Nature*, 422:599, 2003.

[117] S. Y. Jeong, J. Y. Kim, H. D. Yang, B. N. Yoon, S.-H. Choi, H. K. Kang, C. W. Yang, and Y. H. Lee. Synthesis of silicon nanotubes on porous alumina using molecular beam epitaxy. *Adv. Mat.*, 15:1172, 2003.

[118] J. Sha, J. Niu, X. Ma, J. Xu, X. Zhang, Q. Yang, and D. Yang. Silicon nanotubes. *Adv. Mat.*, 14:1219, 2002.

[119] J. Hu, Y. Bando, Z. Liu, J. Zhan, D. Golberg, and T. Sekiguchi. Synthesis of silicon tubular nanostructures with zns as removable templates. *Angew. Chem. Int. Ed.*, 43:63, 2004.

[120] Y. Cui, Q. Wei, H. Park, and C. M. Lieber. Nanowire nanosensors for highly sensitive and selective detection of biological and chemical species. *Science*, 293:1289, 2001.

[121] F. Patolsky, G. Zheng, O. Hayden, M. Lakadamyali, X. Zhuang, and C. M. Lieber. Electrical detection of single viruses. *Proc. Natl. Acad. Sci. U.S.A.*, 101:14017, 2004.

[122] G. Zheng, F. Patolsky, Y. Cui, W. U. Wang, and C. M. Lieber. Multiplexed electrical detection of cancer markers with nanowire sensor arrays. *Nat. Biotechnol.*, 23:1294, 2005.

[123] F. Patolsky and C. M. Lieber. Nanowire nanosensors. *Materials Today*, page 20, April 2005.

[124] S. Pennathur and J. G. Santiago. Electrokinetic transport in nanochannels: 1. theory. *Anal. Chem.*, 77:6772, 2005.

[125] H. Daiguji, P. Yang, and A. Majumdar. Ion transport in nanofluidic channels. *Nano Lett.*, 4:137, 2004.

[126] R. Karnik, R. Fan, M. Yue, L. Deyu, P. Yang, and A. Majumdar. Electrostatic control of ions and molecules in nanofluidic transistors. *Nano Lett.*, 5:943, 2005.

[127] H. Daiguji, Y. Oka, and K. Shirono. Nanofluidic diode and bipolar transistor. *Nano Lett.*, 5:2274, 2005.

[128] R. Karnik, K. Castelino, R. Fan, P. Yang, and A. Majumdar. Effects of biological reactions and modifications on conductance of nanofluidic channels. *Nano Lett.*, 5:1638, 2005.

[129] C. M. Martin. Nanomaterials: A membrane-based synthetic approach. *Science*, 266:1961, 1994.

[130] Y. Cui, L. J. Lauhon, M. S. Gudiksen, J. Wang, and C. M. Lieber. Diameter-controlled synthesis of single-crystal silicon nanowires. *Appl. Phys. Lett.*, 78:2214, 2001.

[131] A. B. Greytak, L. J. Lauhon, M. G. Gudiksen, and C. M. Lieber. Growth and transport properties of complementary germanium nanowire field-effect transistors. *Appl. Phys. Lett.*, 84:4176, 2004.

[132] L. J. Lauhon, M. S. Gudiksen, D. Wang, and C. M. Lieber. Epitaxial core-shell and core-multi-shell nanowire heterostructures. *Nature*, 420:57, 2002.

[133] C. M. Lieber. Nanoscale science and technology: Building a big future from small things. *M.R.S. Bull.*, 28:486, 2003.

[134] Y. Cui and C. M. Lieber. Functional nanoscale electronic devices assembled using silicon nanowire building blocks. *Science*, 291:851, 2001.

[135] Y. Cui, X. Duan, J. Hu, and C. M. Lieber. Doping and electrical transport in silicon nanowires. *J. Phys. Chem. B*, 104:5213, 2000.

[136] Y. Cui, Z. Zhong, D. Wang, W. U. Wang, and C. M. Lieber. High performance silicon nanowire field effect transistors. *Nano Lett.*, 3:149, 2003.

[137] A. Krishnan, E. Dujardin, M. M. J. Treacy, J. Hugdahl, S. Lynum, and T. W. Ebbesen. Graphitic cones and the nucleation of curved carbon surfaces. *Nature*, 388:451, 1997.

[138] O. Hod and E. Rabani. A coarse-grained model for a nanometer scale molecular pump. *Proc. Natl. Acad. Sci. U.S.A.*, 100:14661, 2003.

[139] D. Wang, F. Qian, C. Yang, Z. Zhong, and C. M. Lieber. Rational growth of branched and hyper-branched nanowire structures. *Nano Lett.*, 4:871, 2004.

[140] K. A. Dick, K. Deppert, M. W. Larsson, T. Mrtensson, W. Seifert, L. R. Wallenberg, and L. Samuelson. Synthesis of branched 'nanotrees' by controlled seeding of multiple branching events. *Nature Mat.*, 3:380, 2004.

[141] Gerald H. Ristow. *Pattern Formation in Granular Materials*. Springer-Verlag, New York, 2000.

[142] Francisco Melo, Paul Umbanhowar, and Harry L. Swinney. Transition to parametric wave patterns in a vertically oscillated granular layer. *Physical Review Letters*, 72(1):172–175, 1994.

[143] Johann M. Schleier-Smith and Howard A. Stone. Convection, heaping, and cracking in vertically vibrated granular slurries. *Physical Review Letters*, 86(14):3016–3019, 2001.

[144] Haeng Sub Wi, Kipom Kim, and Hyuk Kyu Pak. Pattern selection on granular layers under multiple frequency forcing. *Journal of the Korean Physical Society*, 38(5):573–576, 2001.

[145] Shigeru Naito, Munehiko Minoura, Munenobu Takeda, and Etsuro Okuyama. Ship motion analyses in compact wave basin with absorbing wave-maker. *Int. J. Offshore Polar*, 16:10–17, 2006.

[146] Jonathan E. Luntz, William Messner, and Howie Choset. Discreteness issues in actuator arrays. In *IEEE International Conference on Robotics and Automation*, 1999.

[147] Karl F. Böhringer, Bruce R. Donald, Lydia E. Kavraki, and Florent Lamiraux. Part orientation with one or two stable equilibria using programmable vector fields. In *IEEE International Conference on Robotics and Automation*, 1999.

[148] Mark Yim and Andy Berlin. Contact and non-contact mechanisms for distributed manipulation. In *IEEE International Conference on Robotics and Automation*, 1999.

[149] J. W. Suh, R. B. Darling, K.-F. Böhringer, B. R. Donald, H. Baltes, and G. T. A. Kovacs. Fully programmable mems ciliary actuator arrays for micromanipulation tasks. In *IEEE International Conference on Robotics and Automation*, 2000.

[150] Dan S. Reznik. *The Universal Planar Manipulator*. PhD thesis, University of California at Berkeley, Computer Science Division, 2000.

[151] M. V. Sapozhnikov, Y. V. Tolmachev, I. S. Aranson, and W.-K. Kwok. Dynamics self-assembly and patterns in electrostatically driven granular media. *Physical Review Letters*, 90(11):114301, 2003.

[152] Troy Shinbrot and Fernando J. Muzzio. Reverse buoyancy in shaken granular beds. *Physical Review Letters*, 81(20):4365–4368, 1998.

[153] James B. Knight, H. M. Jaeger, and Sidney R. Nagel. Vibration-induced size separation in granular media: The convection connection. *Physical Review Letters*, 70(24):3728–3731, 1993.

[154] Rémi Jullien and Paul Meakin. Three-dimensional model for particle-size segregation by shaking. *Physical Review Letters*, 69(4):640–643, 1992.

[155] E. Clément and L. Labous. Pattern formation in a vibrated granular layer: The pattern selection issue. *Physical Review E*, 62(6):8314–8323, 2000.

[156] Harvey Gould and Jan Tobochnik. *An Introduction to Computer Simulation Methods: Applications to Physical Systems*. Benjamin Cummings, San Francisco, second edition, 1996.

[157] S. Luding, E. Clément, J. Rajchenbach, and J. Duran. Simulations of pattern formation in vibrated granular media. *Europhysics Letters*, 36(4):247–252, 1996.

[158] D. C. Rapaport. *The Art of Molecular Dynamics Simulation*. Cambridge University Press, New York, 1995.

[159] Kalvis M. Jansons and G. D. Lythe. Stochastic stokes drift. *Physical Review Letters*, 81(15):3136–3139, 1998.

[160] Guy Metcalfe, S. G. K. Tennakoon, L. Kondic, D. G. Schaeffer, and R. P. Behringer. Granular friction, coulomb failure, and the fluid-solid transition for horizontally shaken granular materials. *Physical Review E*, 65(031302), February 2002.

[161] R. Nagpal. Programmable self-assembly using biologically-inspired multiagent control. In *Proceedings of the 1st International Joint Conference on Autonomous Agents and Multi-Agent Systems (AAMAS'02)*, page 418, 2002.

[162] S. Liao and N. C. Seeman. Translation of dna signals into polymer assembly instructions. *Science*, 306:2072, 2004.

[163] C. E. Flynn, S.-W. Lee, B. R. Peellee, and A. M. Belcher. Viruses as vehicles for growth, organization and assembly of materials. *Acta Mater.*, 51:5867, 2003.

[164] J. M. Stuart, E. Segal, D. Koller, and S. K. Kim. A gene-coexpression network for global discovery of conserved genetic modules. *Science*, 302:249, 2003.

[165] B. Berger and T. Leighton. Protein folding in the hydrophobic-hydrophilic (hp) model is np-complete. In *Proceedings of the 2nd Annual International Conference on Computational Molecular Biology*, page 30, 1998.

[166] E. Domany and W. Kinzel. Equivalence of cellular automata to ising models and directed percolation. *Phys. Rev. Lett.*, 53:311, 1984.

[167] A. Adamatzky. *Identification of Cellular Automata*. Taylor Francis, 1994.

[168] S. Wolfram. Statistical mechanics of cellular automata. *Rev. Mod. Phys.*, 55:601, 1983.

[169] C. Moore. Predicting nonlinear cellular automata quickly by decomposing them into linear ones. *Physica D*, 111:27, 1998.

[170] L. Deniau and J. Blanc-Talon. Pca and cellular automata: a statistical approach for deterministic machines. *Complexity International*, 2, 1995.

[171] N. H. Packard and S. Wolfram. Two-dimensional cellular automata. *J. Stat. Phys.*, 38:901, 1984.

[172] V. Guinot. Modelling using stochastic, finite state cellular automata: rule inference from continuum models. *Appl. Math. Modelling*, 26:701, 2002.

[173] S. Wolfram. *A New Kind of Science*. Wolfram Media, 2002.

[174] I. T. Jolliffee. *Principal Component Analysis*. Springer-Verlag, 2002.